CFD Simulation of the Interaction of Buoyant Flows with Nuclear Aerosols

CFD-Simulation der Wechselwirkung von Auftriebsströmungen mit nuklearen Aerosolen

Von der Fakultät für Maschinenwesen der Rheinisch-Westfälischen Technischen Hochschule Aachen zur Erlangung des akademischen Grades eines Doktors der Ingenieurwissenschaften genehmigte Dissertation

vorgelegt von

Vijaya Kumar Gopala Krishna Moorthy

Berichter: Univ.-Prof. Dr. rer. nat. Hans-Josef Allelein
Univ.-Prof. Dr.-Ing. Reinhold Kneer
Prof. Sarith P. Sathian, Ph.D.
Prof. Prasad Patnaik B.S.V., Ph.D.

Tag der mündlichen Prüfung: 16. Dez. 2022

„Diese Dissertation ist auf den Internetseiten der Universitätsbibliothek online verfügbar.“

Pre-publications

Journal articles

1. Vijaya Kumar, G., Kampili, M., Kelm, S., Prakash, K. A., & Allelein, H. (2020). CFD modelling of buoyancy driven flows in enclosures with relevance to nuclear reactor safety. *Nuclear Engineering and Design*, *365*(December 2019), 110682.
2. Vijaya Kumar, G., Cammiade, L. M. F., Kelm, S., Arul Prakash, K., Groß, E. M., Allelein, H. J., Kneer, R., & Rohlfs, W. (2021). Implementation of a CFD model for wall condensation in the presence of non-condensable gas mixtures. *Applied Thermal Engineering*, *187*(August 2020), 116546.
3. Kampili, M., Vijaya Kumar, G., Kelm, S., Arul Prakash, K., & Allelein, H. (2021). CFD simulations of stratified layer erosion in MiniPanda facility using the tailored CFD solver containmentFOAM. *International Journal of Heat and Mass Transfer*, *178*, 121568.
4. Kelm, S., Kampili, M., Liu, X., George, A., Schumacher, D., Druska, C., Struth, S., Kuhr, A., Ramacher, L., Allelein, H.-J., Prakash, K. A., Vijaya Kumar, G., Cammiade, L. M. F., & Ji, R. (2021). The Tailored CFD Package 'containmentFOAM' for Analysis of Containment Atmosphere Mixing, H2/CO Mitigation and Aerosol Transport. *Fluids*, *6*(3), 100.

Conference Proceedings

5. Vijaya Kumar, G., Kelm, S., Arul Prakash, K., & Allelein, H.-J. (2018). CFD modelling of buoyancy driven flows in enclosures: relevance to nuclear reactor safety. *Asian Symposium of Computational Heat Transfer and Fluid Flow, ASCHT 2018, Chennai, India.*
6. Vijaya Kumar, G., Kampili, M., Kelm, S., Arul Prakash, K., & Allelein, H.-J. (2019). Development and verification of a multi-species gas transport solver. *14th OpenFOAM Workshop, Duisburg, Germany.*
7. Kelm, S., Vijaya Kumar, G., Kampili, M., Liu, X., Ji, R., Cammiade, L., George, A., Arul Prakash, K., & Allelein, H.-J. (2019). Technical Scale CFD Analysis of the Pressurization and Transport Processes in the Battelle Model Containment during the ISP 37 VANAM M3 Test. *NUTHOS-13, Hsinchu, Taiwan, September 5-10, 2022.*

ACKNOWLEDGEMENTS

During my Ph.D. study, I received a lot of help from my supervisors and colleagues at IIT Madras, RWTH Aachen, and Forschungszentrum Juelich. I thank each one of them for their invaluable support. First, I would like to thank Prof. Hans-Josef Allelein for supervising my thesis and giving technical and administrative support to complete the Joint Doctoral Program (JDP) between IIT Madras and RWTH Aachen University. I thank Prof. Arul Prakash of IIT Madras for encouraging me to pursue the JDP and supporting me wholeheartedly. I take this opportunity to thank Prof. Reinhold Kneer, Prof. Sarith P. Sathian, and Prof. Prasad Patnaik for reviewing my thesis and providing valuable feedback. I want to give a special mention to Stephan Kelm, who helped me, both technically and administratively, to make a successful JDP. I owe a lot to you.

I thank the DAAD-UGC scholarship for funding the JDP between IIT Madras and RWTH Aachen University. I thank Becker Technologies GmbH for providing me with valuable data on the THAI experiments to validate the models developed during the thesis. I thank IIT Madras and Forschungzentrum Juelich for providing me with the infrastructure necessary to carry out my PhD work seamlessly.

I thank my colleagues at IIT Madras and Forschungszentrum Juelich, who provided a happy environment to carry out my Ph.D. work. Special mention goes to Manohar Kampilli, Xiongguo Liu, Liam Cammiade, Eva Groß, and René Vennemann.

I thank each one of my family members who gave me moral support throughout the time period of my Ph.D. Special mention to my wife, Ramya, who came into my life in the finishing stages of my Ph.D. It was a pretty turbulent time, and I was able to weather it with a great deal of help from her. I owe a lot to my father, who financially and morally supported me during my thesis. Last but not least, I thank my mother, Amul Rani, who has been the guiding light throughout my life. You mean the world to me, Amma.

ABSTRACT

In a severe accident, the prevailing flow in a nuclear reactor containment is driven by buoyancy forces and determines the transport of hydrogen, steam, air, and radioactive fission products—noble gases and aerosol particles. Multiple interacting phenomena such as turbulence, steam condensation, radiation heat transport, and structure-gas heat transfer due to the thermal inertia of steel and concrete structures govern the containment flow. The noble gases and nuclear aerosols carry significant decay heat, which may affect the gas mixing by inducing local buoyancy forces. A previous Ph.D. research project at Forschungszentrum Juelich and RWTH Aachen University analyzed the impact of decay heat on the buoyant flow inside the small-scale DIANA facility (L $\sim$ 0.7 m) with a sophisticated Euler-Lagrangian approach. It was conclusive that the decay heat of aerosol particles influences the gas flow. However, it also became obvious that the Euler-Lagrangian approach is computationally cumbersome for further investigations on a technical scale.

In order to further investigate aerosol transport and the effect of associated decay heat on application scale, in the present work, a "fast-running" CFD model is developed based on the Euler-Eulerian approach to simulate the gas-aerosol transport in a containment. The unsteady-RANS approach, based on the k-ω-SST turbulence model, and a suitable wall condensation model, treat the gas flow. A simplified Eulerian model—*Mixture model*—is used for treating the aerosol transport with the consideration of drag, inertia, buoyancy, thermophoretic, and diffusiophoretic forces. The evolution of particle size distribution due to hygroscopic growth in humid atmospheres is treated with the *Log-normal model* for technical scale applications. The CFD model is systematically validated against small-scale experiments and then against the technical scale THAI experiments (L $\sim$ 9 m and Volume $\sim$ 60 m^3).

For the first time, the aerosol transport and impact of aerosol decay heat on buoyancy-driven mixing processes in the THAI facility is analyzed with a CFD approach. The results show that the decay heat effect significantly impacts the gas mixing phenomenon. Furthermore, the model's scalability to application scale is successfully demonstrated by simulation of the VANAM-M3 experiment (Volume $\sim$ 615 m^3), which involves steam and hygroscopic NaOH aerosol injection followed by a distribution and depletion phase.

KURZFASSUNG

Bei einem schweren Unfall wird die vorherrschende Strömung im Sicherheitsbehälter eines Kernreaktors durch Auftriebskräfte angetrieben und bestimmt den Transport von Wasserstoff, Dampf, Luft und radioaktiven Spaltprodukten - Edelgasen und Aerosolpartikeln. Die Strömung im Sicherheitsbehälter wird durch zahlreiche interagierende Phänomene wie Turbulenz, Dampfkondensation, Wärmetransport durch Strahlung und, aufgrund der thermischen Trägheit von Stahl- und Betonstrukturen, Wärmeübertragung zwischen Struktur und Gas bestimmt. Die Edelgase und nuklearen Aerosole tragen eine beträchtliche Menge an Zerfallswärme mit sich, die die Gasmischung durch lokale Auftriebskräfte beeinflusst. In einem vorangegangenen Dissertation des Forschungszentrums Jülich und der RWTH Aachen wurde daher die Auswirkungen der Nachzerfallswärme auf die freie Zirkulation in der kleinskaligen DIANA-Anlage (L $\sim$ 0,7 m) mit einem detaillierten Euler-Lagrange Ansatz analysiert. Es war schlüssig, dass die Zerfallswärme von Aerosolpartikeln die Gasströmung beeinflusst. Es zeigte sich jedoch auch, dass der Euler-Lagrange Ansatz für weiterführende Untersuchungen im technischen Maßstab zu rechenaufwändig ist.

Zur weiteren Untersuchung des Aerosoltransports und der Auswirkung der damit verbundenen Zerfallswärme im Anwendungsmaßstab wird in der vorliegenden Arbeit ein rechenzeiteffizientes CFD-Modell mittels des Euler-Euler Ansatzes entwickelt, um den Gas-Aerosol-Transport in einem Containment zu simulieren. Der instationäre RANS-Ansatz, unter Nutzung des k-ω-SST Turbulenzmodells, wird zur Behandlung des Aerosoltransports unter Berücksichtigung von Widerstand, Trägheit, Auftrieb, thermophoretischen und diffusiophoretischen Kräften verwendet. Die Entwicklung der Partikelgrößenverteilung aufgrund des hygroskopischen Wachstums in feuchter Atmosphäre wird unter Annahme einer Log-normalen Verteilung für Anwendungen im technischen Maßstab behandelt. Das CFD-Modell wird systematisch anhand von Experimenten im kleinen Maßstab und anschließend anhand der THAI-Experimente im technischen Maßstab (L $\sim$ 9 m, Volumen $\sim$ 60 m^3) validiert.

Zum ersten Mal wird der Aerosoltransport und Einfluss der Nachzerfallswärmefreisetzung auf auftriebsgetriebene Strömungen in der THAI-Anlage mit einem CFD-Ansatz analysiert. Die Ergebnisse zeigen deutlich, dass der Zerfallswärme der aerosolpartikel das Phänomen der Gasmischung erheblich beeinflusst. Darüber hinaus wird die Skalierbarkeit des Modells auf den Anwendungsmaßstab durch die Simulation des VANAM-M3-Experiments (Volumen $\sim$ 615 m^3) erfolgreich demonstriert, bei dem Dampf und hygroskopisches NaOH-Aerosol in eine komplexe Mehrraumgeometrie eingespeist transportiert und abgelagert werden.

TABLE OF CONTENTS

Page

ACKNOWLEDGEMENTS 3

ABSTRACT 5

KURZFASSUNG 6

LIST OF TABLES 10

LIST OF FIGURES 15

1 Introduction 19

1.1 Background and Motivation 19

1.2 Scope of the thesis 22

2 State of the art 25

2.1 Severe accident phenomenology 25

2.1.1 Containment thermal-hydraulics 25

2.2 Containment aerosols 28

2.2.1 Fission product decay heat 29

2.2.2 Experiments on Containment Aerosols 30

2.2.3 CFD approaches 31

3 CFD Modeling Approach 34

3.1 Gas-flow modelling 34

3.1.1 Governing equations 35

3.1.2 Wall condensation modelling 39

3.1.3 Algorithm and solution method 46

3.2 Dispersed phase modeling 48

3.2.1 Multicomponent aerosol 48
3.2.2 Dispersed phase mass fraction equation 49
3.2.3 Evolution of particle size distribution 53
3.2.4 Decay heat modeling 56
3.3 Summary 56

4 Model Validation **57**
4.1 Validation strategy 57
4.1.1 Baseline CFD model 59
4.2 Differentially heated square cavity (DHSC) 60
4.2.1 Experiment 60
4.2.2 CFD setup 60
4.2.3 Discussion of results 61
4.3 Comparison of wall condensation models 70
4.3.1 Convergence behavior 70
4.3.2 Grid sensitivity 70
4.3.3 Mass conservation 71
4.4 SETCOM 73
4.4.1 SETCOM experimental facility 73
4.4.2 Strategy 74
4.4.3 Mesh 74
4.4.4 Results 76
4.5 THAI series 79
4.5.1 Experimental setup 79
4.5.2 Mesh 81
4.5.3 THAI-TH21: Natural convection flow of dry air 82
4.5.4 THAI-TH22 - Natural convection driven helium layer erosion 93
4.5.5 THAI-TH24 - Natural convection driven steam layer erosion . 99

4.6 Particle growth at different relative humidities 109
4.6.1 CFD simulation 109
4.6.2 Discussion of Results 110
4.7 AHMED Experiments 112
4.7.1 Experimental Details 113
4.7.2 CFD simulations 113
4.7.3 Discussion of results 115
4.8 Summary of the CFD model validation 119

5 Applications **121**

5.1 Impact of decay heat 121
5.1.1 CFD Setup 121
5.1.2 THAI-TH22 Results 122
5.1.3 THAI-TH24 Results 127
5.1.4 Summary of the THAI decay heat simulations 132
5.2 VANAM 133
5.2.1 The VANAM M3 Experiment 133
5.2.2 CFD simulation 137
5.2.3 Results 140
5.2.4 Summary of the VANAM-M3 simulation 145

6 Summary and future perspectives **147**

6.1 Summary and Conclusions 147
6.2 Future perspectives 152

LIST OF TABLES

Table	Title	Page
3.1	Boundary conditions at the condensation interface.	46
4.1	Grid convergence study for the DHSC case using the average convective wall heat flux at the hot wall as the parameter ϕ.	64
4.2	Comparison of the species mass conservation errors for the *Volumetric source terms* and *Face-flux* wall condensation models on $y^+ \sim 1$ and $y^+ > 30$ meshes.	72
4.3	Boundary conditions for the three representative cases with different condensation strengths (signified by v^+_{suc}). The steam mass fraction at the condensing wall ($Y_{\text{H}_2\text{O,i}}$) is evaluated from saturation conditions at the interface temperature (T_i).	75
4.4	THAI-TH21: Influence of radiation heat transfer on the volume-averaged quasi-steady pressure & temperature.	87
4.5	Material properties of aerosols	110
4.6	Details of AHMED experiments for Ag, NaOH, CsOH, and CsI aerosols	113
4.7	Growth ratio of different aerosol materials at different relative humidities computed by the CFD model	116
5.1	VANAM: Experimental sequence	135

LIST OF FIGURES

2.1 Schematic of the severe accident phenomenology in a nuclear reactor containment (Bentaïb *et al.*, 2015). 26

2.2 Coupling between the nuclear aerosols and containment flows (Allelein *et al.*, 2009). 30

3.1 Temperature boundary conditions at the condensing interface 'i'—Conjugate heat transfer and Heat transfer coefficient—with heat flux due to convection, condensation and radiation. 41

3.2 Illustration of *Volumetric source terms* (left) and *Face-flux* (right) models, with a two-dimensional control volume. 43

3.3 Streamwise velocity profiles for different suction velocities v^+_{suc}, compared with the law of the wall ($\kappa = 0.41$, $B = 5.5$) and Spalding continuous velocity profile, for turbulent, forced convection flows. . . 45

3.4 Wall condensation model interfacing with the PIMPLE algorithm for segregated solution of transport equations. 47

4.1 Validation matrix: Experiments and the physics covered. 58

4.2 CFD Model - Differentially Heated Square Cavity 60

4.3 Comparison of natural-convection boundary layer profile of DHSC and THAI-TH21 (at heated walls) with the law of the wall typically used for forced convection flows. 62

4.4 Comparison of local Nusselt number on the hot wall between experimental data and simulation results with different near-wall grid resolutions 63

4.5 DHSC - sensitivity of the results to time-step size. a) Velocity transients at the top left corner (x = 0.03m, y = 0.72m) of the domain, b) Transients of the total heat transfer rate from the hot wall into the fluid. 65

4.6 DHSC - influence of convergence criterion on results. a) Velocity profile near the hot wall at mid-height of the cavity (Y=0.5), b) Temperature profile near the hot wall at the mid-height of the cavity. . 65

4.7 DHSC - temperature along the vertical line $X = 0.5$ (middle of the cavity) for simulations with and without radiation heat transfer. 66

4.8 DHSC - contour plot of temperature field for simulations with and without radiation heat transfer. 66

4.9 DHSC - heat flux on the hot and cold walls for simulations with and without radiation heat transfer. 67

4.10 DHSC - temperature distribution across the width of the cavity at $Y = 0.5$. 68

4.11 DHSC - velocity distribution across the width of the cavity at $Y = 0.5$. 68

4.12 DHSC - turbulent kinetic energy distribution across the width of the cavity at $Y = 0.5$. 69

4.13 Grid sensitivity of the *Face-flux* and the *Volumetric source terms* models, based on local fluxes on the condensing wall: total wall heat flux (left top), condensation mass flux (right top), convective wall heat flux (left bottom), and wall shear stress (right bottom). 71

4.14 Schematic of the SETCOM facility (left), a photograph of the facility in vertical position. 74

4.15 Two-dimensional computational domain of the SETCOM channel with different near-wall grid refinement for fine and coarse meshes. 75

4.16 Comparison of the experimental integral heat flux with the fine mesh ($y^+ \sim 1$) and coarse mesh ($y^+ \sim 75$) solutions for 81 forced convection tests in the SETCOM facility. The dotted grey lines indicate a deviation of $\pm 15\,\%$ from the center line (solid grey line). 77

4.17 Local wall fluxes—total wall heat flux (top), convective wall heat flux (middle), wall shear stress (bottom)—along the condensing wall for three cases (differentiated by color) with the fine (solid line) and coarse (dotted-dashed line) meshes. Experimental data is available for the total wall heat flux only (dots). 78

4.18 THAI experiments on buoyancy-driven flows and mixing processes (Gupta *et al.*, 2015). 80

4.19 Simplified geometry of the THAI vessel (sectioned view). 81

4.20 Block-structured mesh of the THAI facility (sectional view) with detailed views: (1) Fine mesh around the injector. (2) Conformal mesh at the fluid (grey) and inner-cylinder (yellow) interface. (3) Conformal mesh at the fluid (grey) and vessel (yellow) interface. 83

4.21 THAI-TH21: Pressure transients 84

4.22 THAI-TH21: Iso-surfaces of instantaneous and time-averaged temperature (colored by velocity magnitude), illustrating the 3D nature of flow-field 85

4.23 THAI-TH21: Time-averaged and circumferentially-averaged streamlines and temperature contour. 86

4.24 THAI-TH21: Heat transfer rates at the external walls for simulations with and without radiation. 87

4.25 THAI-TH21: Temperature variation with height at non-dimensional radius R = 0.952 88

4.26 THAI-TH21: Temperature variation with height at non-dimensional radius R = 0.697 89

4.27 THAI-TH21 - temperature contour of the sump region of THAI vessel (sectioned view) for simulations with radiation (Case 1) and without radiation. 90

4.28 THAI-TH21 - temperature contour of the outer surface of the inner-cylinder for simulations with radiation (Case 1) and without radiation. 90

4.29 THAI-TH21 - velocity profile at Y = 0.533 for simulations with 3D model, with and without radiation. 91

4.30 THAI-TH21 - velocity profile at Y = 0.696 for simulations with axisymmetric model and 3D model, with and without radiation. 92

4.31 THAI-TH22: Helium injection mass flow rate and temperature. 94

4.32 THAI-TH22: Simulated transients of the helium concentration and gas temperature (sectional view). 95

4.33 THAI-TH22: Comparison of the pressure transients between experiment (dotted line) and simulation (solid line). 96

4.34 THAI-TH22: Comparison of the helium concentration transients between experiment (dotted lines) and simulation (solid lines) at different locations along the centerline. 97

4.35 THAI-TH22: Comparison of the gas temperature transients between experiment (dotted lines) and simulation (solid lines) at different locations along the centerline. 98

4.36 THAI-TH24: Comparison of the cooled wall temperature at different heights between experiment (dotted lines) and simulation (solid lines). 101

4.37 THAI-TH24: Steam injection mass flow rate and temperature. 102

4.38 THAI-TH24: Simulated initial temperature contour indicating the quasi-steady-state natural circulation flow field 103

4.39 THAI-TH24: Simulated transients of the steam concentration and gas temperature (sectional view). 104

4.40 THAI-TH24: Comparison of pressure transients between experiment (dotted line) and simulation (solid line). 105

4.41 THAI-TH24: Comparison of the steam concentration transients between experiment (dotted lines) and simulation (solid lines) at different heights along the centerline. 106

4.42 THAI-TH24: Comparison of the gas temperature transients between experiment (dotted lines) and simulation (solid lines) at different heights along the centerline. 107

4.43 THAI-TH24: Comparison of the cumulative steam condensate mass between experiment and simulation. 107

4.44 Growth ratio of CsI aerosols at different relative humidities. 111

4.45 Growth ratio of CsOH aerosols at different relative humidities. 112

4.46 Comparison of experimentally measured Ag aerosol mass concentration transients (solid lines) with the simulation results (dotted lines) at RH = 54% (indicated by color). Experimental uncertainity of $\pm 10\%$ is indicated with the grey shading. 115

4.47 Comparison of experimentally measured NaOH aerosol concentration transients (solid lines) with the simulation results (dotted lines) at different relative humidities (indicated by color). Experimental uncertainity of $\pm 10\%$ is indicated with the grey shading. 117

4.48 Comparison of experimentally measured CsOH aerosol concentration transients (solid lines) with the simulation results (dotted lines) at different relative humidities (indicated by color). Experimental uncertainity of $\pm 10\%$ is indicated with the grey shading. 118

4.49 Comparison of experimentally measured CsI aerosol concentration transients (solid lines) with the simulation results (dotted lines) at different relative humidities (indicated by color). Experimental uncertainity of $\pm 10\%$ is indicated with the grey shading. 119

5.1 Transients of helium concentration contours for the fundamental THAI-TH22 simulation without aerosol injection (top) vs. the THAI-TH22 simulation with CsI aerosol particles carrying decay heat (bottom). . . 123

5.2 Transients of gas temperature contours for the fundamental THAI-TH22 simulation without aerosol injection (top) vs. the THAI-TH22 simulation with CsI aerosol particles carrying decay heat (bottom). . . 124

5.3 Transients of helium concentration profiles for the fundamental THAI-TH22 simulation without aerosol injection (solid lines) vs. the THAI-TH22 simulation with CsI aerosol particles carrying decay heat (dashed lines). 125

5.4 Transients of pressure (blue) and volume-averaged gas temperature profiles (red) for the fundamental THAI-TH22 simulation without aerosol injection (solid lines) vs. the THAI-TH22 simulation with CsI aerosol particles carrying decay heat (dashed lines). 126

5.5 Transients of steam concentration contours for the fundamental THAI-TH24 simulation without aerosol injection (top) vs. the THAI-TH24 simulation with CsI aerosol particles carrying decay heat (bottom). . . 128

5.6 Transients of gas temperature contours for the fundamental THAI-TH24 simulation without aerosol injection (top) vs. the THAI-TH24 simulation with CsI aerosol particles carrying decay heat (bottom). . . 128

5.7 Transients of steam concentration profiles for the fundamental THAI-TH24 simulation without aerosol injection (solid lines) vs. the THAI-TH24 simulation with CsI aerosol particles carrying decay heat (dashed lines). 129

5.8 Transients of pressure (blue) and volume-averaged gas temperature profiles (red) for the fundamental THAI-TH24 simulation without aerosol injection (solid lines) vs. the THAI-TH24 simulation with CsI aerosol particles carrying decay heat (dashed lines). 130

5.9 Transients of the cumulative condensate mass for the fundamental THAI-TH24 simulation without aerosol injection (solid lines) vs. the THAI-TH24 simulation with CsI aerosol particles carrying decay heat (dotted lines). 131

5.10 Transients of the 'upper cooled' wall temperatures at different heights for the fundamental THAI-TH24 simulation without aerosol injection (solid lines) vs. the THAI-TH24 simulation with CsI aerosol particles carrying decay heat (dashed lines). 132

5.11 VANAM: Geometry of the Batelle Model Containment (BMC) with the different compartments/rooms (left) and the locations of gas/aerosol injection, and the gas flow path showing interconnections between rooms (right). 134

5.12 VANAM: Pressure evolution and mass balance of the gas during the different phases of the experiment. 136

5.13 VANAM: Sectional view of the hex-dominant mesh with mesh quality statistics. 138

5.14 VANAM: Temperature and steam distribution estimated as initialization for 'phase 2' (1st aerosol injection). 140

5.15 VANAM: Transient evolution of pressure and non-condensable gas (air) mass. 141

5.16 VANAM: Transient evolution of the simulated gas temperature during the 1st injection and dry depletion phase. 142

5.17 VANAM: Comparison of gas temperature transients between the experiment (circle) and simulation (solid lines). Color coding indicates the measurement locations. 144

5.18 VANAM: Transient evolution of the simulated NaOH aerosol concentration during the 1st injection and dry depletion phase. 144

5.19 VANAM: Comparison of NaOH aerosol concentration transients between the experiment (circle) and simulation (solid lines). Color coding indicates the measurement locations. 145

Nomenclature

Greek symbols

α	laminar thermal diffusivity of the gas mixture ($\mathrm{m^2\,s^{-1}}$)
α_{eff}	effective thermal diffusivity of the gas mixture ($\mathrm{m^2\,s^{-1}}$)
α_k	thermal diffusivity of kth gas species ($\mathrm{m^2\,s^{-1}}$)
α_t	turbulent thermal diffusivity of the gas mixture ($\mathrm{m^2\,s^{-1}}$)
δ	Kronecker delta
λ	laminar thermal conductivity of the gas mixture ($\mathrm{W\,m^{-1}\,K^{-1}}$)
λ_{eff}	effective thermal conductivity of the gas mixture ($\mathrm{W\,m^{-1}\,K^{-1}}$)
λ_k	thermal conductivity of kth gas species ($\mathrm{W\,m^{-1}\,K^{-1}}$)
μ	dynamic viscosity of the gas mixture ($\mathrm{Pa\,s}$)
μ_k	dynamic viscosity of kth gas species ($\mathrm{Pa\,s}$)
ν	kinematic viscosity of the gas mixture ($\mathrm{m^2\,s^{-1}}$)
ν_t	eddy viscosity ($\mathrm{m^2\,s^{-1}}$)
ω	turbulence eddy frequency ($\mathrm{s^{-1}}$)
ρ	density of the gas mixture ($\mathrm{kg\,m^{-3}}$)
τ	viscous stress tensor ($\mathrm{N\,m^{-2}}$)
τ_w	wall shear stress ($\mathrm{N\,m^{-2}}$)

Alphabets

$\vec{\dot{q}}''$	heat flux vector ($\mathrm{W\,m^{-2}}$)
$\vec{\dot{q}}''_{\text{rad}}$	radiation heat flux vector ($\mathrm{W\,m^{-2}}$)
$\vec{g}$	gravity vector ($\mathrm{m\,s^{-2}}$)
$\vec{n}_i$	unit outward facing normal to the interface i

$\vec{S}_{\text{mom}}$ volumetric source term for the momentum conservation equation ($\mathrm{N\,m^{-3}}$)

A_i face area of the interface i ($\mathrm{m^2}$)

$c_{p,k}$ specific heat capacity of kth gas species ($\mathrm{J\,kg^{-1}\,K^{-1}}$)

D_{jk} binary diffusivity of the species pair $j-k$ ($\mathrm{m^2\,s^{-1}}$)

$D_{k,\text{eff}}$ effective diffusivity of kth gas species ($\mathrm{m^2\,s^{-1}}$)

$D_{k,m}$ molecular diffusivity of kth gas species ($\mathrm{m^2\,s^{-1}}$)

$D_{k,T}$ thermal diffusion coefficient of kth gas species ($\mathrm{kg\,m^{-1}\,s^{-1}}$)

$D_{k,t}$ turbulent diffusivity of kth gas species ($\mathrm{m^2\,s^{-1}}$)

h static enthalpy of the gas mixture ($\mathrm{J\,kg^{-1}}$)

h_k specific enthalpy of kth gas species ($\mathrm{J\,kg^{-1}}$)

$h_{\text{ref},k}$ specific enthalpy of kth gas species at T_{ref} ($\mathrm{J\,kg^{-1}}$)

HTC heat transfer coefficient ($\mathrm{W\,m^{-2}\,K^{-1}}$)

J_k diffusive mass flux of kth gas species ($\mathrm{kg\,m^{-2}\,s^{-1}}$)

K specific kinetic energy of the mean flow ($\mathrm{J\,kg^{-1}}$)

Kn Knudsen number

p pressure (Pa)

Pr_t turbulent Prandtl number, Pr_t = 0.9

R_u universal gas constant, $R_u = 8314.5\,\mathrm{J\,kmol^{-1}\,K^{-1}}$

S list of all the gas species in the mixture

S_{m} volumetric source term for the total mass conservation equation ($\mathrm{kg\,m^{-3}\,s^{-1}}$)

S_{Y_k} volumetric source term for mass conservation equation equation of kth species ($\mathrm{kg\,m^{-3}\,s^{-1}}$)

Sc_t turbulent Schmidt number, Sc_t = 0.9

T temperature (K)

T_{ref} reference temperature (K)

u^+ dimensionless streamwise velocity

u_τ friction velocity ($\mathrm{m\,s^{-1}}$), $u_\tau = \sqrt{\tau_w/\rho}$

v^+_{suc} dimensionless suction velocity, $v^+_{\text{suc}} = \vec{U}_i \cdot \vec{n}_i / u_\tau$

V_c volume of the cell (control volume) adjacent to the interface i ($\mathrm{m^3}$)

W molar mass of the gas mixture ($\mathrm{kg\,kmol^{-1}}$)

W_k molar mass of kth gas species ($\mathrm{kg\,kmol^{-1}}$)

x, y Cartesian coordinates (m)

X_k molar fraction or volume fraction of kth gas species

y^+ dimensionless wall normal distance, $y^+ = y u_\tau / \nu$

$\dot{m}''_i$ condensation mass flux ($\mathrm{kg\,m^{-2}\,s^{-1}}$)

$\dot{m}''_{k,i}$ mass flux of kth gas species at the condensing interface ($\mathrm{kg\,m^{-2}\,s^{-1}}$)

Ma Mach number of the fluid flow

Subscripts

c centre of the control volume adjacent to the condensing interface i

j, k indices of individual gas species

t turbulence component

w wall

sat vapor saturation condition

CHAPTER 1

Introduction

1.1 BACKGROUND AND MOTIVATION

In the event of a severe accident, e.g., a loss of coolant (LOCA) with core degradation, reactor containment is the final barrier preventing the release of radioactive material into the environment. The containment building can fail in multiple ways during a core-melt accident. In the in-vessel phase, pressure rises in the containment because of steam release from the cooling system of the reactor pressure vessel (Bentaïb *et al.*, 2015). The high-temperature steam also causes the exothermic oxidation of the control rod materials, resulting in rapid generation of hydrogen in the reactor pressure vessel, which is subsequently released into the containment, causing more pressurization. Hydrogen also accumulates in the containment and may form locally flammable mixtures, resulting in dynamic loads on the containment through detonation or deflagration (Bentaïb *et al.*, 2015). During the ex-vessel phase, the molten corium interacts with the concrete basemat of the containment (known as Molten Core Concrete Interactions (MCCI)), releasing gases; thus, further pressurization. Also, the corium, when it comes in contact with any water present in the reactor pit, may result in either slow vaporization of steam (slow pressurization) or steam explosion (rapid pressure increase) (Bentaïb *et al.*, 2015).

The severe accidents at the Fukushima Daiichi nuclear power plant site have confirmed the need to understand the gas transport and mixing processes in a containment (Amano, 2015). To prevent dynamic loads on the containment building due to hydrogen detonation/deflagration, hydrogen mitigation methods such as passive autocatalytic recombiners (PARs) are usually employed (OECD-NEA, 2015). For effective positioning of PARs, the hydrogen gas distribution in a containment should be predicted for multiple possible accident scenarios. System codes or 1D lumped parameter codes, e.g., COCOSYS (Allelein *et al.*, 2008), are typically used to model the containment thermal–hydraulics. The lumped parameter codes are well established and successfully predict the pressure history of the containment, average steam content, and hydrogen distribution (Karwat *et al.*, 1999). But the hydrogen gas distribution obtained from the lumped-parameter codes suffers from high numerical diffusion due to coarse nodalization. Thus, this information cannot be a basis for 3D combustion load analysis. Computational Fluid Dynamics (CFD) scores over lumped-parameter codes in that; it

can provide three-dimension, high-resolution (less numerically diffusive) data on gas distributions which can serve as a basis for local combustion load analysis in a reactor containment (Smith *et al.*, 2015).

During a severe accident, e.g., a loss of coolant accident (LOCA) with core damage, the containment thermal hydraulics is governed by multiple interacting phenomena: Multi-component gas system (N_2, O_2, H_2, H_2O, CO, and CO_2), turbulence, mixed convection flow regime, gas-wall heat transfer (convection, condensation, and radiation) (Karwat *et al.*, 1999). In the past, commercial CFD codes have been successfully developed to capture the containment thermal hydraulics and thoroughly validated against technical scale experiments (Kelm *et al.*, 2016*a*,*c*,*b*; Dehbi *et al.*, 2019). Despite their success, commercial CFD codes have limited access to the source code; therefore, it is difficult to verify the implementation of different models, affecting the reliability of simulation results. In recent years at Forschungzentrum Juelich, a tailored CFD solver *containmentFOAM*, based on open-source CFD package *OpenFOAM®*, has been developed to simulate the containment thermal hydraulics (Kelm *et al.*, 2021). The high computational cost is the major challenge for using CFD in containment applications. Thus major efforts need to be taken to establish a well-balanced CFD model set, i.e., computationally efficient and at the same time provides reliable results. While the primary objective of this thesis is to analyze the impact of aerosol transport and decay heat on containment thermal hydraulics, considerable effort has been spent on implementing numerically efficient models in the framework of *containmentFOAM*, e.g., turbulence model (Kumar *et al.*, 2020), wall condensation with conjugate heat transfer (Vijaya Kumar *et al.*, 2021).

Aerosols reach the containment through multiple sources: a leak in the reactor coolant system, from the molten core after the failure of the reactor pressure vessel, during MCCI events, or re-entrainment from boiling sumps. Because of the multiple sources, a typical nuclear aerosol comprises numerous materials, i.e., fission products, control rod materials, and concrete constituents. The aerosols, reaching the containment, are transported and distributed by the prevailing atmospheric flows. Locally different thermal-hydraulic conditions are present in a containment. In some parts, the gas mixing is limited by stable gas stratifications. Few containment compartments may be excluded from the gas mixing, e.g., dead-end rooms. Due to this variation in gas mixing between the different parts of the containment, the aerosol concentration is not uniform. Though, the average aerosol concentration is estimated to be around 1 $\mathrm{g\,m^{-3}}$, local

concentrations can reach up to 100 $\mathrm{g\,m^{-3}}$ (Allelein *et al.*, 2009). Aerosol concentration in the containment atmosphere is governed by the competing wall deposition and re-suspension processes. The deposition is mainly caused due to gravitational settling (sedimentation), diffusiophoresis, thermophoresis, and Brownian diffusion phenomena. Aerosols re-suspend from the walls due to local hydrogen deflagration (Allelein *et al.*, 2009). The gas flow usually carries aerosol particles, but they also have a slip velocity with respect to the gas phase, depending on their size (inertia). The aerosol particle size distribution (PSD) in a containment is mainly influenced by steam condensation on particles and agglomeration. When the containment atmosphere is super-saturated (RH > 100%), the steam condenses on the aerosol particle, resulting in their growth and subsequently faster depletion. Due to the presence of hygroscopic material, e.g., CsOH, CsI, in a typical nuclear aerosol, the steam condenses on particles even at sub-saturated (RH < 100%) conditions (Jokiniemi, 1990). Depending on the local aerosol concentration, smaller-sized particles coalesce to form larger particles, thereby affecting the depletion behavior.

Diffusiophoresis causes a differential force on the particle due to gas mass concentration gradients. These concentration gradients exist near cold containment structures where steam condenses. Thermophoresis results in an additional force on aerosol particles due to temperature gradients and is significant near the cold containment structures. Unlike gravitational settling, diffusiophoresis and thermophoresis is independent of particle size (Allelein *et al.*, 2009). Brownian diffusion is a vital deposition process of sub-micron-sized aerosol particles.

In addition to the radioactive gases (e.g., I-131), aerosols also account for a significant proportion of fission product decay heat (Allelein *et al.*, 2009). The decay heat of aerosols in the containment atmosphere increases the local gas temperature and reduces the local humidity. Consequently, this affects the steam condensation on aerosols and their settling behavior. Aerosols deposited on the containment walls are washed down by the condensate flow and reach the sump. Due to decay heat, it may cause the evaporation of sump water and hence increases the relative humidity closer to the sump. Aerosol's decay heat affects the containment thermal hydraulics, and in turn, the thermal hydraulics affect the aerosol depletion behavior resulting in a tightly coupled system.

1.2 SCOPE OF THE THESIS

In the past, experiments and simulations concerning containment aerosols were focused on assessing the radioactive source term in the containment atmosphere. The studies relating to aerosol decay heat's impact on containment thermal hydraulics are limited. The state-of-the-art report on nuclear aerosols mentions that the decay heat of fission products (aerosols and gases) influences the containment thermal hydraulics (Allelein *et al.*, 2009). Kelm *et al.* (2014), through a system code analysis of the containment of a German pressurized water reactor (1300 MW_{el}), concluded that the decay heat had an impact on pressure evolution and thermal-hydraulics in the containment building. Consequently, a Ph.D. project at RWTH Aachen University and Forschungzentrum Juelich studied the influence of aerosol decay heat on the buoyancy-driven flows in the small-scale DIANA facility (L $\sim$ 0.7 m) (Kampili, 2022). The flow field had mild turbulence (Ra $\sim 10^9$). The decay heat was modeled as a source term (100 $\mathrm{W\,m^{-3}}$) in the gas phase based on the local aerosol concentration. The author used a CFD approach based on the Euler-Lagrangian method—Eulerian framework for the gas phase and a Lagrangian particle tracking method for the aerosol particles. The influence of drag, gravity, thermophoresis, and turbophoresis accounted for the particle transport. The research concluded that the decay heat of aerosols affected the gas flow field, turbulence levels, and particle deposition on the walls.

Even though the Euler-Lagrangian approach used by Kampili (2022) is accurate, it is computationally expensive and infeasible for containment scale applications. Therefore, a computationally efficient CFD model is necessary to analyze an actual containment accident sequence, and the present thesis aims to fill this gap. The primary objective of this thesis is to develop a well-balanced CFD code to analyze the impact of aerosol decay heat on buoyancy-driven gas mixing in technical scale geometries.

The literature review revealed that the *Mixture model*, based on the Euler-Eulerian approach, is suitable for the containment applications (Manninen *et al.*, 1996). In addition to the drag, inertia, and buoyancy forces, the containment-specific force components such as thermophoresis, diffusiophoresis, and Brownian diffusion are considered. The present work does not consider the resuspension of particles from the walls, and the aerosol particles deposited on the walls are removed from the computational domain. In the preceding work with the Lagrangian framework, the aerosol particle is treated as a single-component, monodisperse system (Kampili, 2022). The current work treats the aerosol as a multi-component, polydisperse system,

mimicking a typical nuclear aerosol (Frederix, 2016). The evolution of particle size distribution is treated primarily with a *Log-Normal* method, based on the Method of Moments model (Lucci *et al.*, 2022). The particle size distribution is affected mainly by the growth of aerosol particles due to steam condensation and the agglomeration of smaller-sized particles into larger particles. Even though agglomeration is an important phenomenon, the discussion in this thesis is restricted to particle growth in a humid containment atmosphere.

The model implementations are in the framework of *containmentFOAM* CFD solver, based on open-source code, OpenFOAM (Kelm *et al.*, 2021). First, the gas transport solver, covering the containment thermal-hydraulic phenomena such as turbulence, buoyancy-driven flow, multicomponent gas transport, conjugate heat transfer with condensation, convection, and radiation heat transfer, is thoroughly validated against small-scale (Ampofo and Karayiannis, 2003; Kelm *et al.*, 2019*b*) and technical scale experiments (Gupta *et al.*, 2015). Subsequently, the aerosol transport models for hygroscopic growth and gravitational settling are validated against the experiments conducted in the AHMED facility (Mäkynen *et al.*, 1997).

Nuclear aerosols release the decay heat into the gas phase, affecting local buoyancy-driven gas mixing and containment pressurization. Aerosols that get deposited on containment walls affect the local steam condensation. Also, aerosol particles that get washed down into the sump through condensate flows cause the evaporation of water in the sump, thereby influencing containment pressurization and gas composition. As a first step, this thesis considers only the direct release of aerosol decay heat into the containment atmosphere.

The thesis is organized as follows. The next chapter, state of the art, discusses experiments and modeling approaches for gas and aerosol transport in containment applications. Subsequently, chapter 3 discusses the CFD models employed in the present thesis to simulate particle-laden gas flows in a containment. Justifications for choosing specific approaches are also provided. In Chapter 4, the above models are systematically validated against small-scale and technical-scale experiments. To achieve the objectives of this thesis, in Chapter 5, CFD simulations are performed to analyze the impact of decay heat on gas-mixing in the technical-scale THAI facility. Also, a first attempt has been made to simulate the VANAM M3 experiment conducted in the large-scale Battelle Model Containment (Volume = 615 m^3) to demonstrate

the CFD model's performance on real applications (Kanzleiter, 1993). Chapter 6 summarizes the thesis and also presents the way forward.

CHAPTER 2

State of the art

2.1 SEVERE ACCIDENT PHENOMENOLOGY

A severe accident means accident conditions more severe than a design basis accident and involving significant core degradation (Bentaïb *et al.*, 2015). During the in-vessel phase of the severe accident, the loss of cooling results in the uncovering of the core. Since the decay heat generated by the core is not sufficiently removed, the temperature of the fuel rod and the Zircalloy cladding increases. At a temperature of 900 °C, the cladding material swells and ruptures, and the fission gases inside the fuel rod (e.g., Xenon and Krypton) are released into the reactor coolant system (RCS). At a temperature of above 1200 °C, the Zircalloy material in the fuel rod cladding oxidizes on contact with the super-heated steam, releasing large amounts of hydrogen gas, which can enter the reactor containment through the breaks in the RCS or the pressurizer relief valve (Bentaïb *et al.*, 2015). The oxidation is a highly exothermic reaction, increasing the local material temperatures and hence causes further oxidation of the cladding material and fuel heat-up. Between 1200-1800 °C, the control rod components, steel, and Zircalloy cladding melt. At around 2850 °C, the Uranium oxide components melt, resulting in the formation of a molten corium pool, which relocates to the RPV lower plenum, where it can interact with remaining water, resulting in rapid vaporization, a so-called steam explosion. Otherwise, the continuous heat transfer weakens the RPV wall, and if it cannot be cooled from outside, this will finally lead to RPV failure.

The so-called ex-vessel phase begins with the melt relocation to the reactor pit. There may be again the risk of a steam explosion if the cavity is flooded. Otherwise, the molten corium concrete interaction (MCCI), i.e., the decomposition of the basemat concrete, will begin and release further hydrogen, steam, carbon monoxide, and carbon dioxide gases to the containment. Eventually, the penetration of the basemat is possible. The accident phenomenology is described in Figure 2.1.

2.1.1 Containment thermal-hydraulics

In the event of a severe accident, the reactor containment is the final barrier preventing the release of radioactive material to the external environment. The pressure within the containment has to be maintained within its design limits to prevent containment

failure. Release of hydrogen, steam, and other non-condensable gases from the reactor pressure vessel (RPV) causes slow pressurization, whereas hydrogen combustion or steam explosion result in dynamic loads on the containment building. Immediately after the blow-down phase, the containment flow is driven by the temperature differences between the structures, e.g., hot reactor pressure vessel and cold concrete structures. Therefore, a natural circulation flow field is typical of a nuclear reactor containment. Hydrogen gas, because of its low density, gets accumulated in the top part of the containment and form a stably stratified layer. Based on the level of density stratification, the natural convection flow field is either suppressed or enhanced (Karwat *et al.*, 1999).

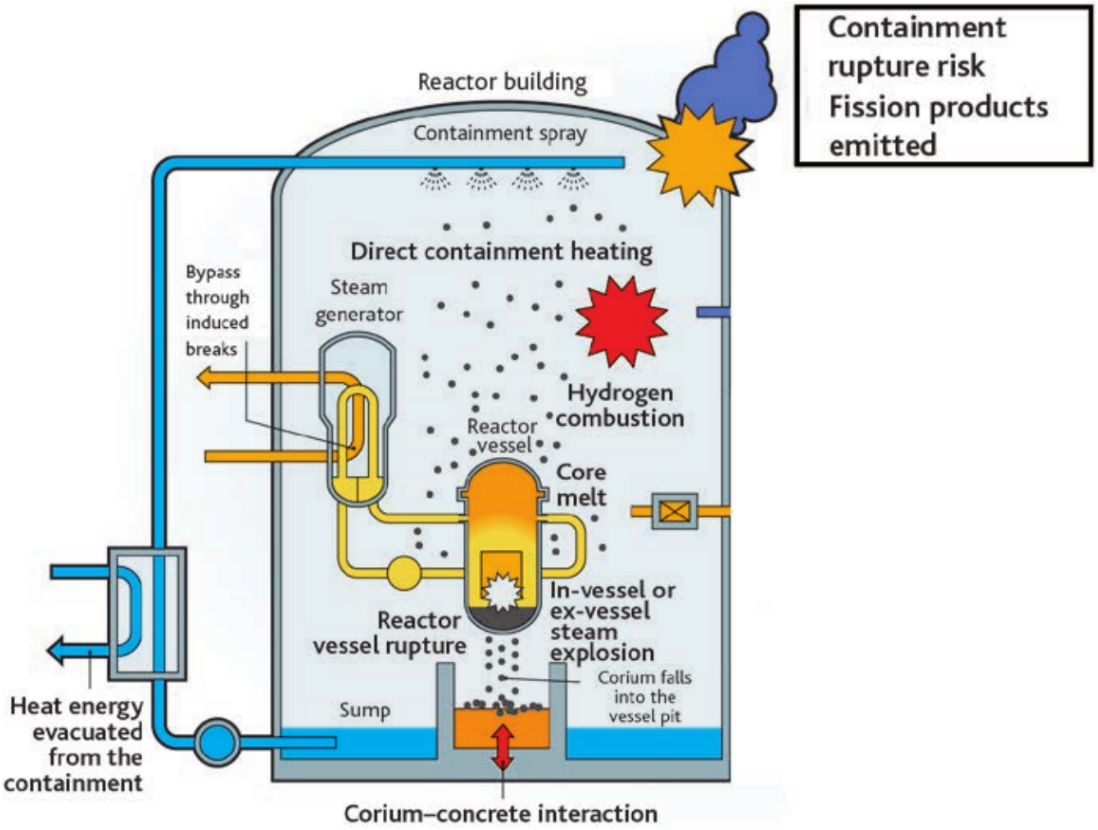

Figure 2.1: Schematic of the severe accident phenomenology in a nuclear reactor containment (Bentaïb *et al.*, 2015).

During a severe accident, along with hydrogen, lots of steam are released into the containment. Steam brings in two-phase effects due to its condensation in the bulk, and on the containment structures. The composition of hydrogen-steam-air mixture influences the hydrogen combustion. Steam condensation in the bulk and on the walls

also reduce the containment pressure. Therefore, the wall condensation of steam is an important phenomenon in this context. Apart from the hydrogen stratification and steam condensation, the containment thermal-hydraulics is influenced by the containment geometry itself. A typical containment is a multi-compartmented geometry with multiple structures that can affect the flow field. Several experiments were performed in the past in large scale and small scale facilities to understand the gas flow and mixing processes in a containment (Allelein *et al.*, 2007; Gupta *et al.*, 2015; Studer *et al.*, 2012; Auban *et al.*, 2007; Kelm *et al.*, 2019*b*).

To summarize, the flow prevailing in a nuclear reactor containment in the event of a severe accident is turbulent, buoyancy-driven, multiphase flow with a multicomponent gas mixture (H_2, H_2O, N_2, and O_2). Conjugate heat transfer also prevails due to the thermal inertia of steel and concrete containment structures (Karwat *et al.*, 1999).

2.1.1.1 Simulation approaches

Several safety systems, such as, Passive Auto-catalytic Recombiners (PARs), Filtered Containment Venting System (FCVS), are available to mitigate the risk of containment pressurization or hydrogen combustion. But for effective use of these systems, the containment thermal hydraulics should be correctly predicted for postulated accident scenarios. Lumped parameter (LP) codes, e.g., COCOSYS (Allelein *et al.*, 2008), are typically used to predict the containment thermal hydraulics. The LP codes have been sufficiently validated against small scale and large scale experiments. They have been shown to predict the pressure transients and gas mixing processes accurately (Allelein *et al.*, 2007). But the lumped parameter codes use coarse nodalization—control volume sizes are of the order of 100 to 1000 m^3, preventing detail insights on the flow field. Computational Fluid Dynamics (CFD) approaches can provide highly resolved data, which can form a basis for H_2 combustion analyses. Allelein *et al.* (2007) concluded that the lumped parameter codes should be used to run accident sequences and the CFD simulations to be used for detailed analysis.

Owing to the large scale geometry, scale resolving CFD approaches such as LES and DNS are not applicable to simulate containment flows. Therefore, an unsteady-RANS approach (uRANS) is only feasible for modelling the turbulence. This approach has been applied by various authors in the past to simulate containment thermal hydraulics and no major modeling discrepancies were reported (Kelm *et al.*, 2016*a*,*c*,*b*; Dehbi *et al.*, 2019). In recent years at Forschungzentrum Juelich, a tailored CFD

solver *containmentFOAM*, based on open-source CFD package *OpenFOAM®*, has been developed to simulate the containment thermal hydraulics (Kelm *et al.*, 2021). The main aim of this Ph.D. thesis is to develop a computationally efficient and a reliable CFD solver to simulate the gas-aerosol transport in a containment. As a first step, the gas transport modelling part is thoroughly validated against small scale (Ampofo and Karayiannis, 2003; Kelm *et al.*, 2019*b*) and technical scale experiments (Gupta *et al.*, 2015).

2.2 CONTAINMENT AEROSOLS

During a severe accident, volatile fission products are formed in the degrading core and pass through the reactor coolant system (RCS). Due to the colder condition of RCS, the fission products nucleates as aerosols. A significant proportion of these aerosol particles deposit on the coolant pipes owing to high flow velocities (turbulence) and thermophoresis (Allelein *et al.*, 2009). The remaining aerosols reach the containment. Aerosols are also generated in the containment during the MCCI interactions. Aerosols are also re-entrained from boiling sumps into the containment atmosphere. Due to the multiple sources, a typical containment aerosol is composed of numerous materials, e.g., fission products, control rod materials, core structure materials, and concrete constituents (Jokiniemi, 1990).

Due to the presence of fission products, the aerosol concentration in the containment atmosphere forms a significant proportion of the radioactive source term. The concentration transients of the aerosols in the containment atmosphere are governed by the balance between particle deposition on containment structures, aerosol generation by re-entrainment from boiling sumps, and particle resuspension from the walls. Particle deposits on the containment structures are mainly through sedimentation or gravitational settling. Other possible reasons for deposition include thermophoresis and diffusiophoresis phenomena.

The gravitational settling of particles is a function of the particle size distribution (PSD). The aerosol prevailing in the containment has a wide size distribution—from 0.1 μm to 10 μm. Larger particles settle faster under gravity because of their weight, whereas the smaller particles remain suspended in the containment atmosphere for a long duration. The evolution of PSD is governed by multiple phenomena: agglomeration/coalescence, de-agglomeration, particle growth by steam condensation, and resuspension from the

containment walls. The average aerosol concentration in the containment atmosphere is only 1 $\mathrm{g\,m^{-3}}$, but local concentrations can reach up to 100 $\mathrm{g\,m^{-3}}$ (Allelein *et al.*, 2009). Mass concentration (consequently, the number concentration) determines the significance of agglomeration. If the containment atmosphere is super-saturated (relative humidity > 100%), the steam condenses on the aerosol particles, affecting the PSD. Also, a typical nuclear aerosol is composed of hygroscopic material, e.g., CsI or CsOH, which absorbs water even in sub-saturated conditions (relative humidity < 100%). Depending on the local hydrogen gas concentration, deflagration may happen. The violent local flow caused due to deflagration may remove the particles suspended on the containment structures, i.e., resuspension. In the context of containment aerosols, the resuspension phenomenon is less significant than agglomeration or steam condensation (Allelein *et al.*, 2009).

In the initial phase of a severe accident, a containment's concrete and steel structures are colder than the gas atmosphere (Karwat *et al.*, 1999). This has two effects: 1) Strong temperature gradients between the gas and the structures. 2) Steam condenses on the structures resulting in gas mass concentration gradients. The aerosol particles experience differential forces due to these gradients—thermophoresis due to temperature gradients and diffusiophoresis due to concentration gradients (Allelein *et al.*, 2009). These additional forces affect the deposition process.

2.2.1 Fission product decay heat

Fission products—noble gases and aerosols—continue releasing decay heat into the containment atmosphere because of their radioactivity. The decay heat, absorbed by the gas phase, affects the local buoyancy forces through the change in gas temperature (Allelein *et al.*, 2009). Also, the relative humidity in the atmosphere changes based on aerosol concentration. Because of the generation of local buoyancy forces in the gas phase, the atmospheric flows in the containment get affected. Due to changes in relative humidity, the particle growth due to steam condensation changes, which affects the aerosol depletion rate. Aerosols deposited on containment walls with wet films get washed down to the sump by condensate flows. The decay heat carrying aerosols causes evaporation of sump water and thereby enhancing the relative humidity in the containment atmosphere. Figure 2.2 explains the tight coupling of the fission product decay heat with the containment flows.

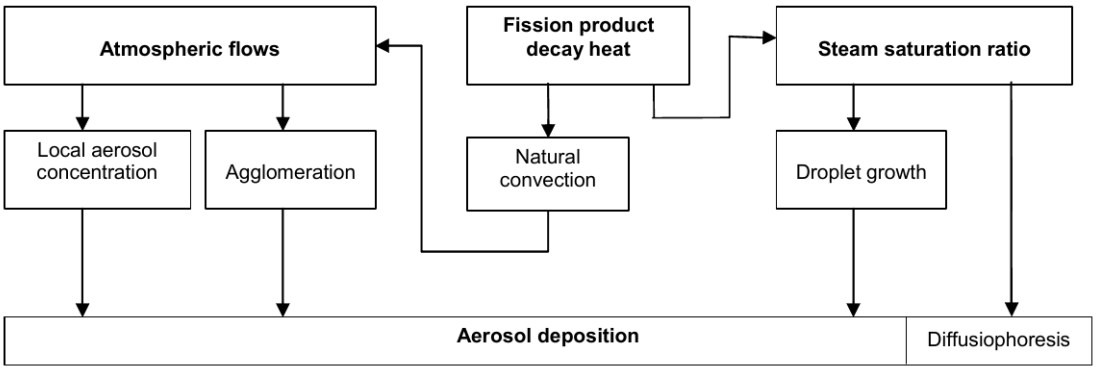

Figure 2.2: Coupling between the nuclear aerosols and containment flows (Allelein *et al.*, 2009).

There are multiple interacting phenomena concerning aerosol transport in a containment. The main aim of this thesis is to develop a CFD model to analyze the impact of decay heat on the buoyancy-driven flows in a containment. The amount of decay heat released in the containment atmosphere is proportional to the aerosol concentration remaining in the gas phase. The aerosol depletion rate, in turn, depends on the evolution of the particle size distribution (PSD): Agglomeration and the steam condensation on aerosols are important phenomena in this context (Allelein *et al.*, 2009). Agglomeration is critical in regions of high particle concentration, but the size distribution is always affected by particle growth due to steam condensation. In this thesis, only the PSD change due to steam condensation is sought as a first step.

2.2.2 Experiments on Containment Aerosols

Kampili (2022) summarized the different experiments on nuclear aerosols based on the geometry scale and the different phenomena covered. In the present work, only the steam condensation of particles is considered for the evolution of size distribution. Hence, only those experiments relevant to particle growth due to steam condensation is discussed here.

The LACE experiments were conducted in a single volume compartment of 852 m^3 (Mäkynen *et al.*, 1997). The gravitational settling of both inert and hygroscopic aerosols is studied. The pressure, temperature (gas and wall), relative humidity, and particle size distribution were monitored.

VANAM experiments were conducted in the 'Batelle Model Containment', which is a 626 m^3, multi-compartmented geometry (Kanzleiter, 1993). The gravitational

depletion of both the soluble (hygroscopic) and inert aerosol materials was studied. Multiple interacting phenomena typical of nuclear reactor containment, such as steam condensation, hygroscopic aerosol (NaOH), the thermal inertia of the concrete structures (conjugate heat transfer), and buoyancy-driven flow, were present in the experiment.

The problem with the large-scale geometries of the VANAM and LACE experiments was that the thermal hydraulic conditions (relative humidity and temperature) were not uniform. Therefore, these experiments were not suitable for validating the separate effect—hygroscopic growth of aerosols. To remove modeling uncertainties, well-controlled thermal hydraulic conditions (relative humidity and temperature) are needed.

The PITEAS experiments were performed in a 2.9 m^3 vessel with well-controlled thermal-hydraulic conditions (temperature and relative humidity). The depletion behavior of the hygroscopic CsI aerosols was studied.

In the AHMED experiments performed by VTT, Finland, the aerosol depletion behavior was studied in a small-scale 1.8 m^3 facility, with well-defined thermal-hydraulic conditions (uniform pressure and temperature) (Mäkynen *et al.*, 1997). Compared to the PITEAS experiments, where single hygroscopic material was studied, the AHMED experiments used multiple hygroscopic materials, i.e., CsI, CsOH, and NaOH. Also, the depletion behavior of inert silver aerosols was studied. In the present Ph.D. thesis, the AHMED experiments are used to validate the CFD model pertaining to hygroscopic aerosol growth and the gravitational settling behavior.

2.2.3 CFD approaches

The aerosol particle is the dispersed phase in a containment flow, with the gas being the continuous phase. Based on the treatment of the dispersed phase, there are two CFD approaches: Euler-Lagrangian and Euler-Eulerian. The gas phase is always treated with the Eulerian framework. The dispersed phase can either be treated with a Lagrangian or Eulerian framework. With the Lagrangian approach, the force balance is performed on the individual aerosol particle, and its movement through space is tracked with time (Dehbi, 2008). The Eulerian approach solves a concentration equation for the dispersed phase, similar to the continuous phase (Riella *et al.*, 2018). The Lagrangian model is numerically accurate and offers resolved insights into particle dynamics. But the computational cost of the Lagrangian approach increases based on the number of

particles tracked. The Eulerian method requires reduced computational cost, but its application is limited to dense particle concentrations.

In a nuclear reactor containment, the particle concentration is typically dilute ($1\ \mathrm{g\,m^{-3}}$) and hence, the Euler-Eulerian approach is not strictly applicable. Consequently, an Euler-Lagrangian approach was used in the preceding work to simulate the gas-aerosol transport (Kampili, 2022). The thesis concluded that the Euler-Lagrangian approach is to be used for getting detailed insights, but a cheaper alternative should be sought for technical scale applications.

In the literature, a simplified Euler-Eulerian model (Mixture model) is available for treating dilute dispersed phase concentrations (Manninen *et al.*, 1996). This method is also called the drift-flux approach, where the particle phase has a drift (relative) velocity with respect to the continuous phase. Manninen *et al.* (1996) mentioned that the model is suitable when the continuous phase is liquid and not for high-velocity gas flows. The flow prevailing in the containment is of low speed, and since a computationally efficient model is required, the Mixture model is used in the present Ph.D. thesis.

2.2.3.1 Particle size distribution

The evolution of particle size distribution in a containment is governed by agglomeration, de-agglomeration, and particle growth by steam condensation. The evolution of PSD is given the General Dynamic Equation (GDE) (Allelein *et al.*, 2009). The GDE is described in chapter 3 (Eq. 3.27). There are two commonly used approach to solve the GDE. They are the sectional model and the Method of Moments (MOM) (Lucci *et al.*, 2022). The sectional model splits a given PSD into finite sections, and solves a number concentration equation for each section. The sectional method is implemented in the MAEROS aerosol dynamics code. MAEROS is implemented as a sub-module in system codes such as COCOSYS and MELCOR (Allelein *et al.*, 2009). The Method of Moments(MOM) has multiple types based on the nature of PSD, e.g, Quadrature MOM, Gamma MOM, log-normal MOM.

In the present thesis, a computationally efficient CFD model is sought after. Though the sectional model is used in system codes to capture the particle growth due to steam condensation, they are not applicable to CFD simulations because of the computational cost which scales with the number of grid points. In a containment flow, the PSD follows a log-normal distribution (Allelein *et al.*, 2009), and hence the log-normal

MOM is applicable. The log-normal MOM approximates the GDE with one number concentration equation and hence computationally cheap (Lucci *et al.*, 2022). In the scope of the present thesis, both the sectional and the log-normal MOM are implemented, but the log-normal MOM is applied to technical scale simulations.

CHAPTER 3

CFD Modeling Approach

The primary aim of this thesis is to develop a CFD model to simulate the gas-aerosol transport prevailing in a nuclear reactor containment in the event of a severe accident. The preceding Ph.D. project developed an Euler-Lagrangian CFD model to analyze the impact of decay heat on containment flows (Kampili, 2022). But for application to technical scale simulations, the Euler-Lagrangian approach is computationally costly. This chapter discusses a computationally efficient CFD model based on the simplified Euler-Eulerian approach. The section is organized into two parts: First, the gas flow modeling is discussed, followed by the aerosol transport modeling.

3.1 GAS-FLOW MODELLING

In the recent years, at Forschungzentrum Jülich, the *containmentFOAM* CFD solver and supporting model libraries, based on OpenFOAM, are being developed, to model containment flows (Kelm *et al.*, 2019*a*; Kumar *et al.*, 2020). During a severe accident, e.g., a LOCA (Loss of coolant accident) with core damage, the flow prevailing in a nuclear-reactor containment comprises of a multi-component gas mixture (in particular N_2, O_2, H_2, and H_2O) and it is primarily in the turbulent mixed convection regime. The flow is incompressible from the perspective of its speed, i.e., $Ma < 0.3$, but the density varies due to temperature gradients and mass concentration gradients of the multi-component mixture. Thus, the Boussinesq approximation for buoyancy forces becomes untenable, and the ideal gas equation of state models the varying density. Conjugate heat transfer modeling addresses condensation on cold structures of the containment (steel and concrete walls). Furthermore, the *containmentFOAM* solver can handle radiative heat transfer between the structures and the humid atmosphere. Due to the containment size (Volume $\sim$ 50,000 - 70,000 m^3 for a typical pressurized water reactor and Volume $\sim$ 15,000 m^3 for a boiling water reactor), scale resolving approaches such as LES or DNS becomes computationally expensive; therefore, an unsteady RANS (uRANS) approach based on the k-ω-SST model by Menter and Esch (2001) is applied.

This section is organized into three parts: First, the equations governing the fluid flow are addressed. The second part discusses the different approaches for modeling wall condensation. Finally, the numerical methods and the order of solving the equations are elaborated.

3.1.1 Governing equations

3.1.1.1 Species mass conservation

For a system of N gas species with $S = \{1, 2, 3, ..., N\}$, the species mass conservation equation is defined in terms of the species mass fractions Y_k, $\forall k \in S$. Subscript v denotes the condensable species or vapor. The set of non-condensable gas species, identified by subscript nc, includes all the species except the vapor.

$$\frac{\partial (\rho Y_k)}{\partial t} + \nabla \cdot (\rho \vec{U} Y_k) = -\nabla \cdot J_k + S_{Y_k}, \tag{3.1}$$

where $\vec{J_k}$ is the diffusive mass flux and S_{Y_k} is volumetric source term ($= 0$ unless explicitly defined) of the kth specie. The diffusive mass flux $\vec{J_k}$ is described by Fick's law of diffusion

$$\vec{J_k} = -\rho D_{k,\text{eff}} \nabla Y_k - D_{k,T} \frac{\nabla T}{T}. \tag{3.2}$$

The first term on the RHS of Eq. (3.2) is the diffusive mass flux due to the concentration gradient. $D_{k,\text{eff}} = D_{k,m} + D_{k,t}$ is the effective diffusivity of the specie k in the multi-component gas medium with $D_{k,m}$ and $D_{k,t}$ being the molecular diffusivity and turbulent diffusivity respectively. In flow regimes, where turbulence dominates, it is common to assume the same molecular diffusivity for all the species. This approximation is suitable for gases of similar molecular weights. In containment applications, the molecular weights of the gases—H_2, H_2O, and N_2—are dissimilar, and they diffuse at different rates. Thus, in the present work, the *effective binary diffusivity approximation*, which handles the varying diffusion rates, is used to model the molecular diffusivity,

$$D_{k,m} = \frac{1 - X_k}{\sum_{\substack{j=1 \\ j \neq k}}^{N} X_j / D_{jk}}, \tag{3.3}$$

where X_j is the molar fraction of species 'j' and D_{jk} is the binary diffusivity of the species pair $j - k$. Turbulent diffusivity is defined as $D_t = \nu_t / Sc_t$, where ν_t is the eddy viscosity and $Sc_t = 0.9$ is the turbulent Schmidt number. The second term, on the RHS of Eq. (3.2), corresponds to mass diffusion due to temperature gradients i.e., thermophoresis or the Soret effect, where $D_{T,k}$ is the thermal diffusion coefficient of kth species. For the wall condensation phenomenon, the mass diffusion is primarily governed by the gas concentration gradient, whereas the temperature gradient has a negligible impact (Minkowycz and Sparrow (1966)). Consequently, the Soret effect is omitted in the present work.

3.1.1.2 Total mass conservation

Summing the N species mass conservation equations (Eq. (3.1)) gives the total mass conservation or continuity equation

$$\frac{\partial \rho}{\partial t} + \nabla \cdot \left(\rho \vec{U} \right) = S_{\mathrm{m}}, \tag{3.4}$$

where S_{m} is the volumetric source term in the continuity equation ($S_{\mathrm{m}} = 0$, unless specified). The continuity equation is solved along with $N - 1$ species mass conservation equations. The mass fraction of the N-th species (non-condensable species that is in abundance) is obtained by the mass fraction constraint, i.e., $\sum_{i=1}^{N} Y_k = 1$.

3.1.1.3 Momentum conservation equation

The momentum conservation equation that governs the flow velocity $\vec{U}$ is given by

$$\frac{\partial \left(\rho \vec{U} \right)}{\partial t} + \nabla \cdot \left(\rho \vec{U} \otimes \vec{U} \right) = -\nabla p + \nabla \cdot \tau + \rho \vec{g} + \vec{S}_{\mathrm{mom}}, \tag{3.5}$$

where τ is the viscous stress tensor, p is the pressure, $\vec{g}$ is the acceleration due to gravity, and $\vec{S}_{\mathrm{mom}}$ is the volumetric source term for the momentum equation ($\vec{S}_{\mathrm{mom}} = 0$, unless specified). The viscous stress tensor is defined as

$$\tau = \rho \left(\nu + \nu_t \right) \left[\nabla \vec{U} + (\nabla \vec{U})^T - \frac{2}{3} \delta \nabla \cdot \vec{U} \right], \tag{3.6}$$

where ν is the kinematic viscosity of the gas mixture, ν_t is the turbulent eddy viscosity and δ is the Kronecker delta. Turbulence model provides ν_t (Section 3.1.1.6).

3.1.1.4 Energy conservation equation

Energy conservation is treated with the total enthalpy formulation.

$$\begin{aligned} \frac{\partial (\rho h)}{\partial t} + \nabla \cdot (\rho \vec{U} h) + \frac{\partial (\rho K)}{\partial t} + \nabla \cdot (\rho \vec{U} K) = \\ \frac{\partial p}{\partial t} - \nabla \cdot \vec{q}'' + \nabla \cdot (\vec{U} \cdot \tau) + \vec{U} \cdot (\rho \vec{g}) + \vec{U} \cdot \vec{S}_{\mathrm{mom}} - \nabla \cdot \vec{q}''_{\mathrm{rad}} + S_{\mathrm{h}} \end{aligned} \tag{3.7}$$

The LHS corresponds to the material derivative of total enthalpy, given by $h_{\mathrm{tot}} = h + K$, with $K = |\vec{U}|^2/2$ being the mechanical energy (specific kinetic energy of the mean

flow). The terms in the RHS are described as follows: The first term ($\partial p/\partial t$) accounts for the enthalpy changes due to temporal pressure variations. The second term corresponds to the enthalpy transport from net heat flux due to conduction and mass diffusion ($\vec{\dot{q}}''$ described in Eq. (3.8)). The third term accounts for viscous dissipation; it is negligible for low speed flows, i.e., $Ma < 0.3$ and hence neglected. The fourth term and the fifth terms represent the work due to the momentum sources $\rho\vec{g}$ and $\vec{S}_{\text{mom}}$. The sixth term $-\nabla \cdot \vec{\dot{q}}''_{\text{rad}}$ is the volumetric source term due to radiation heat transfer. The seventh term is for any arbitrary volumetric enthalpy source term ($S_{\text{h}} = 0$, unless specified). The heat flux vector,

$$\vec{\dot{q}}'' = -\lambda_{\text{eff}} \nabla T + \sum_{k=1}^{N} \vec{J}_k h_k - \sum_{j=1}^{N} \sum_{k=1}^{N} \frac{p}{\rho^2} \frac{D_{T,j}}{Y_j} \frac{X_j X_k}{D_{jk}} \left(\frac{\vec{J}_k}{Y_k} - \frac{\vec{J}_j}{Y_j} \right), \tag{3.8}$$

consists of three contributions: 1) the conductive heat flux, 2) enthalpy transport due to diffusive mass flux, and 3) heat flux due to the Dufour effect. The Dufour effect is an inverse phenomenon of the Soret effect described in section 3.1.1.1, i.e., a heat flux arising due to mass concentration gradients. Minkowycz and Sparrow (1966) concluded that the Dufour effect has a negligible impact on wall condensation for a steam-air mixture—ergo, the heat flux contribution due to the Dufour effect is omitted in the present work. However, in the future, consideration has to be given to the Dufour and Soret effects in the presence of light gases, e.g., H_2, He. The diffusive heat flux follows Fourier's law of heat conduction. For improving the CFD solver's numerical stability, the diffusive heat flux term is formulated partly implicit by rewriting it in terms of static enthalpy h. From the preceding arguments and substituting for the diffusive mass flux (Eq. (3.2)), the heat flux vector becomes

$$\vec{\dot{q}}'' = -\rho\alpha_{\text{eff}} \nabla h + \sum_{k=1}^{N} \rho \left(\alpha_{\text{eff}} - D_{k,\text{eff}} \right) h_k \nabla Y_k, \tag{3.9}$$

where $\alpha_{\text{eff}} = \alpha + \alpha_t$ is the effective thermal diffusivity of the gas mixture. Here, α is the molecular or laminar thermal diffusivity of the mixture and $\alpha_t = \nu_t / Pr_t$ is the turbulent thermal diffusivity. In the present work, the turbulent Prandtl number is chosen to be the same value as turbulent Schmidt number, i.e., $Pr_t = Sc_t = 0.9$. Consequently, the turbulence contribution in the second term of heat flux vector (Eq. (3.9)) vanishes and only the laminar part remains. Only if Lewis number $Le_k = \alpha / D_{k,m} \sim 1$ holds for all species, the second term in the heat flux vector (Eq. (3.9)) becomes negligible. Therefore, the heat flux vector is used as in Eq. (3.9) without further simplifications.

3.1.1.5 Equation of state

The transport equations of mass, momentum and energy are closed by the equations of state for density and enthalpy. For containment flows, the gas mixture is considered to be an ideal gas. Consequently, density is defined as

$$\rho = \frac{pW}{R_u T}, \tag{3.10}$$

where $W = \left(\sum_{k=1}^{N} Y_k/W_k\right)^{-1}$ is the molar mass of the gas mixture with W_k being the molar mass of the kth species in $\mathrm{kg\,kmol^{-1}}$ and $R_u = 8314.5\,\mathrm{J\,kmol^{-1}\,K^{-1}}$ is the universal gas constant. With the ideal gas assumption, the static enthalpy for a gas species k is related to temperature by

$$h_k = h_{\text{ref},k} + \int_{T_{\text{ref}}}^{T} c_{p,k} dT, \tag{3.11}$$

where T_{ref} is the reference temperature, $h_{\text{ref},k}$ is the enthalpy of the kth at the reference temperature, and $c_{p,k}$ is the specific heat capacity at constant pressure for species k (temperature-dependent property). The value of $T_{\text{ref}} = 0\ K$ and $h_{\text{ref},k} = 0\ \mathrm{J\,kg^{-1}}$ is used for all the gas species including the condensing vapor. Since bulk condensation is ignored and only wall condensation is under consideration in the present work, the phase-change enthalpy of condensation is handled through the boundary conditions (described in section 3.1.2.1). From this, the static enthalpy of the mixture is related to the temperature as $\frac{dh}{dT} = c_p$; with this relation, the temperature field can be obtained from the static enthalpy using the Newton-Raphson method.

3.1.1.6 Turbulence quantities

Turbulence contribution arises in the species mass conservation, momentum conservation, and energy conservation equations through the turbulent mass diffusivity $D_{k,t}$, the eddy viscosity ν_t, and the turbulent thermal diffusivity α_t, respectively. The standard k-ω-SST model of Menter and Esch (2001), which solves transport equations for turbulent kinetic energy k[1]and eddy frequency ω, models turbulence. The model is selected because it can be integrated up to the wall with a low Reynolds number boundary condition (low-Re approach). The eddy viscosity ν_t is a function of k and ω. Further, D_t and α_t are evaluated from ν_t using relations discussed already.

[1] k used in section 3.1.1.6 identifies turbulent kinetic energy and not the species index k used in other sections

3.1.1.7 Temperature dependent mixture properties

In a low-Re approach, the molecular transport properties dominate the wall fluxes. Since strong temperature gradients exist in the vicinity of a condensing wall, temperature-dependent transport properties are important to obtain the correct mass, momentum, and energy fluxes. Individual species properties—molecular viscosity μ_k, thermal conductivity λ_k, and specific heat capacity at constant pressure $c_{p,k}$—are defined as polynomial functions of temperature. Temperature-dependent molecular diffusivity $D_{k,m}$ is specified by computing the binary diffusivity D_{jk} with the Fuller approach (Fuller *et al.*, 1966). Wilke (1950) model is used to define the gas mixture's viscosity and thermal conductivity. The mixture's specific heat capacity is obtained with a mass-weighted summation of individual species' specific heat capacity values.

3.1.2 Wall condensation modelling

The saturation pressure of vapour at the interface temperature T_i and the partial pressure of vapour in the wall-adjacent cell determines wall condensation. Wall condensation is enabled if $p_{v,\text{sat}} < p_{v,c}$. Saturation pressure is computed at the interface temperature using Antoine's equation (Antoine, 1888). For steam, saturation pressure is given as

$$p_{v,\text{sat}} = 133.28e^{\left(18.3036 - \frac{3816.44K}{T_i - 46.13K}\right)} \text{ [Pa]}. \tag{3.12}$$

The mass fraction of vapor at the interface corresponding to $p_{v,\text{sat}}$ is evaluated as follows:

1. Compute molar fraction of vapor using the Dalton's law of partial pressures, i.e., $X_{v,i} = p_{v,\text{sat}}/p_i$.
2. Calculate the effective molecular weight of the mixture of non-condensable species, i.e., $W_{nc,i} = \sum_{k \in nc} X_k^* W_k$. Since, the sum of the molar fractions of non-condensable gases is not equal to unity, a normalized molar fraction—$X_k^* = X_k / \sum_{j \in nc} X_j$—is used.
3. Find the effective molecular weight of the mixture of condensable and non-condensable gas species, i.e., $W_{\text{mix},i} = X_{v,i} W_v + (1 - X_{v,i})\, W_{nc,i}$.
4. Evaluate vapor mass fraction $Y_{v,i} = X_{v,i} W_v / W_{\text{mix},i}$.

If $p_{v,\text{sat}} \geq p_{v,c}$, to prevent re-evaporation of the vapor from the wall, a zero-flux or zero-gradient boundary condition is resembled by setting the vapor mass fraction at the interface equal to that of the wall adjacent cell. If the condensation criterion is satisfied,

vapor diffuses towards the cold wall (also the liquid-vapor interface). This motion also entrains the non-condensable gases; the liquid-vapor interface is impermeable to the non-condensable gases. In the vicinity of the interface, non-condensable gases will build-up. For both the condensing vapor and non-condensable gases, the mass flux normal to the interface—going out of the computational domain—has a convective and diffusive component. If $\vec{n}_i$ is the unit outward-facing normal to the interface, the mass flux for the condensable vapor is given by

$$\dot{m}''_{v,i} = \left(\rho_i \vec{U}_i Y_{v,i}\right) \cdot \vec{n}_i + \vec{J}_{v,i} \cdot \vec{n}_i. \tag{3.13}$$

Due to the impermeability condition, the mass flux of the non-condensable species is zero, i.e.,

$$\dot{m}''_{k,i} = \left(\rho_i \vec{U}_i Y_{k,i}\right) \cdot \vec{n}_i + \vec{J}_{k,i} \cdot \vec{n}_i = 0, \quad \forall k \in nc. \tag{3.14}$$

Equation (3.14) signifies that the convective flow of non-condensable gases towards the interface compensates the diffusive flux back into the bulk, due to the mass fraction of non-condensable species at the interface being more abundant than that of the near-wall cell. The mass fraction of each non-condensable gas species at the condensing interface is obtained by solving equation (3.14). The general formulation of mixture mass flux at the interface is

$$\dot{m}''_i = \rho_i \vec{U}_i \cdot \vec{n}_i = \dot{m}''_{v,i} + \sum_{k \in nc} \dot{m}''_{k,i}. \tag{3.15}$$

From equations ((3.13)) to ((3.15)), the condensation mass flux is

$$\dot{m}''_i = \dot{m}''_{v,i} = \frac{1}{1 - Y_{v,i}} \left(\vec{J}_{v,i} \cdot \vec{n}_i\right). \tag{3.16}$$

3.1.2.1 Interface temperature boundary condition

Based on a particular scenario, interface temperature may be modelled in one of the following ways.

1) Fixed temperature or Dirichlet BC: If the condensing wall can be considered an infinite reservoir of heat, the latent heat of condensation will have a negligible impact on the wall temperature; therefore, a fixed value boundary condition is sufficient.

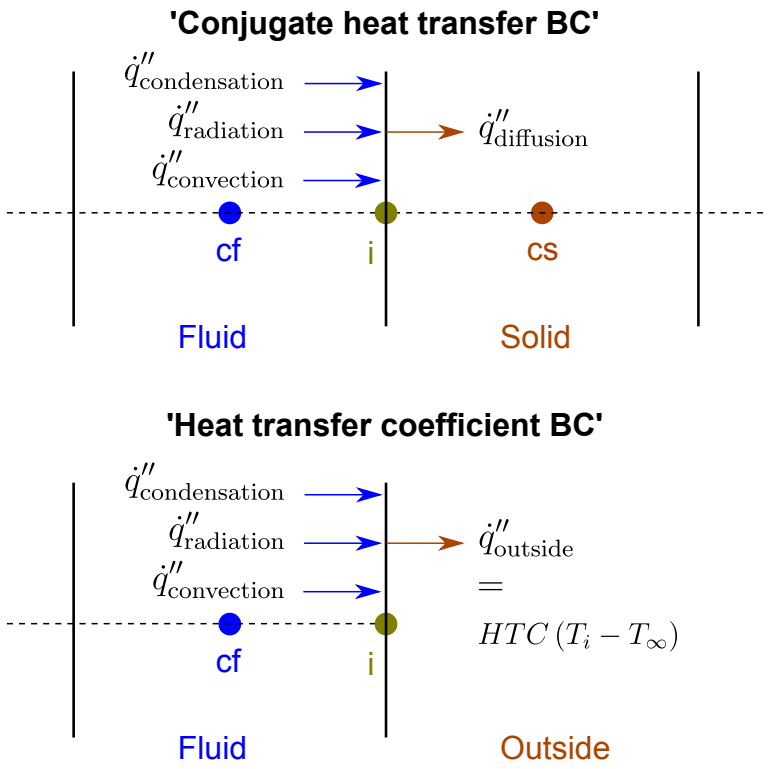

Figure 3.1: Temperature boundary conditions at the condensing interface 'i'—Conjugate heat transfer and Heat transfer coefficient—with heat flux due to convection, condensation and radiation.

2) Conjugate heat transfer BC: If the condensing wall is at the interface of a solid and a fluid region, an additional heat diffusion equation is solved to account for the heat transport in the solid region. Then, the interface temperature is evaluated by performing the heat balance as follows. The vapor condenses at the liquid-vapor interface by releasing the latent heat of condensation. The heat flux due to condensation is given by

$$\dot{q}''_{\text{condensation},i} = \dot{m}''_i h_{vL}, \tag{3.17}$$

where $h_{vL} = h_v - h_{l=L}$ is the latent enthalpy due to change of phase from vapor 'v' to liquid 'L' at the saturation pressure of vapor at the interface (Eq. (3.12)). The conjugate heat transfer boundary conditions is illustrated by means of one-dimensional control-volumes in Fig. 3.1. The total heat flux from the fluid control-volume towards the interface is equal to the net heat flux from the interface into the solid control-volume. The heat flux from the fluid towards the interface has contributions due to condensation, radiation, and convection, whereas in the solid domain, the heat flux is only due to

diffusion.

$$\dot{q}''_{\text{condensation},i} + \dot{q}''_{\text{radiation},i} + \lambda_{f,\text{eff}} \frac{T_{cf} - T_i}{\delta_{cf-i}} = \lambda_s \frac{T_i - T_{cs}}{\delta_{cs-i}}. \tag{3.18}$$

Here, $\lambda_{f,\text{eff}}$ is the effective thermal conductivity of the fluid at the interface accounting for laminar and turbulent heat flux, λ_s is the thermal conductivity of the solid, δ_{cf-i} is the distance of the cell-center 'cf' of the fluid control-volume from the interface i, and δ_{cs-i} is the distance of the cell-center 'cs' of the solid control-volume from the interface i. Temperature T_i is evaluated from Eq. (3.18) and applied as a boundary condition for the energy equations of the fluid and solid domain. The governing equations for the fluid and solid regions are solved in a segregated manner and iterated until the temperature and total heat flux values at the interface converge for the fluid and solid regions.

3) Heat transfer coefficient BC: If a cooling system controls the wall temperature, e.g., oil/water-cooled heat exchanger, or if the interface is in contact with quiescent air, such that the heat transfer is by natural convection, then the heat transfer coefficient (HTC) and ambient temperature (T_∞) boundary condition can be employed. The interface temperature T_i is obtained by performing the following heat balance analysis.

$$\dot{q}''_{\text{condensation},i} + \dot{q}''_{\text{radiation},i} + \lambda_{f,\text{eff}} \frac{T_{cf} - T_i}{\delta_{cf-i}} = HTC\,(T_i - T_\infty) \tag{3.19}$$

3.1.2.2 Wall condensation approaches

In the literature, two approaches for modeling wall condensation are commonly used: 1) Volumetric source terms in the near-wall cell (Bucci *et al.*, 2013; Dehbi *et al.*, 2013), 2) Face-flux at the condensing wall (Zschaeck *et al.*, 2014). The mathematical description of the models is presented below and their performance is compared in the next chapter.

Approach 1 - Volumetric source terms: In CFD codes, the use of a no-slip boundary condition defines a wall to be impermeable to mass flux. In this case, vapor condensation is implemented with volumetric source (sink) terms in the governing equations in the first cells adjacent to the walls (Fig. 3.2). The method has been previously used in the works of Bucci *et al.* (2013) and Dehbi *et al.* (2013) with consistent results. The source term in the total mass conservation equation (Eq. (3.4)) for a cell-volume V_c and interface area A_i is given by

$$S_\text{m} = -\frac{\dot{m}''_i A_i}{V_c}. \tag{3.20}$$

Only the vapor condenses, and therefore it seems reasonable to introduce a source

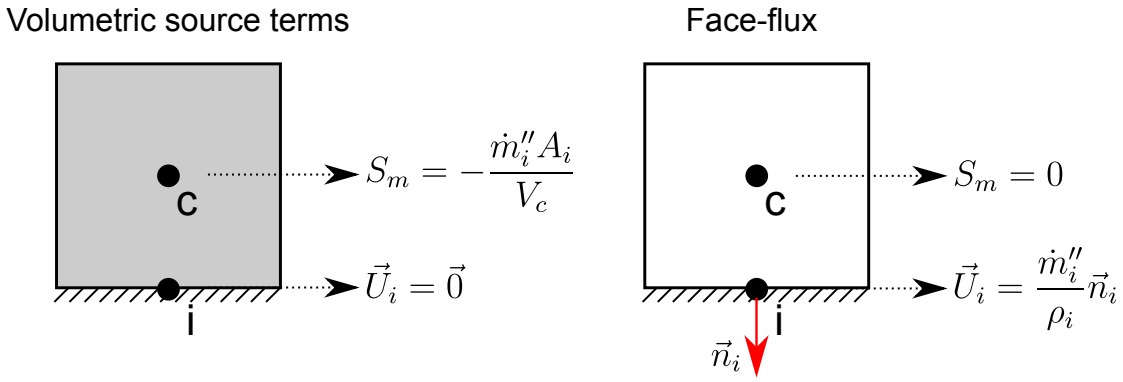

Figure 3.2: Illustration of *Volumetric source terms* (left) and *Face-flux* (right) models, with a two-dimensional control volume.

term only in the mass fraction equation of the vapor. But, for both the vapor and non-condensable species, concentration gradients at the wall result in non-zero diffusive mass flux. Consequently, the source terms of all species have to be corrected for this diffusive component and are of the form

$$S_j = -\frac{\dot{m}_i'' A_i}{V_c} Y_{j,i} = S_\mathrm{m} Y_{j,i}. \tag{3.21}$$

Along with the mass sink, the transported quantities have to be removed as well. The momentum source corresponding to the mass source term S_m is $\vec{S}_\mathrm{mom} = S_\mathrm{m}\vec{U}$. The respective source term in the energy equation is $\vec{S}_\mathrm{mom} \cdot \vec{U}$. For the energy equation, Bucci *et al.* (2013) and Dehbi *et al.* (2013) considered the latent enthalpy of condensation in the source term. But, in the present work, the formulation of enthalpy of the vapor does not contain the latent heat of condensation (section 3.1.1.5). Instead, the latent heat is treated through the temperature boundary condition. Thus, the source term in the energy equation is obtained by summing the contributions from individual species as

$$S_\mathrm{h} = \sum_{j=1}^{N} S_j h_j = S_\mathrm{m} h. \tag{3.22}$$

Similarly, the source terms for the turbulent kinetic energy equation and eddy frequency equation are $S_\mathrm{k} = S_\mathrm{m} k$ and $S_\omega = S_\mathrm{m}\omega$, respectively. The source terms of the species mass fractions, momentum, enthalpy and turbulence equations are of form $S_\phi = S_\mathrm{m}\phi$,

where ϕ is any arbitrary variable. Since, S_{m} is negative, the volumetric source terms are discretized as implicit terms, for better convergence.

Approach 2 - Face-flux: Instead of a "no-slip" boundary condition for velocity, mass flux is defined at the interface by specifying a suction velocity normal to the interface (Fig. 3.2).

$$\vec{U}_i = \frac{\dot{m}''_i}{\rho_i}\vec{n}_i \tag{3.23}$$

The above formulation also renders the velocity component tangential to the wall zero, i.e. $U_{x,i} = 0$. Through this boundary condition, the sink terms due to condensation, appear in the convective component $\nabla \cdot \left(\rho\vec{U}\phi\right)$ of all the governing equations, where $\phi \in \{1, Y_j, U, h, k, \text{and } \omega\}$.

3.1.2.3 Wall functions

In industrial applications, with large and complex geometries, it is impossible to fully resolve the turbulent boundary layer at all locations; instead, wall functions are employed to predict the wall fluxes. Though the wall condensation model developed in the current work, is for all the flow regimes—forced convection, natural convection, and mixed convection—, the discussion in this paper is limited to only forced convection flows for brevity's sake. Ideally, the wall functions should give mesh insensitive predictions, irrespective of whether the first grid point normal to the wall is in the viscous sublayer ($y^+ < 6$), or in the buffer layer ($5 < y^+ < 30$), or in the log-law region ($y^+ > 30$) of the forced convection turbulent boundary layer. Continuous wall functions achieve this purpose by blending the profiles of non-dimensional quantities—velocity, temperature, concentration, turbulent kinetic energy, and eddy frequency—in the viscous sublayer and the log-law region. In the absence of wall condensation, the turbulent viscosity at the wall ν_t is obtained from the Spalding (1961) continuous velocity profile (see Fig. 3.3). The Kader (1981) wall function gives the turbulent thermal diffusivity α_t and mass diffusivity D_t, based on the continuous profiles of temperature and species mass fractions. The eddy frequency ω value at the wall is specified through the blended profile described in Menter and Esch (2001). A zero-gradient boundary condition is imposed for the turbulent kinetic energy.

During condensation of vapor on a wall, the mass transport normal to the wall brings about the *suction effect*, which compresses the boundary layer, and hence the velocity profile deviates from the standard log-law profile (Favre *et al.*, 1966). The strength of

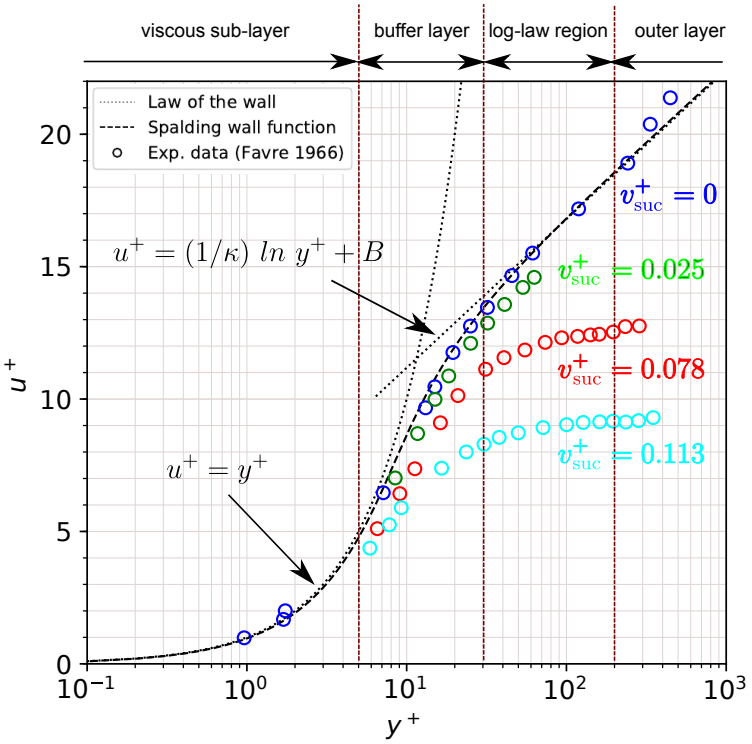

Figure 3.3: Streamwise velocity profiles for different suction velocities v^+_{suc}, compared with the law of the wall ($\kappa = 0.41$, $B = 5.5$) and Spalding continuous velocity profile, for turbulent, forced convection flows.

the condensation is quantified by the non-dimensional suction velocity $v^+_{\text{suc}} = \vec{U}_i \cdot \vec{n}_i / u_\tau$, where $u_\tau = \sqrt{(\tau_w/\rho)}$ is the friction velocity. Figure 3.3 shows the streamwise velocity (u^+) profiles for multiple suction velocities; it can be observed that the deviation from the log-law profile is more pronounced at larger suction velocities. Sucec (1999) and Lehmkuhl *et al.* (2016) describes corrected velocity profiles, as an alternative to the Spalding profiles, to handle this *suction effect*. However, for the experimental validation cases considered in the present work (section 4.4), the suction velocity is $v^+_{\text{suc}} < 0.02$ Consequently, the u^+ deviation from the log-law profile is expected to be insignificant. Hence, the continuous wall functions, without corrections for the *suction effect*, are deemed applicable. Future work aims at implementing a new consistent wall treatment for near-wall suction and buoyancy effects (Kelm *et al.*, 2019*b*). A summary of the boundary conditions at the condensation interface is given in Table 3.1.

Field	Boundary condition
Vapor mass fraction $Y_{v,i}$	Saturation condition at T_i
Non-condensable mass fractions $Y_{j,i}$	Impermeability condition (Eq. 3.14)
Velocity $\vec{U}_i$	No-slip condition for *Volumetric source terms* method / Suction velocity for *Face-flux* method (Eq. 3.23)
Temperature T_i	Fixed value / Conjugate heat transfer / Heat transfer coefficient
Turbulent viscosity $\nu_{t,i}$	Spalding profile (Spalding, 1961)
Turbulent thermal diffusivity $\alpha_{t,i}$	Kader wall function (Kader, 1981)
Turbulent mass diffusivity $D_{t,i}$	Kader wall function (Kader, 1981)
Turbulent kinetic energy k_i	Zero gradient
Eddy frequency ω_i	Menter's profile (Menter and Esch, 2001)

Table 3.1: Boundary conditions at the condensation interface.

3.1.3 Algorithm and solution method

The numerical discretization of the governing equations is second-order accurate in time and space. Figure 3.4 describes the order of solving the governing equations and how the wall condensation model interfaces with the transport equations. For every time-step, the transport equations are solved until the convergence criterion—initial residuals $< 10^{-5}$—is reached.

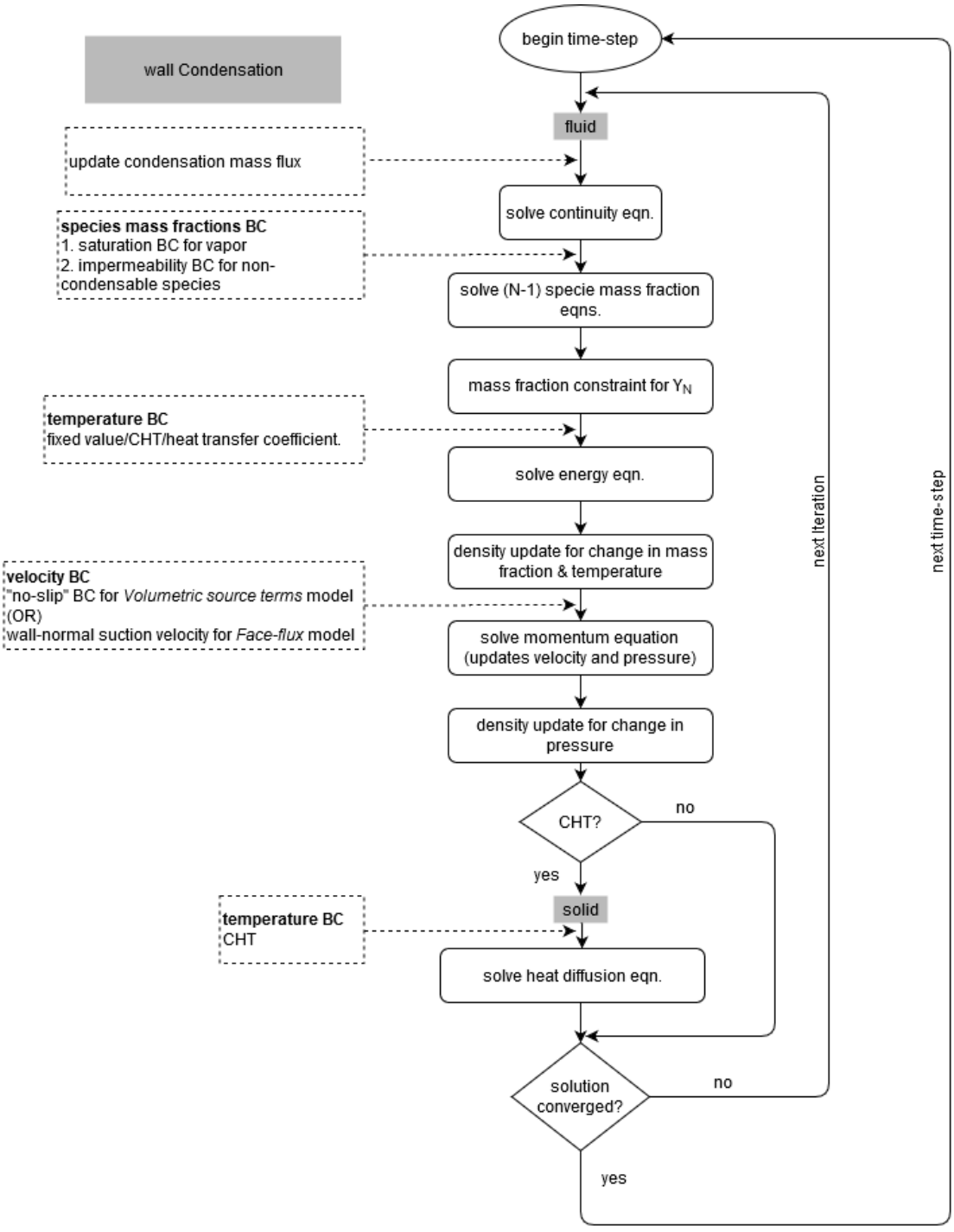

Figure 3.4: Wall condensation model interfacing with the PIMPLE algorithm for segregated solution of transport equations.

3.2 DISPERSED PHASE MODELING

In a nuclear reactor containment, the aerosol particle has a wide range of size distribution—0.1 $\mu\mathrm{m}$ to 10 $\mu\mathrm{m}$ (Allelein *et al.*, 2009). Also, due to agglomeration/de-agglomeration and steam condensation on aerosols, the particle size distribution (PSD) continually varies in time and space. Due to the different sources, e.g., degraded core and MCCI interactions, the aerosol is composed of multiple materials. The previous work, based on the Euler-Lagrangian approach, considered aerosols of monodisperse distribution (uniform size) and composition (Kampili, 2022). The current work develops a CFD model, which captures the evolving size distribution and multicomponent aerosol. For this purpose, the Eulerian mixture model described in Frederix (2016) is implemented in the framework of *containmentFoam* CFD solver as an add-on to the gas transport solver described in the previous section.

3.2.1 Multicomponent aerosol

The multi-component aerosol system is represented by an arbitrary number of species mass fractions, similar to the gas phase. In the current discussion, the terms aerosol, particle, and the droplet is used interchangeably. Since in the humid containment atmosphere, the aerosols reside primarily as water droplets (liquid), the dispersed particle phase is denoted by the superscript l. The gas phase is denoted by the superscript g. In the previous section (sec. 3.1), no such superscripts were used since the entire discussion was for the gas phase. Y_j denotes the mass fraction of j-th species in the gas phase, whereas Z_j represents the j-th species in the particle phase. N^g and N^l denote the total number of species in the gas and liquid phases, respectively. Y and Z represent the total mass fraction of the gas and particle phase, respectively.

$$Y + Z = 1 \tag{3.24}$$

The mixture rules used for computing the gas mixture properties (density, viscosity, thermal conductivity, specific heat capacity, and molecular diffusivity) in the previous section (sec. 3.1) still hold. The only change is that a normalized mass fraction Y_j/Y should be used instead of Y_j. For instance, the density of the gas phase is computed with Eq. 3.10, except that the molar mass of the gas mixture is computed with the normalized mass fractions.

The mixture density of the dispersed phase is computed from the species densities (ρ_j^l)

as,

$$\rho^l = \left[\sum_{j=1}^{N^l} \frac{Z_j/Z}{\rho_j^l} \right]^{-1} . \tag{3.25}$$

The species mass fraction Z_j is again normalized by the total phase mass fraction Z, similar to the treatment of the gas phase. The individual species densities in the dispersed phase is assumed to have a constant value and does not vary with temperature.

The density of the mixture of both the phases is given by

$$\rho = \left[\frac{Y}{\rho^g} + \frac{Z}{\rho^l} \right]^{-1} . \tag{3.26}$$

For simulations with both gas and aerosols, the mixture density given by the above equation is used in the governing equations of continuity, momentum, species mass fractions, and energy described in section 3.1.

3.2.2 Dispersed phase mass fraction equation

In addition to the governing equations for the gas phase described in the previous section3.1, the mass fraction equations for the dispersed phase species have to be defined. Frederix (2016) defined the number distribution $n(s, \mathbf{x}, t)$ as the number of particles per unit volume in the size range $[s, s + ds]$ at a location $\mathbf{x}$ (position vector) and time t. It must be noted that the particle size (s) used in this work denotes the particle's mass. Also, the containment aerosol particles are assumed to be spherical and do not have a shape factor. This assumption is valid since the particles become droplets by absorbing steam in the humid containment atmosphere (Allelein *et al.*, 2009). The 'General Dynamic Equation' (GDE) gives the evolution of particle size distribution.

$$\frac{\partial n(s)}{\partial t} + \nabla \cdot \left(\vec{U} n(s) \right) + \nabla \cdot \left(\mathbf{u}^l(s) n(s) \right) = \nabla \cdot \left[\left(\mathbb{D}^l(s) + \frac{\nu_t}{Sc_t} \right) \nabla n(s) \right] + J(s) \tag{3.27}$$

In this equation, the second term on the LHS accounts for the convection of the particle by the gas flow. The third term on the LHS represents the particle transport due to the particle's relative velocity (drift velocity) with the gas phase. The drift velocity of particles is significant in containment flows because of the particle inertia, i.e., the density of aerosol materials is greater than 1000 $\mathrm{kg\,m^{-3}}$. The first term on the RHS of Eq. 3.27, denotes the diffusion of particles due to Brownian motion and turbulence. The last term on the RHS accounts for the source term due to particle growth due to

steam condensation.

The first moment of the number size distribution gives the total mass of the dispersed phase per unit volume at a given location and time (x, t).

$$\rho Z = \int_0^\infty s\, n(s) ds \tag{3.28}$$

Applying this relation, the mass fraction equation of the dispersed phase can be obtained as,

$$\frac{\partial\left(\rho Z_j\right)}{\partial t} + \nabla \cdot \left(\rho \vec{U} Z_j\right) + \nabla \cdot \left(Z^{-1}\mathbf{f} Z_j\right) = \nabla \cdot \left[\frac{\nu_t}{Sc_t}\nabla Z\right] + S_{Z_j} \tag{3.29}$$

where $\mathbf{f}$, now not only accounts for drift flux ($\mathbf{f}^{\text{drift}}$) but also accounts for the mass flux due to Brownian diffusion ($\mathbf{f}^{\text{diff}}$).

$$\begin{aligned} \mathbf{f} &= \mathbf{f}^{\text{drift}} - \mathbf{f}^{\text{diff}} \\ \mathbf{f}^{\text{drift}} &= \int_0^\infty s\ \mathbf{u}^l(s)\ n(s, \mathbf{x}, t) ds \\ \mathbf{f}^{\text{diff}} &= \int_0^\infty s\ \mathbb{D}^l(s)\ \nabla n(s, \mathbf{x}, t) ds \end{aligned} \tag{3.30}$$

The drift velocity $\mathbf{u}^l(s)$ for a particle of size 's' is described in section 3.2.2.1. Brownian diffusion is dominant for particles in the sub-micron range and is given by the Stokes-Einstein equation.

$$\mathbb{D}^l(s) = \frac{k_B\ T\ C_c}{3\pi\ \mu\ d} \tag{3.31}$$

where, k_B is Boltzmann constant, T is Temperature, C_c is Cunningham correction factor, μ is mixture viscosity, and d is droplet diameter. C_c is defined as

$$C_c = 1 + \frac{\lambda}{d}\left(2.34 + 1.05\ \exp\left[-0.39\frac{d}{\lambda}\right]\right) \tag{3.32}$$

3.2.2.1 Drift velocity

The drift velocity is computed from the particle force balance equation, with the consideration of drag force, gravitational force (also buoyancy force), thermophoretic force, and diffusiophoretic force. The Basset history force and virtual mass forces are omitted since the ratio of particle density to the gas phase density is really high ($>> 1$).

Considering a particle of mass s and diamter d, the force balance can be written as

$$s\frac{d\mathbf{v^l}}{dt} = \vec{F_{\text{drag}}} + \vec{F_G} + \vec{F_T} + \vec{F_D} \tag{3.33}$$

Drag force: Drag force is modelled with the simplified Stokes-drag law along with Cunningham slip correction factor for sub-micron particles (Frederix *et al.*, 2017).

$$\vec{F}_{\text{drag}} = -\frac{1}{2}\rho^g A_p C_D |\mathbf{u^l}|\mathbf{u^l}, \tag{3.34}$$

with drag coefficient C_D given by

$$C_D = \frac{1}{C_C}\frac{24}{Re_p}. \tag{3.35}$$

Particle Reynolds number Re_p is given by

$$Re_p = \frac{\rho^g \mathbf{u^l} d}{\mu}, \tag{3.36}$$

and the Cunnigham slip correction is given by

$$C_c = 1 + \text{Kn}\left(1.257 + 0.4\text{exp}\left(\frac{-1.1}{\text{Kn}}\right)\right) \tag{3.37}$$

Thermophoretic force: Particles suspended in the gas phase experience an additional acceleration due to the prevailing temperature gradient. This phenomenon is known as thermophoresis. Kampili (2022) showed that the thermophoresis is dominant in sub-micron particles and hence relevant for containment application. The formulation for thermophoretic force used in the present work is as described by Talbot *et al.* (1980).

$$\vec{F_T}(d) = -\frac{6\pi d\mu^2 C_s\left(K + C_t\text{Kn}\right)}{\rho^g\left(1 + 3C_m\text{Kn}\right)\left(1 + 2K + 2C_t\text{Kn}\right)}\frac{\nabla T}{T}. \tag{3.38}$$

Here, K is the ratio of thermal conductivity of the gas and dispersed phases,

$$K = \frac{\lambda^g}{\lambda^l}. \tag{3.39}$$

The gas phase's thermal conductivity used in this relation is not identical to the thermal conductivity used in the energy equation. Here, the thermal conductivity is based on the

transitional energy only and is given by,

$$\lambda^g = \frac{15\mu R_u}{4\bar{W}^g}, \tag{3.40}$$

where, R_u is the universal gas constant and W^g is the molar mass of the gas phase. The constants used in the relation are $C_s = 1.17$, $C_t = 2.18$, and $C_m = 1.14$.

Diffusiophoretic force: Due to condensation on the cold structures of a containment, appreciable gas concentration gradients exist in its proximity, giving rise to diffusion of gas molecules. An aerosol particle present in this region, will experience phoretic forces due to the motion of gas molecules. Due to the difference in molecular weights of the gas molecules, there will be a net force on the aerosol particle called as "Diffusiophoretic force." The formulation for diffusiophoretic force is described for an "air-water vapor" binary gas system is described in Camuffo (2014). For containment application, air is replaced with a mixture of non-condensable gas species (in particular N_2, O_2, and light-gas H_2). If 'nc' represents the mixture of non-condensables, the diffusiophoretic force on an aerosol particle is given by,

$$\vec{F_D}(d) = -\frac{\sigma_{v-nc} D_v}{\tau C_c} \nabla X_v, \tag{3.41}$$

where, σ_{v-nc} is the diffusion slip factor,

$$\sigma_{v-nc} = \frac{W_v - W_{nc}}{(X_{nc} W_{nc} + X_v W_v) - (X_v + X_{nc})\sqrt{X_v X_{nc}}}. \tag{3.42}$$

The deposition of aerosol particles on condensing walls due to Stefan flow is not considered in the above formulation. Instead, Stefan flow is accounted for in the mixture velocity $\vec{U}$.

Local equilibrium assumption: The particle velocity $\mathbf{v}^{\mathbf{l}}$ and the drift velocity $\mathbf{u}^{\mathbf{l}}$ are related by

$$\mathbf{v}^{\mathbf{l}} = \vec{U} + \mathbf{u}^{\mathbf{l}}. \tag{3.43}$$

Rewriting Eq. 3.33, in terms of drift-velocity,

$$s\left(\frac{d\vec{U}}{dt} + \frac{d\mathbf{u}^{\mathbf{l}}}{dt}\right) = \vec{F}_{\text{drag}} + \vec{F_G} + \vec{F_T} + \vec{F_D} \tag{3.44}$$

In the LHS, the rate of change of the gas phase velocity $\vec{U}$ is the acceleration $\vec{a}$. The second term is the rate of change of drift velocity. Manninen *et al.* (1996) stated that the rate of change of drift velocity vanishes for cases where the dispersed phase reaches the terminal velocity instantly. This approach is called as "Local equilibrium approach." Scoping analysis for the particle sizes prevailing in the containment revealed that the approach is valid. On simplifying Eq. 3.44, the drift velocity is obtained.

$$\mathbf{u^l} = \left(\vec{G} + \frac{\vec{F_T}}{s} + \frac{\vec{F_D}}{s} - \vec{a} \right) \tau C_c, \tag{3.45}$$

where, $\vec{G}$ is

$$\vec{G} = \frac{\left(\rho^l - \rho^g\right)}{\rho^l} \vec{g}, \tag{3.46}$$

and τ is the particle relaxation time.

$$\tau = \frac{\rho^l d^2}{18\mu}. \tag{3.47}$$

3.2.3 Evolution of particle size distribution

In the current work, the particle size distribution changes due to the hygroscopic growth in humid containment atmosphere. Two approaches are used in the current work to compute the PSD evolution: *Sectional method* and the *Log-normal* method.

3.2.3.1 Sectional method

The sectional method divides the size domain into P arbitrarily sized adjoining interval (Lucci *et al.*, 2022). The i-th section (with $i = 1, 2, 3, .., P$) covers part of the size domain limited by $y_i \leq s < y_{i+1}$, with y_i being the position of the interface between $(i-1)$th and ith sections. If $N_i(\mathbf{x}, t)$ is the total number of droplets per unit volume in the i-th size section, then

$$N_i(\mathbf{x}, t) = \int_{y_i}^{y_{i+1}} n(s, \mathbf{x}, t) ds \qquad [m^{-3}]. \tag{3.48}$$

The general dynamic equation 3.27 is rewritten for a specific section as,

$$\frac{\partial \rho M_i}{\partial t} + \nabla \cdot \left(\rho \vec{U} M_i \right) + \nabla \cdot \left(\rho \mathbf{u}_i^l M_i \right) = \nabla \cdot \left[\mathbb{D}_i^l \, \nabla (\rho M_i) \right] + \mathcal{J}_{M_i}. \tag{3.49}$$

Here $M_i = N_i/\rho$. The drift velocity and Brownian diffusivity are computed for the particle size in each section. The turbulent diffusion is not shown in the above equation for conciseness, but it is considered in the simulations.

3.2.3.2 Log-Normal model

The *Log-Normal* model is based on the Method of Moments (MOM) and assumes the particle size distribution to be "log-normal" with a fixed geometric size distribution (GSD).

$$\frac{\partial \rho M}{\partial t} + \nabla \cdot (\rho \mathbf{U} M) + \nabla \cdot \left(\rho \mathbf{u}^l M\right) = \nabla \cdot \left[\mathbb{D}^l \, \nabla(\rho M)\right] + \mathcal{J}_M. \tag{3.50}$$

The drift velocity and Brownian diffusivity are computed based on the count mean diameter of the log-normal distribution. The *Log-Normal* model is computationally efficient, since it requires solving only one transport equation for the particle number concentration. The *Sectional Model* is computationally costly, but accurate.

3.2.3.3 Hygroscopic growth

Aerosol particles released into the containment of a nuclear reactor in the event of a core melt accident include both hygroscopic (e.g., CsI and CsOH) and non-hygroscopic materials (e.g., Ag, SnO2). Hygroscopic materials absorb water and grow in size in humid containment atmosphere. Steam condensation on aerosol particles have to be accounted for with source terms in the dispersed phase mass fraction equation for water species. A corresponding sink term has to be applied for the vapor mass fraction equation in the gas phase. Also, source terms have to be applied in the GDE equations of the *Sectional* and *Log-Normal* methods (Lucci *et al.*, 2022).

Asgari *et al.* (2021) describes the formulation for condensation rate (or evaporation rate). The rate of condensation (or evaporation) on a single particle is primarily dependent on the difference between the vapor partial pressure on the particle surface ($p_v, surf$) and in the gas phase (p_v). The condensation rate described in Newbold and Amundson (1973) and further successfully verified by Jokiniemi (1990) and Asgari *et al.* (2021) is used.

$$I_v = -\frac{2\pi\beta D_v^g \rho_v^g f(\xi_v)}{p} \left(e^{\xi_v} p_v - p_{v,\text{surf}}\right), \tag{3.51}$$

where β is the Knudsen or Fuchs' correction factor to account for the non-continuum effects arising in micron and sub-micron particle sizes, given by

$$\beta = \frac{1 + Kn}{1 + 1.71Kn + 1.3325Kn^2}, \tag{3.52}$$

where Kn is the Knudsen number. D_v^g is the effective molecular diffusivity of vapor. ρ_v^g is the vapor density based on ideal gas equation of state. The function $f(\xi_v)$ is to make the formulation of condensation rate applicable for a scenario where there are multiple phase changeable species. For an arbitrary species j,

$$f(\xi_v) = \frac{\xi_v}{1 - e^{\xi_v}}, \tag{3.53}$$

where

$$\xi_v = \ log \left(\frac{p - p_{v,\text{surf}}}{p - p_v} \right) \tag{3.54}$$

$$p_{v,surf} = A_w \text{Ke} p_{v,sat} \tag{3.55}$$

$p_{v,sat}$ is the saturation water vapor pressure at the temperature on the droplet surface. Since we assume thermal equilibrium between the gas and the particle phase, $p_{v,sat}$ is evaluated at the common temperature T using the Eq. 3.12. The Kelvin effect, dominant in sub-micron particles is considered with the coefficient "Ke" (Jokiniemi, 1990).

Water activity: The factor A_w is the chemical activity of water or hygroscopicity or simply water activity, is the tendency of a particle to absorb moisture from the surrounding atmosphere. $A_w = 1$ for non-hygroscopic materials, e.g., silver metal, and $A_w < 1$ for hygroscopic materials, e.g., NaOH, CsOH, CsI, etc.

The aerosol droplets can be treated as solutions of the material in water. In a nuclear reactor containment, the aerosol particle is composed of multiple components, e.g., CsI, CsOH, SnO_2, etc. Therefore, the water activity formulation should be defined for a multicomponent system. Jokiniemi (1990) uses the modified Raoult's law to compute the water activity,

$$A_w = \frac{1}{1 + \sum\limits_{j \neq H_2O} Q_j W_{H_2O}\, m_j}, \tag{3.56}$$

where Q_j is the van't Hoff factor of the species 'j', m_j is the molality of the soluble species 'j' in water. Molality is limited by the maximum solubility of a particular

substance in water.

$$m_j = \min\left[\frac{Z_j}{W_j Z_{H_2O}}, \frac{\text{solubility}}{W_j \rho^l_{H_2O}}\right] \tag{3.57}$$

3.2.4 Decay heat modeling

Due to the low volume fraction of the aerosol particles in containment flows ($\sim 10^{-5}$), no separate energy equation is considered for the particle phase, and thermal equilibrium is assumed between the particles and the gas phase. Kampili (2022) showed that the gas phase instantaneously absorbs the decay heat of aerosol particles and the temperature transients of the particle are short compared to the simulation time step used in containment applications. Therefore, the fission product decay heat—due to aerosols and noble gases— is absorbed entirely in the gas phase. They are modeled through the source term S_h in the energy conservation equation (Eq. 3.7). As an example, if CsI aerosol particles with a decay heat (DH) of 111.57 $\mathrm{kW\,kg^{-1}}$ will have a source term S_h in the energy equation is given by

$$S_\mathrm{h} = (\rho Z_\mathrm{CsI})\,\mathrm{DH}. \tag{3.58}$$

If multiple aerosol or noble gas components carry decay heat, then the source term is obtained by the sum of individual contributions.

3.3 SUMMARY

This chapter discusses the CFD model to simulate gas-aerosol transport in a containment atmosphere. The gas phase model describes the CFD models to simulate the turbulent, buoyancy-driven, multicomponent gas transport in a containment with conjugate heat transfer, radiation heat transfer, and wall condensation effects. Subsequently, the Eulerian aerosol transport is discussed with regards to the particle inertia (drift flux), the evolution of particle size distribution due to hygroscopic growth, and finally, the decay heat effect of aerosol particles (and noble gases). The linking between the gas phase and aerosol phase models is described. In the next chapter 4, the models depicted here are systematically validated against small-scale and technical scale experiments.

CHAPTER 4

Model Validation

4.1 VALIDATION STRATEGY

The phenomenology in a nuclear reactor containment during a severe accident is a multiphysics problem. The main phenomena are the multicomponent gas transport, turbulent flow in the free and mixed convection regime, wall and bulk condensation of steam, radiation heat transport, and conjugate heat transfer with the containment structures. In addition, nuclear aerosol particles released into the containment may influence the existing flow field. The primary objective of this thesis is to investigate the significance of the aerosol particle's decay heat on the gas transport and mixing processes. For the CFD model to be applicable for predictions, its validity must be proven against suitable experiments covering the different interacting phenomena.

Due to the size of a nuclear reactor containment (PWR dry containment volume $\sim$ 50,000-70,000 m^3, L $\sim$ 50 m), model validations against experiments done on small-scale test facilities are insufficient. Nevertheless, a small-scale experiment's simple and reduced computational domain facilitates comprehensive parametric studies necessary for model assessment. For this purpose, the CFD model is validated first against small-scale experiments—DHSC (L $\sim$ 0.75 m) and SETCOM (0.44 m x 0.44 m x 6 m)—followed by the technical scale experiments conducted in the THAI facility (Volume $\sim$ 60 m^3, L $\sim$ 9.2 m). The validation matrix (Fig. 4.1) shows the different experiments and the physics covered.

The experiment in the "**D**ifferentially **H**eated **S**quare **C**avity" (DHSC) investigates a two-dimensional, mildly turbulent (Ra $\sim 10^9$), natural circulation flow of dry-air (Ampofo and Karayiannis, 2003). The CFD solver's time-step sensitivity and the convergence criterion's effect on the simulation results are analyzed in this case. The findings are applied to further simulations in the present work. Since dry air is transparent to radiation, the influence of surface-to-surface radiation heat transfer on the flow field is studied with the fvDOM model.

The wall condensation model is to be validated as the next logical step. But before that, the two wall condensation models discussed in the previous chapter (*Volumetric source terms* and *Face-flux*) are compared to identify the computationally efficient and

Phenomenon:	DHSC	SETCOM	THAI-TH21	THAI-TH22	THAI-TH24	AHMED
Buoyancy	X		X	X	X	
Turbulence	X	X	X	X	X	
Multi-species gas		X	X	X	X	
Conjugate heat transfer			X	X	X	
Radiation heat transfer	X		X	X	X	
Wall condensation		X		X	X	
Aerosol transport						X
Hygroscopic growth						X

Figure 4.1: Validation matrix: Experiments and the physics covered.

accurate approach. For this purpose, a two-dimensional, turbulent channel flow case in the forced convection regime is employed.

In the "**S**eparate **E**ffect **T**ests for **CO**ndensation **M**odeling" (SETCOM) test facility, a wide range of steam-air flow in the forced convection and mixed convection regimes is studied to generate experimental data on wall condensation (Kelm *et al.*, 2019*b*). The CFD model is validated against SETCOM experiments in the forced convection regime. Apart from the primary phenomenon of wall condensation, the adaptability of the CFD model to give accurate results on coarser grids with wall functions is also studied. This ability is crucial for realizing a computationally efficient CFD code for containment applications.

After the validations against the small-scale experiments, the CFD model is validated against the experiments conducted in the technical scale THAI facility. Three THAI experiments in the natural convection regime with increasing order of complexity are taken up for analysis. Turbulence, buoyancy-driven flow, multicomponent gas diffusion, surface-to-surface and gas radiation heat transfer, wall condensation, and conjugate heat transfer are covered.

After validating the gas flow modeling part of the CFD model, the aerosol transport part is validated in two steps. In the first step, the hygroscopic growth model is validated by comparing the equilibrium diameter of different Nuclear aerosol materials at different relative humidities. Subsequently, the gravitational settling model is evaluated against the experiments in the AHMED facility (Volume = $1.81\ \mathrm{m}^3$). The depletion behavior of hygroscopic particles such as NaOH, CsOH, and CsI and non-hygroscopic (Ag) aerosols at different relative humidities are studied. The models for other phenomena like thermophoresis and diffusiophoresis of aerosol particles are thoroughly verified during implementation, and their discussion here is omitted for brevity.

4.1.1 Baseline CFD model

The default settings used in the CFD simulations performed in the present thesis are listed here. Turbulence modeling is done with the standard k-ω-SST model by (Menter and Esch, 2001). The SGDH model accounts for the turbulence production and dissipation source terms due to buoyancy (Chung W. and Devaud C. B., 2008). The temperature-dependent material properties are specified for the gas mixture, as discussed in section 3.1.1.7. The segregated system of governing equations is solved with the PIMPLE algorithm discussed in section 3.1.3. The PIMPLE iterations are performed for a time step until a residual of 10^{-5} is achieved for each equation. The numerical schemes mostly correspond to the baseline model settings, summarized in (Kelm *et al.*, 2019*a*). Second-order advection schemes are employed except for turbulent quantities. The advection term for the turbulence quantities is discretized with the first-order upwind scheme for stability. Furthermore, the laplacian term and the surface normal gradients scheme contain a limiter for the explicit source term of the non-orthogonal correction. Discretization in time is conducted with a second-order Crank-Nicholson scheme, which is stabilized by blending with a 10% Euler time marching scheme.

4.2 DIFFERENTIALLY HEATED SQUARE CAVITY (DHSC)

4.2.1 Experiment

The 2D natural circulation flow of dry-air in a square cavity (side H = 0.75 m) with low-level turbulence is chosen for validation as an initial step (Ampofo and Karayiannis, 2003). The hot wall and cold wall of the cavity are maintained at temperatures of 50 °C and 10 °C, giving a Rayleigh number Ra = 1.58×10^9. The top and bottom walls were insulated from the ambient conditions by layers of steel, wood, and polystyrene. The depth of the cavity in the z-direction is kept at 1.5 m (aspect ratio = 2) to ensure a 2D flow in the mid-plane of the cavity. The experiment provides high spatial resolution data on velocity profiles, temperature profiles, and turbulence statistics.

4.2.2 CFD setup

Since the flow prevailing in the experiment was ensured to be a two-dimensional, a two-dimensional grid is employed to reduce computational cost. For simplicity, the insulation solid materials—steel, wood, and polystyrene—used in the experiment are not considered in the CFD model. Instead, the top and bottom walls of the cavity are given an adiabatic boundary condition and only the fluid domain is considered. with the boundary conditions, as shown in Fig. 4.2. The grids were completely made of hexahedral cells with finer mesh resolution near the walls and stretching towards the core of the cavity with coarser cells. Such an arrangement is necessary to capture the near-wall gradients of velocity and temperature accurately.

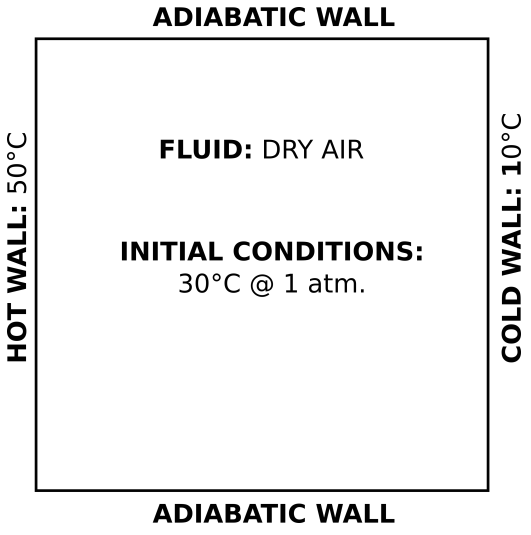

Figure 4.2: CFD Model - Differentially Heated Square Cavity

4.2.3 Discussion of results

Firstly, grid dependence was studied with the "average convective wall heat flux" as the parameter. As a second step, the time-step dependency and impact of convergence criterion on the results are discussed. Simulations with and without radiations were performed to understand the influence of radiation on the wall heat transfer rates and temperature distribution in the atmosphere of the cavity. Finally, the CFD model is validated against the experimental data by comparing the simulation results of velocity, temperature, and turbulence kinetic energy against experimental data. All the results discussed below are time-averaged, unless stated otherwise. The time-averaging is performed once a quasi-steady state—constant volume-averaged temperature and pressure—is reached.

4.2.3.1 Near-wall treatment

For forced convection flows, the near-wall region can be modelled in either one of the following two ways. The first approach is to fully resolve the boundary layer close to the wall ($y^+ \sim 1$) and not using wall functions. The second approach is to place the first grid point outside the viscous sub-layer ($y+ > 6$) and using the standard wall functions as described in Fig. 4.3. The first approach, though accurate, is practically impossible in some cases, as it increases the number of grid points and hence makes the computational cost prohibitively expensive. The second approach of using the law of the wall relaxes the grid resolution requirement in the near-wall region and hence is the preferred choice in industrial applications. The major problem is that the standard wall functions are calibrated for forced convection flows. The applicability of standard wall functions for natural convection flows was evaluated by performing simulations with meshes of different near-wall grid resolutions. No wall functions were used for simulations with meshes that have sufficient near-wall resolution ($y^+ < 1$ and $y^+ \sim 2$). Simulations on two other meshes with the first grid point outside the viscous sub-layer ($y^+ \sim 7$ and $y^+ \sim 10$), were carried out with the standard law of the wall treatment.

The non-dimensional wall heat flux (local Nusselt number) is plotted for the different simulations against the experimental data in Fig. 4.4. The local Nusselt number is defined as

$$Nu_{local} = -\frac{L}{\Delta T}\frac{\partial T}{\partial n}\Big|_{wall}. \tag{4.1}$$

The local Nusselt number is under-predicted for simulations on grids where the standard

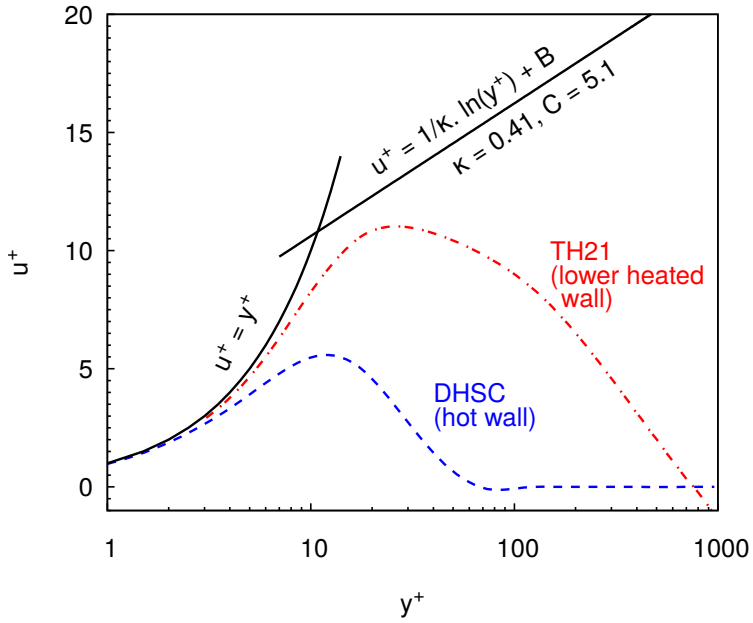

Figure 4.3: Comparison of natural-convection boundary layer profile of DHSC and THAI-TH21 (at heated walls) with the law of the wall typically used for forced convection flows.

wall functions were employed. The plot of non-dimensional streamwise velocity u^+ versus the non-dimensional distance from the wall y^+ for the differentially heated cavity case and the THAI-TH21 case also clearly demonstrate that the profiles deviate from the standard wall functions for $y^+ > 2$ (Fig. 4.3). It is conclusive that the near-wall region has to be completely resolved for natural convection flows ($y^+ < 2$), and the standard wall functions are not applicable.

4.2.3.2 Grid sensitivity

From the preceding section on the near-wall treatment, it is clear that the results are grid-dependent if the first grid point adjacent to a wall is outside the viscous sub-layer. Therefore, it becomes meaningless to perform grid sensitivity analysis with meshes that have $y+ > 2$. Hence, grid independence studies are carried out by keeping the near-wall resolution to $y^+ < 2$ and limiting the grid refinement to only the core of the cavity. The standard "Grid convergence index" (GCI) method was employed (ASME, 2008). The "average convective wall heat flux" on the hot wall (variable ϕ) of the cavity is the parameter chosen. Three successively refined grids of cells 400×400 (grid 1), 200×200 (grid 2), 100×100 (grid 3) were considered. Monotonic grid convergence was achieved, and the results are tabulated in Table 4.1. Mesh with a resolution 200×200 is used for

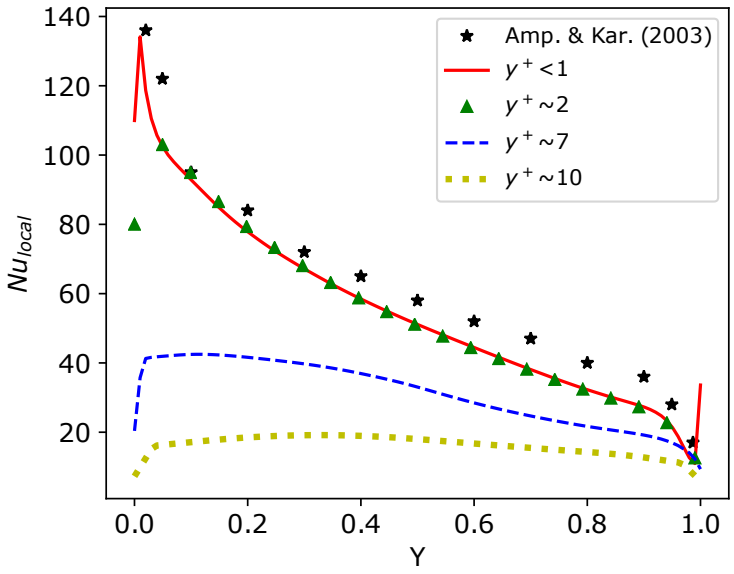

Figure 4.4: Comparison of local Nusselt number on the hot wall between experimental data and simulation results with different near-wall grid resolutions

further simulations.

4.2.3.3 Time-step size sensitivity

The sensitivity of the results to the time-step size is analyzed based on the transients of one local variable and a global variable, as shown in Fig. 4.5. Instabilities in the flow were visible near the corners of the cavity and hence the vertical velocity at a point located in the top left corner of the domain is chosen as the local parameter. The total heat transfer rate from the hot wall into the fluid is selected as the global parameter. The transients of both variables are monitored for a physical time of 10 s. It is clear from the results that the solution is time-independent if the maximum Courant number is less than 4. For the time-step size $dt = 0.08s$, the maximum Courant number is around 8, and the solution deviates from the results of simulations with smaller time-steps. Wiggles in the transients of the total heat transfer rate from the hot wall indicate solution instability. Hence, all the simulations reported in the present work are carried out with time-step values having maximum Courant number less than 4.

4.2.3.4 Convergence criterion

The solver used in the present work is a segregated solver, which means that the equations of continuity, momentum, energy, turbulence quantities, and ideal gas equation of state are solved separately in an iterative manner until the different fields

Number of grid points: N_1, N_2, N_3	160000,40000,10000
Domain area : $A(m^2)$	0.5625
Average elemental length: h_1, h_2, h_3	0.001875,0.00375,0.0075
yPlus values: y_1, y_2, y_3	0.58,1.13,2.21
Ratio of grid size: r_{21}	2
Ratio of grid size: r_{32}	2
ϕ_1	80.0191
ϕ_2	80.7335
ϕ_3	83.7364
Apparent order of convergence: p	2.0714
Richardson extrapolate: ϕ_{ext}^{21}	79.7960
Approximate relative error: e_a^{21}	0.89%
Extrapolated relative error: e_{ext}^{21}	0.3%
Coarse grid convergence index: GCI_{coarse}^{32}	1%
Fine grid convergence index: GCI_{fine}^{21}	0.3%

Table 4.1: Grid convergence study for the DHSC case using the average convective wall heat flux at the hot wall as the parameter ϕ.

converge for every time-step. Then the solution is advanced to the next time-step. The convergence is monitored by computing the residuals of individual equations. Three simulations were carried out with the differentially heated cavity case until the residuals for different equations reduced below 10^{-4}, 10^{-5} and 10^{-6}, and the results are shown in Fig. 4.6. There is no visible difference in the results between the three convergence criteria. It is conclusive that a convergence criterion of residuals below 10^{-5} is sufficiently accurate, and the same is applied for all the simulations carried out in the present work.

4.2.3.5 Influence of radiation

For comparing the CFD results with the experimental data, the temperature is non-dimensionalized as

$$\theta = \frac{T - T_c}{T_h - T_c}, \tag{4.2}$$

where, T is the gas temperature, T_h is the temperature of the hot wall (= 50 °C), and T_c is the temperature of the cold wall (= 10 °C). The model with radiation captures non-zero convective heat flux values (temperature gradients) at the top and bottom adiabatic walls (Fig. 4.7). The convective heat flux at these walls is balanced by an equal and opposite amount of radiative heat flux. Temperature stratification across the height of the cavity is over a smaller range while considering radiation effect, compared to the case without

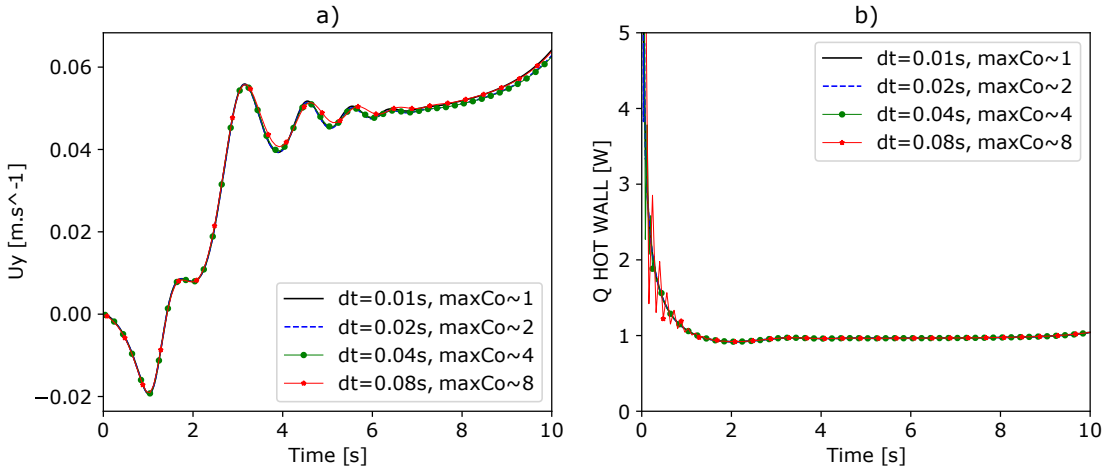

Figure 4.5: DHSC - sensitivity of the results to time-step size. a) Velocity transients at the top left corner (x = 0.03m, y = 0.72m) of the domain, b) Transients of the total heat transfer rate from the hot wall into the fluid.

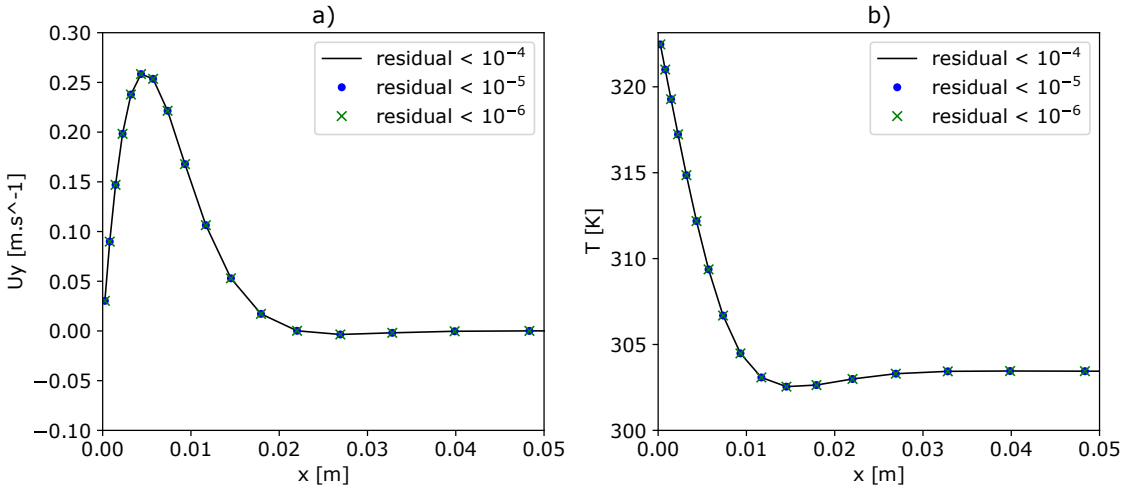

Figure 4.6: DHSC - influence of convergence criterion on results. a) Velocity profile near the hot wall at mid-height of the cavity (Y=0.5), b) Temperature profile near the hot wall at the mid-height of the cavity.

radiation (Fig. 4.7 & 4.8). Still, there exists some difference between the simulation results and experimental data, which may be attributed to the boundary conditions. In the simulation, the wall emissivity values were considered to be constant ($\epsilon = 0.3$), but the details on wall emissivity were not specified in the experimental work. Also, in the experiment, the top and bottom walls were not perfectly adiabatic as considered in the CFD model. The radiation heat transfer phenomenon not only increased the net heat flux from a wall but also reduced the convective heat flux component (Fig. 4.9), which

is consistent with the studies by Balaji and Venkateshan (1993).

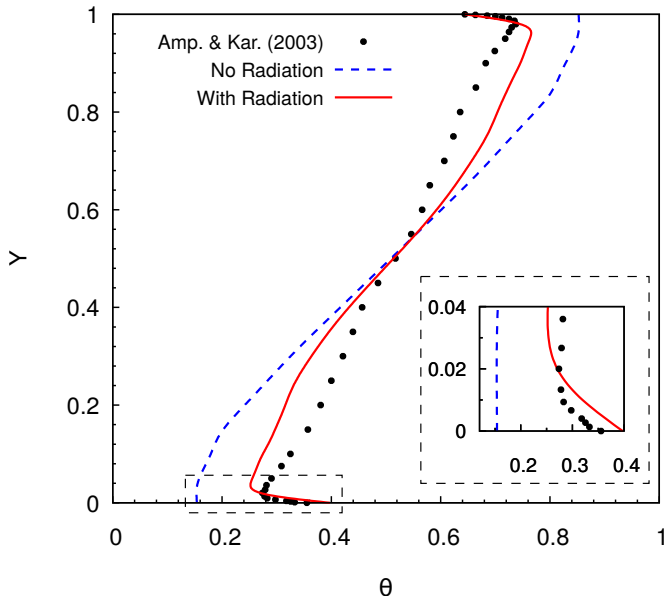

Figure 4.7: DHSC - temperature along the vertical line $X = 0.5$ (middle of the cavity) for simulations with and without radiation heat transfer.

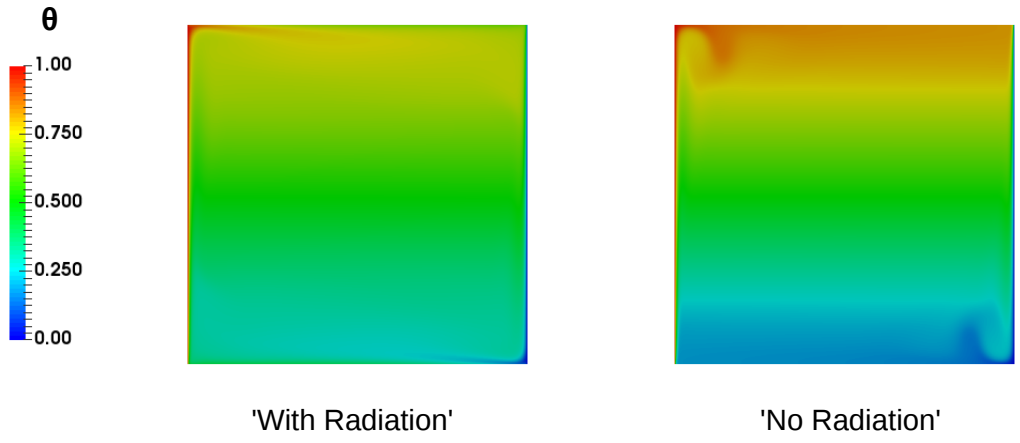

Figure 4.8: DHSC - contour plot of temperature field for simulations with and without radiation heat transfer.

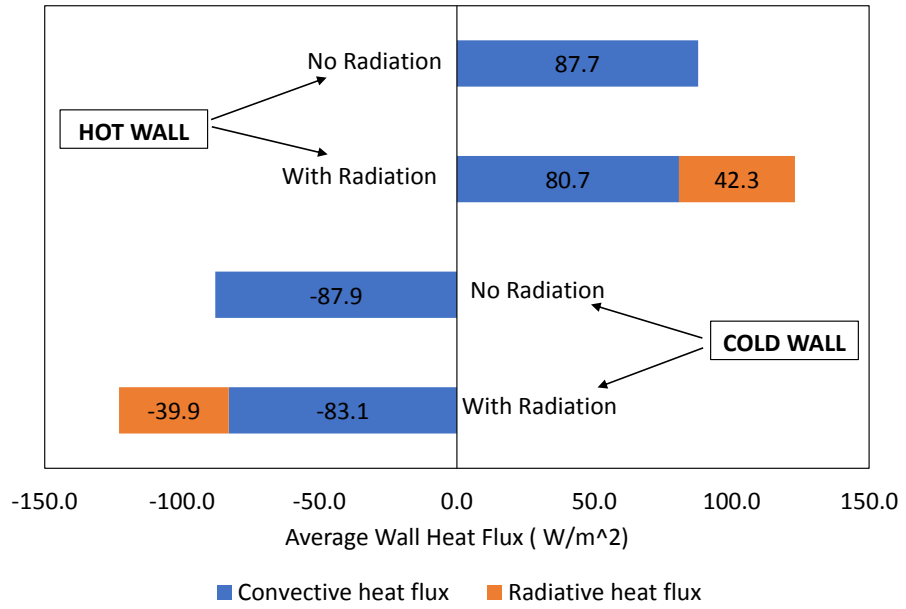

Figure 4.9: DHSC - heat flux on the hot and cold walls for simulations with and without radiation heat transfer.

4.2.3.6 Velocity, Temperature and TKE distribution

The vertical velocity, temperature, and turbulent kinetic energy distribution across the width of the cavity at mid-height are compared with the experimental data. The thermal boundary layer corresponds well to the experimental data (Fig. 4.10). The inner part of the velocity boundary layer (from wall to peak velocity) is predicted well by the CFD model. Still, the peak velocity is overpredicted, and the velocity is under-predicted in regions away from the wall (Fig. 4.11). This anomaly can only be explained with the prediction of turbulent kinetic energy (TKE). Though the trend and order of magnitude of TKE (10^{-3} $\mathrm{m^2\,s^{-2}}$) are predicted reasonably in the simulations, the magnitude of TKE is under-predicted as shown in Fig. 4.12. Lower TKE results in lower momentum diffusion and hence, the under-prediction of velocity in the outer part of the boundary layer (Fig. 4.11). Overall, the CFD model, in spite of its limitations in predicting turbulence quantities, was able to predict the mean flow quantities of velocity and temperature with reasonable accuracy. Also, in containment application, only the mean flow quantities are of interest. Hence the CFD model is taken for further validations against large-scale experiments without any improvements to the turbulence modelling.

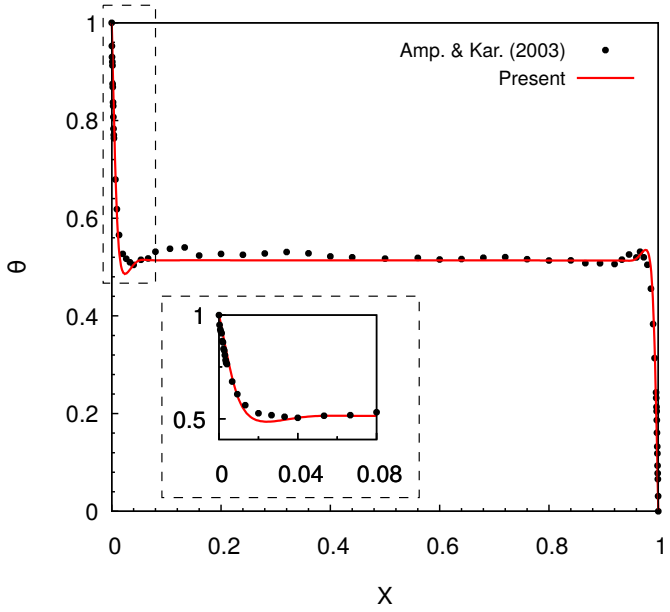

Figure 4.10: DHSC - temperature distribution across the width of the cavity at $Y = 0.5$.

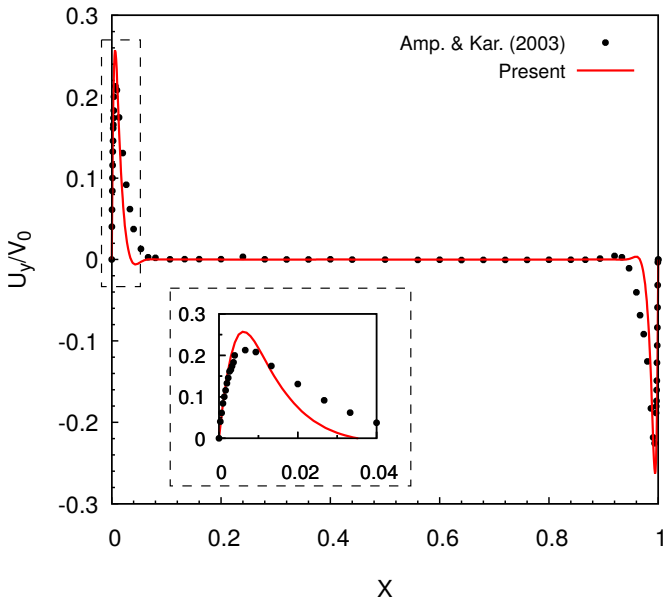

Figure 4.11: DHSC - velocity distribution across the width of the cavity at $Y = 0.5$.

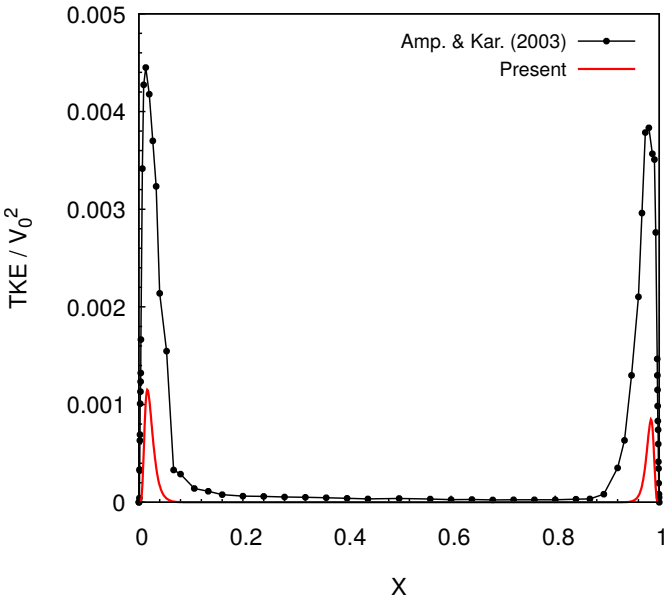

Figure 4.12: DHSC - turbulent kinetic energy distribution across the width of the cavity at $Y = 0.5$.

The fundamental assessment of the CFD model against the DHSC case showed that the wall-bounded, buoyancy-driven flows could not rely on standard wall functions applied for forced convection flows. The regions near the wall must be resolved with a fine mesh ($y^+ < 2$) to capture the wall heat flux and shear stress accurately. Time-step sensitivity studies revealed that the buoyancy-driven flows have to use time-step sizes such that the maximum Courant number is less than 4. Also, the segregated method of solving the governing equations requires a convergence criterion of less than 10^{-5} for an accurate solution. These findings are applied to the subsequent simulations discussed in the present work.

4.3 COMPARISON OF WALL CONDENSATION MODELS

In the previous chapter, two commonly used approaches—*Volumetric source terms* and *Face-flux*—for modelling wall condensation was described (section 3.1.2.2). The two models are compared based on convergence behavior, grid sensitivity, and mass conservation of the gas species to identify the computationally efficient and accurate approach of the two. For the comparison, a 2D turbulent channel flow with two species—steam (H_2O) as the vapor and air as the non-condensable gas—is chosen. The channel is 6 m in length (x-axis) and 0.45 m in height (y-axis) with an inlet at the left end and outlet at the right end. The top wall of the channel is adiabatic, while the bottom wall is the condensing interface with fixed temperature T_i = 281.45 K. The inlet boundary conditions are: U = 4.89 m/s, T = 353.15 K, Y_{H_2O} = 0.3111, and Y_{Air}= 0.6889. A turbulence intensity of 5% is used to define the turbulent kinetic energy k and eddy frequency ω at the inlet. The simulations are carried out for a physical time of 10 s, which amounts to more than eight flow passes[1], thereby achieving a steady-state.

4.3.1 Convergence behavior

The *Face-flux* method exhibited better convergence behavior and required 15% lesser computational time than the *Volumetric source terms* model.

4.3.2 Grid sensitivity

Two meshes with the first grid point normal to the wall placed in the viscous sub-layer ($y^+ \sim 1$ and total cells = 39,032) and log-law region ($y^+ > 30$ and total cells = 28,700), otherwise identical characteristics, are employed to study grid sensitivity. Due to the usage of continuous wall functions (section 3.1.2.3), grid-independent solutions are expected for both approaches. Figure 4.13 compares the wall quantities—total wall heat flux, convective wall heat flux, condensation mass flux, and wall shear stress—between the two approaches for $y^+ \sim 1$ and $y^+ > 30$ meshes. The effect of radiation heat transfer is omitted in the current work; therefore, the total wall heat flux only comprises two components, i.e., convective heat flux and latent heat flux of condensation. The two methods exhibit nearly identical wall fluxes for the $y^+ \sim 1$ mesh. Even with $y^+ > 30$ mesh, the *Face-flux* method provides comparable results to the $y^+ \sim 1$ mesh, especially for the wall shear stress and condensation mass flux quantities. Though the convective

[1]One flow pass = time taken for the fluid to move through the entire channel length with the inlet velocity (here $1.227\,\mathrm{s}$).

wall heat flux values of the $y^+ > 30$ mesh deviate from the results of $y^+ \sim 1$ mesh, it is not unduly concerning. On a condensing wall, the latent heat flux of condensation—proportional to mass flux (Eq. (3.17))—overwhelms the convective component. Since the mass flux due to condensation is calculated in a grid-independently, the prediction of latent heat flux, and thus, the total heat flux is less sensitive to the near-wall grid resolution. On the other hand, the *Volumetric source terms* model showed strong grid dependence, with the results of $y^+ > 30$ mesh deviating significantly from the $y^+ \sim 1$ mesh.

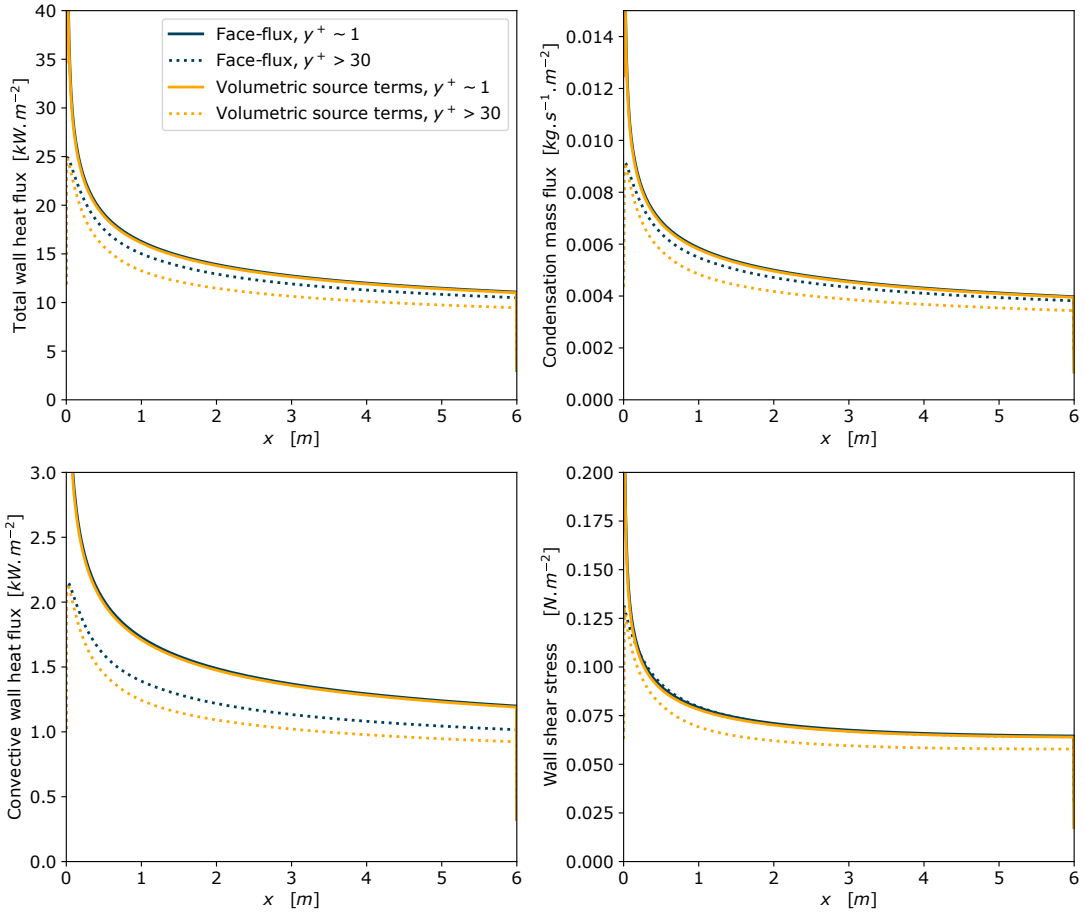

Figure 4.13: Grid sensitivity of the *Face-flux* and the *Volumetric source terms* models, based on local fluxes on the condensing wall: total wall heat flux (left top), condensation mass flux (right top), convective wall heat flux (left bottom), and wall shear stress (right bottom).

4.3.3 Mass conservation

The total mass and individual species mass balance are critical properties for a CFD analysis. Here, the mass flow rate error for a species is the difference between the mass

flow rate entering and leaving the computational domain. Steam enters via the inlet and leaves through the outlet and the condensation interface (Eq. (4.3)). Air being the non-condensable species, the error is defined as in Eq. (4.4).

$$\dot{m}_{H_2O,\text{error}} = |\dot{m}_{H_2O,\text{inlet}} - \dot{m}_{H_2O,\text{outlet}} - \dot{m}_{\text{condensation}}| \tag{4.3}$$

$$\dot{m}_{Air,\text{error}} = |\dot{m}_{Air,\text{inlet}} - \dot{m}_{Air,\text{outlet}}| \tag{4.4}$$

From Table 4.2, it becomes obvious that the species mass conservation is violated for the *Volumetric source terms* method on the $y^+ > 30$ mesh.

Model	Mesh	$\dot{m}_{H_2O,error}$ (% of $\dot{m}''_i$)	$\dot{m}_{Air,error}$ (% of $\dot{m}''_i$)
Face-flux	$y^+ \sim 1$	0	0
Face-flux	$y^+ > 30$	0	0
Volumetric source terms	$y^+ \sim 1$	0.8	0.8
Volumetric source terms	$y^+ > 30$	15	15

Table 4.2: Comparison of the species mass conservation errors for the *Volumetric source terms* and *Face-flux* wall condensation models on $y^+ \sim 1$ and $y^+ > 30$ meshes.

Grid-sensitivity and mass conservation errors with the *Volumetric source terms* approach can be understood by integrating the terms corresponding to condensation, over the control-volume. For an arbitrary transport variable ϕ, where $\phi \in U, Y_j, h, k$ and ω, the net quantity removed due to condensation with the *Volumetric source terms* approach is $\dot{m}''_i A_i \phi_c$, whereas for the *Face-flux* method, the value is $\dot{m}''_i A_i \phi_i$. The *Volumetric source terms* approach removes transport quantities present at the first cell-center instead of the transport quantities at the condensing interface. Larger the distance of the first-grid point from the wall, greater is the miscalculation, and thus the grid-dependence and mass conservation errors. Furthermore, the no-slip velocity condition at the interface with the *Volumetric source term* approach is unphysical, as it cannot capture the "suction effect" due to condensation. The "suction effect" causes the thinning of boundary layers—enhanced near-wall gradients—leading to increased mass, momentum, and heat transfer. Dehbi *et al.* (2013) proposed a modified correction factor to overcome this deficiency of the *Volumetric source terms* method. Such a correction is unnecessary for the *Face-flux* model, as the suction velocity, imposed on a condensing wall, captures the thinning of boundary layers.

In conclusion, the *Face-flux* approach was superior to *Volumetric source terms* on all counts: convergence behavior, grid-independence, and mass conservation. In addition to this, no correction is needed to account for the "suction effect". Thus, the results discussed from hereon will be limited to the *Face-flux* model.

4.4 SETCOM

4.4.1 SETCOM experimental facility

The SETCOM experiments were conducted at Forschungszentrum Jülich GmbH in close cooperation with RWTH Aachen University to study the wall condensation of steam in the forced convection and mixed convection regimes (Kelm *et al.*, 2019*b*). The experiments were sponsored by the German Federal Ministry for Economic Affairs and Energy (BMWi Grant No: 1501489). Figure 4.14 illustrates the setup of the SETCOM facility. The condensation channel is $6\,\mathrm{m}$ in length and comprises of three adiabatic sidewalls and a cooled aluminum plate (condensing wall). The adiabatic sidewalls have heated window cut-outs, at certain positions, for optical instrumentation. Type PT100 resistance thermometers measure wall temperatures inside the cooled aluminum plate, thus estimating wall heat fluxes. SETCOM facility's inclination angle can be seamlessly varied between $90°$-$0°$, i.e., vertical position to horizontal position, thereby changing the angle of the gravitational acceleration to the flow stream and thus allowing for flow investigations in both the forced convection and mixed convection regimes. The test series on forced convection considered in the current work was conducted in a vertical position. Liquid coolant in the heat exchanger, which controls the condensing wall temperature, is at $281\,\mathrm{K}$. Three steam generators, with a maximum total thermal power output of $150\,\mathrm{kW}$, supply steam. Airflow from the blower passes through a pre-heater section and then takes a $180°$ turn, to pass through a flow straightener leading to the condensation channel. One of the SETCOM facility's primary objectives is to investigate wall condensation for a wide range of Reynolds and Grashof numbers; therefore, the bulk flow passing through the condensation channel can be kept to temperatures up to $100\,°\mathrm{C}$, a relative humidity of up to $99\,\%$, and an inlet velocity in the range of $0.5\,\mathrm{m\,s^{-1}}$ to $5\,\mathrm{m\,s^{-1}}$. Kelm *et al.* (2019*b*) describes the SETCOM facility in more detail.

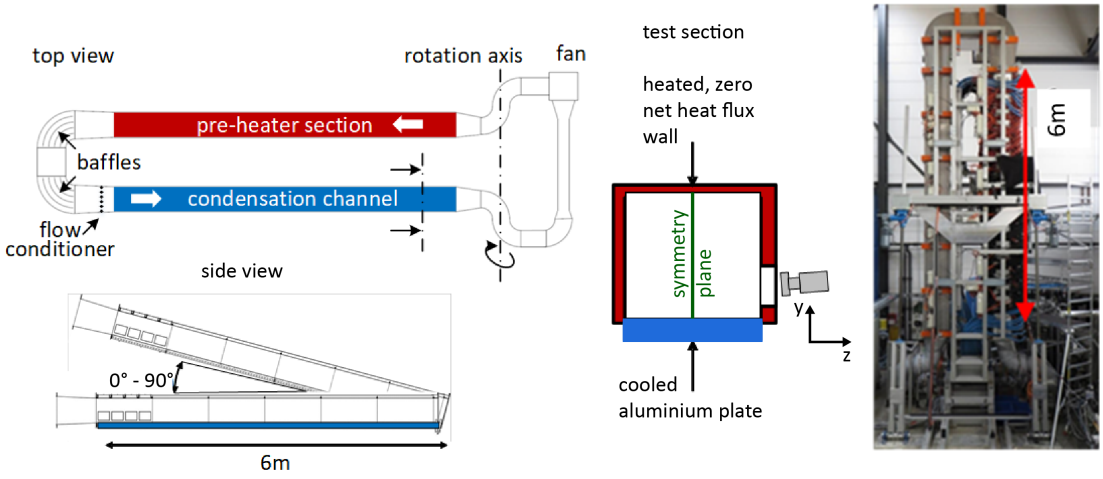

Figure 4.14: Schematic of the SETCOM facility (left), a photograph of the facility in vertical position.

4.4.2 Strategy

Accurate experimental measurements of the local condensation rate ($\dot{m}_i''$) is required to validate the wall condensation model. With the available instrumentation in the SETCOM facility, the estimation of condensation mass flux directly from the steam concentration boundary layer is infeasible. Instead, the total heat flux, obtained by computing gradients of the measured wall temperatures in the cooled aluminum plate, provides a reasonable estimate of condensation mass flux[2]. To showcase the model validity for a broad range of condensation strengths, local wall fluxes are presented for three cases, representing a high (Case 1), medium (Case 2), and low (Case 3) condensation rate. Table 4.3 discusses the boundary conditions for the cases. Finally, the integral value of total heat flux obtained from the CFD model is compared against the experimental data for the entire forced convection SETCOM database, consisting of 81 cases, ranging between mild to severe condensation rates.

4.4.3 Mesh

Figure 4.15 illustrates the overall meshing of the numerical domain and the near-wall grid refinement. The computational domain consists of the region downstream of the flow conditioner until the end of the cooling plate. Three-dimensional simulations of the entire experimental database are computationally cumbersome, and consequently,

[2]For air-steam mixtures used in the current work, the latent heat flux is an order of magnitude larger the convective heat flux; hence, the total heat flux is a representative of latent heat flux and consequently, the condensation mass flux.

Name	U_{in} [$\text{m}\,\text{s}^{-1}$]	T_{in} [K]	$Y_{\text{H}_2\text{O,in}}$ [wt. fr]	$Y_{\text{H}_2\text{O,i}}$ [wt. fr]	Re	v^+_{suc}
Case 1	4.68	353.15	0.31	0.0092	$1.07 \cdot 10^5$	-0.0140
Case 2	2.98	343.15	0.19	0.0079	$6.96 \cdot 10^4$	-0.0081
Case 3	3.95	333.15	0.06	0.0062	$9.64 \cdot 10^4$	-0.0027

Table 4.3: Boundary conditions for the three representative cases with different condensation strengths (signified by v^+_{suc}). The steam mass fraction at the condensing wall ($Y_{\text{H}_2\text{O,i}}$) is evaluated from saturation conditions at the interface temperature (T_i).

the flow is modeled with 2D block-structured meshes. The mesh is refined towards the domain inlet and beginning of the cooling plate, to capture the boundary layer development. To assess the validity of the wall functions (section 3.1.2.3), a fine mesh ($y^+ \sim 1$) and a coarse mesh ($y^+ \sim 75$) are considered. The cooled wall is modeled with the heat transfer coefficient boundary condition—effective $HTC \sim 1656\,\text{W}/\text{m}^2/\text{K}$ and $T_{\text{coolant}} = 280.65\,\text{K}$. Furthermore, the established "CFD best practise guidelines" (ERCOFTAC, 2001) are followed to minimize the numerical errors.

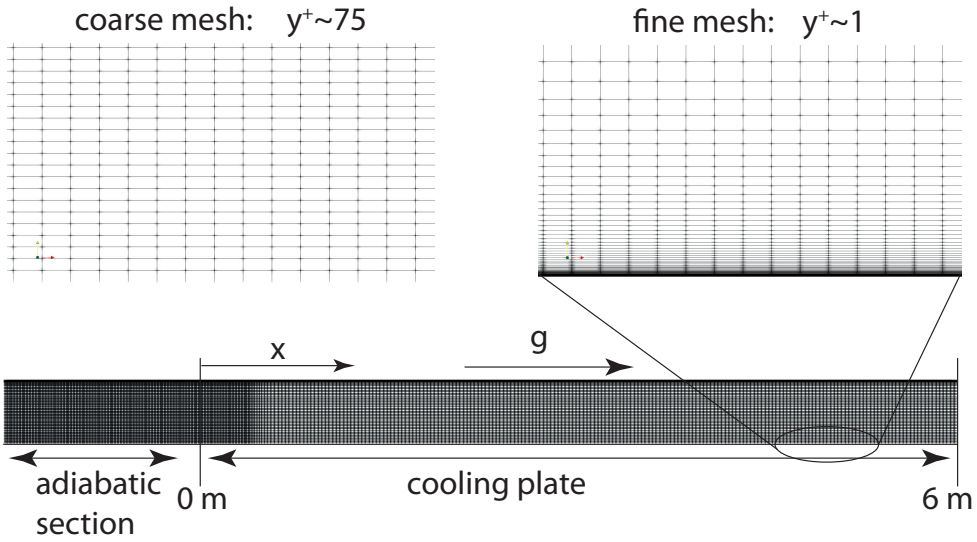

Figure 4.15: Two-dimensional computational domain of the SETCOM channel with different near-wall grid refinement for fine and coarse meshes.

4.4.4 Results

4.4.4.1 Local wall fluxes

Figure 4.17 presents the CFD model's prediction of local wall fluxes on both the fine and coarse meshes. The total heat flux values predicted with fine mesh compares very well with the experimental data for all three condensation scenarios. The coarse mesh solutions, with the first wall-normal grid point positioned in the log-law region, compared reasonably with the experimental data for $x > 3m$, where the boundary layer is developed. In the developing part of the flow, especially for $x < 1m$, the coarse mesh solution is visibly lower than the fine mesh solution; this is an expected behavior only, as the wall functions are primarily derived for fully-developed forced convection flows. No experimental data is available for the convective wall heat flux, and the wall shear stress values. Still, comparisons between the coarse and fine mesh solutions indicate similar deviations in the flow's developing part for the coarse mesh. The "suction effect" at the condensing interface also impacts the coarse solution. Wall functions used in the current work are not corrected for this "suction effect" (section 3.1.2.3), thereby leading to an increased under-prediction in the wall fluxes for the coarse mesh as the condensation rate (suction velocity) increases. The effect of suction is more prominent in Case 1, with the highest condensation rate.

4.4.4.2 Integral total wall heat flux

Figure 4.16 compares the experimental and simulated values of integral total wall heat flux, i.e., $\int_{x=0}^{6} \dot{q}''_{\text{total}}\, dx$, for all the experiments performed in the forced convection flow regime at the SETCOM facility. In total, 81 tests with a Reynolds number range of 70.000 - 100.000 and suction velocity v^{+}_{suc} of $-8.1 \cdot 10^{-3}$ to $-1.44 \cdot 10^{-2}$ is summarized. The fine mesh solutions are within an error band of $\pm 10\,\%$, with a few outliers in the $\pm 15\,\%$ range, which, however, is within the accuracy of the heat flux sensors itself. The coarse mesh results reveal a systematic under-prediction compared to the experimental data and the fine mesh solutions; this may again be attributed to the inefficacy of the wall functions for the developing part of the flow and the "suction effect."

In conclusion, the CFD model's validity was proven for a broad range of flow parameters and condensation rates. The model presented exhibits mesh insensitive results for forced convection flows in the fully developed regions, confirming the validity of the chosen wall functions. During the validation studies, a sensitivity to

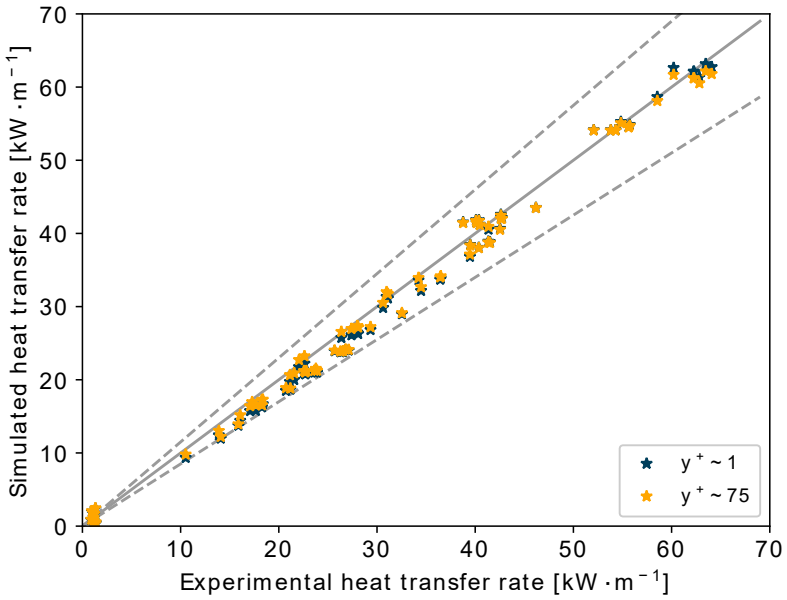

Figure 4.16: Comparison of the experimental integral heat flux with the fine mesh ($y^+ \sim 1$) and coarse mesh ($y^+ \sim 75$) solutions for 81 forced convection tests in the SETCOM facility. The dotted grey lines indicate a deviation of $\pm 15\,\%$ from the center line (solid grey line).

the inlet boundary conditions, especially the turbulence intensity and length scale at the inlet, was observed. A turbulent intensity value of $I = 10\,\%$, along with a length scale of 2.5 (channel width in the flow straightener), was found to provide the most consistent results when compared to the experimental database. Further experimental work will be carried out to characterize the inlet turbulence intensity accurately.

Though the SETCOM experiments considered in this thesis are in the forced convection regime, the results prove that the CFD model can consistently predict the wall condensation of steam in the presence of non-condensable gases. Also, the *Face-flux* wall condensation model has been shown to work on coarser grids with wall functions. This ability of the CFD model is essential if it has to be scaled to real containment applications. As a next step, the CFD model has been validated against the experiments in the technical scale THAI facility.

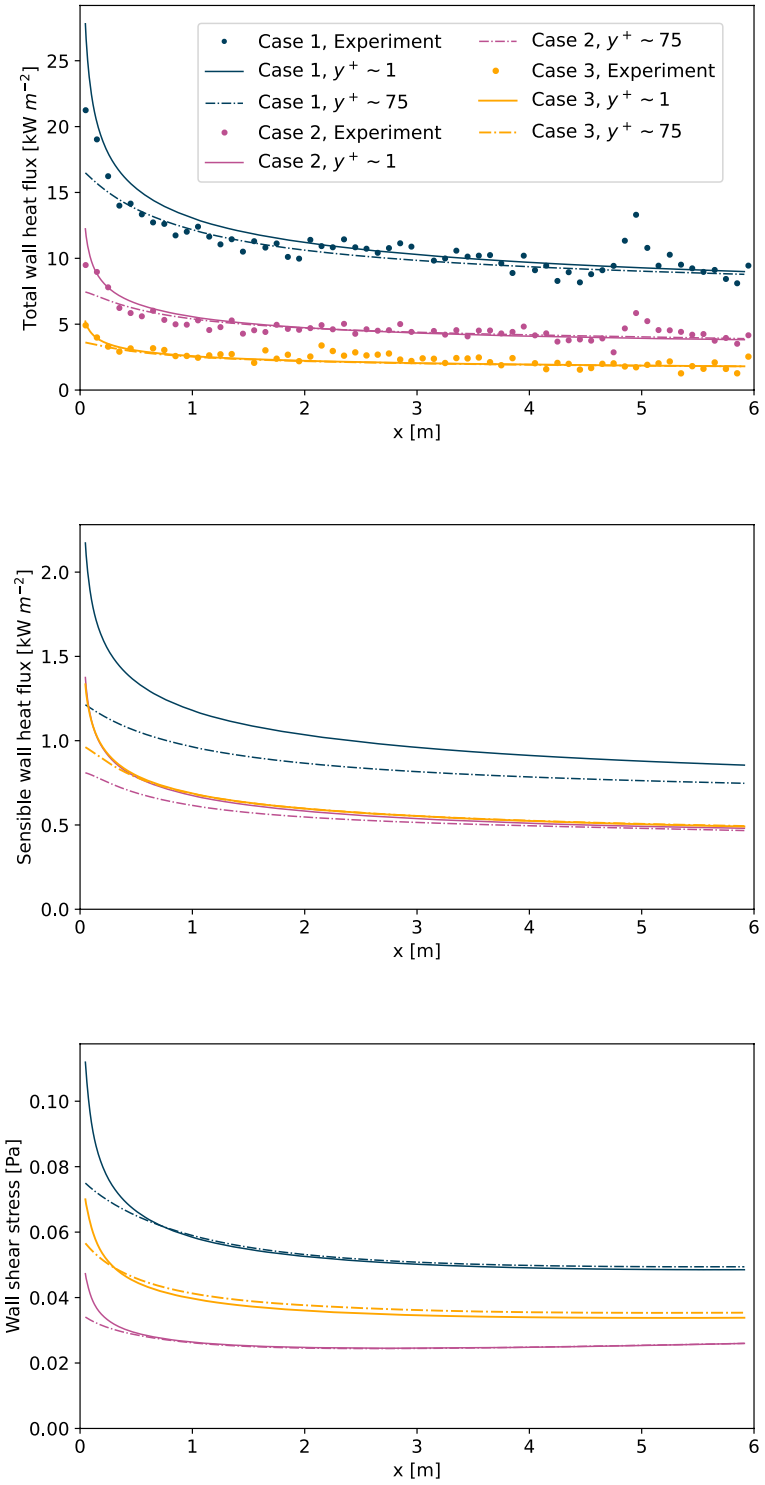

Figure 4.17: Local wall fluxes—total wall heat flux (top), convective wall heat flux (middle), wall shear stress (bottom)—along the condensing wall for three cases (differentiated by color) with the fine (solid line) and coarse (dotted-dashed line) meshes. Experimental data is available for the total wall heat flux only (dots).

4.5 THAI SERIES

To develop reliable reactor safety analysis codes, they must be validated against technical scale experiments that reasonably represent the relevant accident conditions. The THAI, an acronym for **T**hermal-hydraulics, **H**ydrogen, **A**erosols, and **I**odine, is a technical scale test facility (height = 9 m and volume = 60 m^3), operated by Becker Technologies GmbH, to study hydrogen and fission products (e.g., iodine/aerosol) related issues in a nuclear reactor containment. The THAI hydrogen-related experiments study hydrogen stratification build-up and gas mixing by either forced or natural convection, hydrogen deflagrations, and the performance of passive autocatalytic recombiners (Gupta *et al.*, 2015). The THAI experiments on fission products deal with aerosol/iodine transport, deposition on the walls, and resuspension from the walls. The interaction of the fission products with the gas mixing phenomena is also studied. This thesis aims to accurately model buoyancy-driven flows prevailing in a containment in the long term of a severe accident. In this regard, three experiments related to gas mixing by natural convection in increasing order of complexity are considered: (i) In the THAI-TH21 experiment, a turbulent natural convection flow due to differentially heated walls with a single gas species (air) is studied (Fischer *et al.*, 2009). (ii) In the THAI-TH22 experiment, erosion of a stratified helium layer due to natural convection flow is investigated (Gupta *et al.*, 2010). (iii) For the THAI-TH24 experiment, helium is replaced with steam, thereby bringing condensation effects (Gupta *et al.*, 2012). The THAI experiments were conducted by Becker Technologies GmbH and financially sponsored by the German Ministry of Economic Affairs and Energy—BMWi Grant No. 1501325 for the THAI-TH21 experiment and BMWi Grant No. 1501361 for THAI-TH22 and THAI-TH24 experiments. Figure 4.18 gives a schematic overview of these experiments.

4.5.1 Experimental setup

The THAI vessel has a height of 9.2 m and major diameter of 3.2 m with a free gas volume of 60 m^3 (Fig. 4.19). A typical nuclear reactor containment consists of multiple rooms with openings. To mimic the compartments of a reactor containment, an open inner-cylinder with diameter of 1.4 m and height of 4 m is set up. Six pipes (not shown), each with a diameter of 51 mm and thickness of 4.5 mm, are used to position the inner-cylinder. A reactor containment's steel and concrete structures possess significant thermal inertia, which affects the natural convection flow field and wall condensation. The steel structures of the THAI vessel help to study this effect: The exterior vessel has

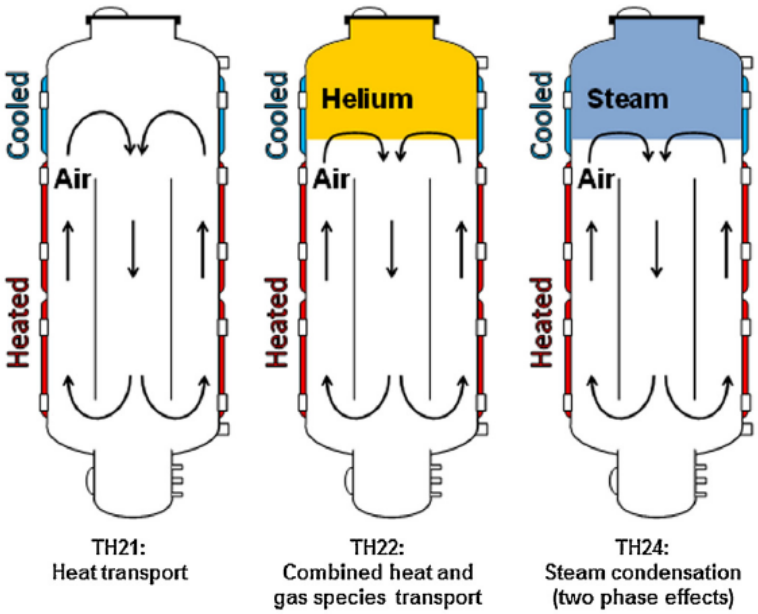

Figure 4.18: THAI experiments on buoyancy-driven flows and mixing processes (Gupta *et al.*, 2015).

a wall thickness of 22 mm and the inner-cylinder has a wall thickness of 10 mm.

Natural circulation flow in the THAI vessel is generated by the differential heating of the cylindrical vessel walls. Figure 4.19 shows the different parts of the vessel's exterior. Two heating jackets—attached to the 'lower heated' and 'middle heated' vessel walls—and one cooling jacket—attached to the 'upper cooled' wall—help maintain the wall temperatures necessary to generate the natural circulation flow. In addition, for the TH22 and TH24 experiments, the curved sections (in yellow) are intermittently heated with electrical heating to have nearly constant wall temperatures throughout the experiments. The remaining part of the outer vessel wall, such as the lid, the sump, and other small sections between the heated and cooled sections, is insulated from the ambient atmosphere by mineral wool and aluminum layers.

In the TH22 and TH24 experiments, helium/steam is injected into the upper plenum of the THAI vessel to build a stably stratified layer. This is done using an injection nozzle of 138 mm diameter, positioned at a radius of 1.14 m, height of 6.8 m, and a polar angle ϕ = 70 °. Polar angle ϕ is measured in the clockwise direction when looking from the top of the THAI vessel. From Figure 4.20, it can be seen that the injector is located above the inner-cylinder and adjacent to the cooled vessel wall.

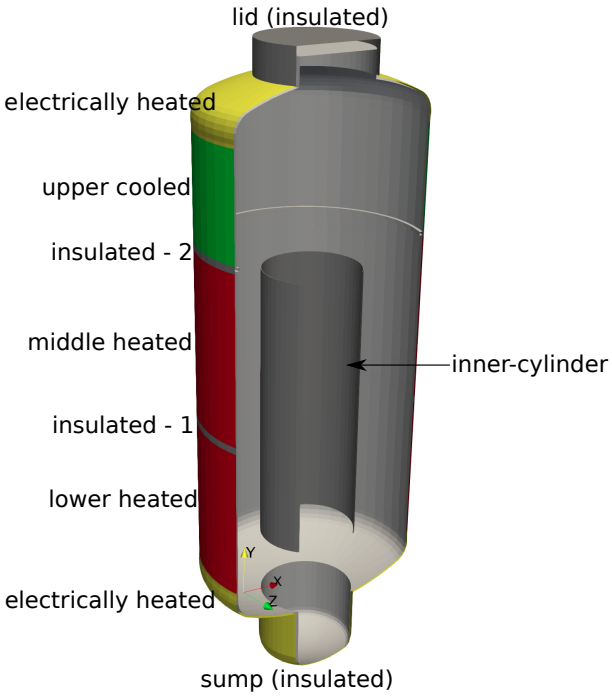

Figure 4.19: Simplified geometry of the THAI vessel (sectioned view).

The helium/steam injection flow rate in TH22 and TH24 experiments is measured with a rotameter-type transducer. 1.5-mm thermocouples with an accuracy of $\pm$ 0.3 K are placed throughout the facility to get insights into the temperature evolution and to study the gas-structure heat transfer. Fast sheathed thermocouples with an outer diameter of 0.25 mm are used to monitor the prevailing turbulence through temperature fluctuations. The pressure inside the vessel is monitored with strain-gauge type pressure transducers. The helium and steam concentration in the TH22 and TH24 experiments are measured with mass spectrometers and thermal conductivity sensors positioned throughout the gas space. Gas velocity measurements are established through Particle image velocimetry (PIV), Laser Doppler anemometer (LDA), and vane wheel sensors.

4.5.2 Mesh

The meshes were generated in the commercial grid generating tool ANSYS ICEM-CFD and then imported into OpenFOAM. The mesh is composed of hexahedral cells with low non-orthogonality and minimal skewness. For the THAI vessel, the thermal inertia of steel structures is significant and cannot be simplified with boundary conditions. Therefore, the vessel and the inner-cylinder are modeled as separate solid domains (steel) with the fluid domain (gas mixture) in contact with them (detailed views 2 and 3 in Fig. 4.20). The grids are conformal at the solid-fluid interfaces to accurately capture

the gas-solid heat exchange. The thin cylindrical pipes which support the inner-cylinder are assumed to have a negligible effect on the gas flow field and hence not considered in the mesh. The internal geometric features of size lesser than the smallest grid size were ignored, as they will not majorly influence the temperature and velocity fields. Also, a fine mesh ($y^+ < 2$) is employed in the near-wall region to accurately capture the wall fluxes—shear stress, heat flux, and condensation mass flux. For the simulations of TH22 and TH24 experiments, the injection nozzle is considered in the fluid domain, and regions near to it are sufficiently resolved to capture the jet behavior (detailed view 1 of Fig. 4.20. Grid sensitivity study is performed only for the THAI-TH21 simulations and the mesh giving grid independent results are employed for all the three THAI experiments. The discussion on grid sensitivity analyses is available in a previously published work (Kumar *et al.*, 2020), and is omitted from the current discussion for the sake of brevity. The mesh consists of approximately 8 lakh nodes in the fluid domain, 1.5 lakh nodes in the vessel domain, and 15k nodes in the inner-cylinder domain.

4.5.3 THAI-TH21: Natural convection flow of dry air

4.5.3.1 CFD setup

The THAI-TH21 experiment studies the turbulent, natural convection flow of dry air due to the differential heating of the cylindrical vessel walls. The heating/cooling jackets maintain nearly constant temperatures (± 2 °C) on the cylindrical vessel walls—lower heated and middle heated at 120 °C and upper cooled at 42 °C. Unlike the TH22 and TH24 experiments, there is no electrically heating available in the TH21 experiment on the curved sections (Fig. 4.19). The remaining part of the outer vessel walls—sump, lid, and curved sections (in yellow)—was insulated from the external environment by layers of mineral wool and aluminum. The heat loss from the THAI vessel to the ambient air through these insulation layers is modeled with a heat transfer coefficient (HTC) boundary condition (Eq. 3.19). The outside of the inner-cylinder is insulated with a layer of mineral wool and further wrapped by a thin aluminum foil. Since these insulation layers are of negligible thickness, they will not significantly influence the flow field in the vicinity of the inner-cylinder. However, the thermal properties of the insulation will affect the heat exchange at the inner-cylinder and gas interface. Therefore, these layers are not taken in the mesh but instead treated as an additional thermal resistance in the interface's conjugate heat transfer boundary condition (Eq. 3.18).

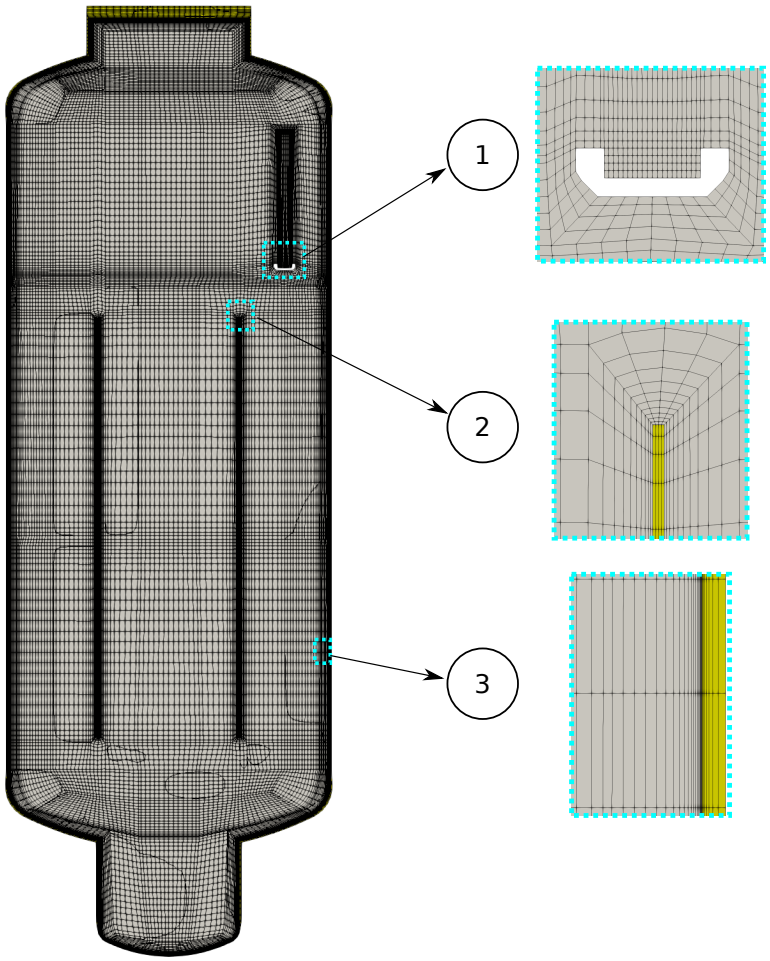

Figure 4.20: Block-structured mesh of the THAI facility (sectional view) with detailed views: (1) Fine mesh around the injector. (2) Conformal mesh at the fluid (grey) and inner-cylinder (yellow) interface. (3) Conformal mesh at the fluid (grey) and vessel (yellow) interface.

In the TH21 experiment, the air inside the THAI vessel is heated from an ambient pressure of 1.02 bar until a natural circulation flow field with a quasi-steady-state pressure of 1.2 bar is reached. The time taken to attain this state is around 12 hours (Fig. 4.21). Simulating the experiment's entire physical time of 12 hours is computationally expensive. Also, only the quasi-steady part of the flow (at 12 hours or 43200 s) is of interest. So, the simulation is started from an initial pressure and temperature such that the mass of air inside the vessel is the same as that in the TH21 experiment and continued until a quasi-steady-state is reached (simulation time = 1030 s). The simulation's steady-state pressure of 1.224 bar is higher than the experiment's value of 1.2 bar. In the experiment, the insulation of the THAI vessel from the ambient atmosphere is not uniform, which brings uncertainty in specifying the heat transfer coefficient boundary condition. This uncertainty leads to reduced heat loss through the

insulated part of the THAI vessel in the simulation (1.6 kW) compared to the TH21 experiment (3 kW) and hence the increased steady-state pressure and temperature in the simulation.

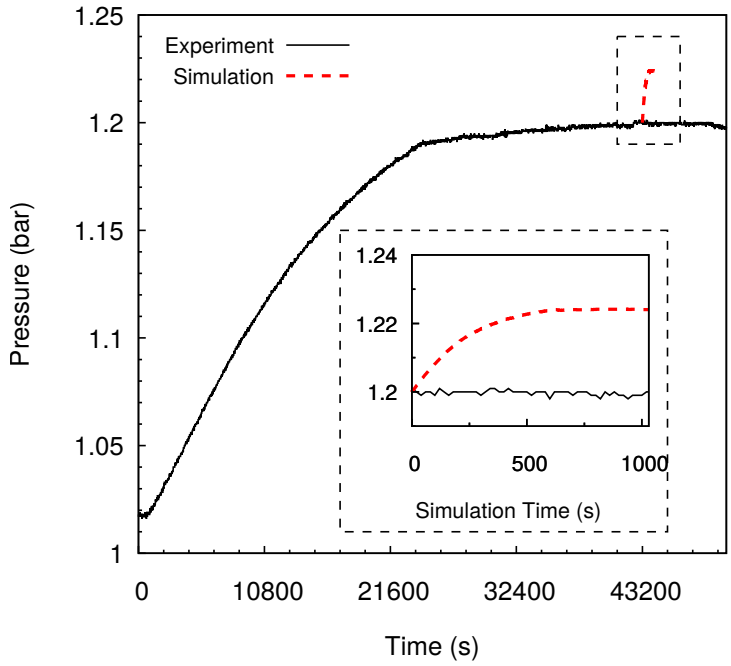

Figure 4.21: THAI-TH21: Pressure transients

4.5.3.2 Results: Flow field

Due to buoyancy, a rising flow is created near the lower and middle heated walls and a descending flow near the cooled upper walls. Instability at the interface where the rising upward flow adjacent to the heated walls and the dropping flow adjacent to the cooled wall gives rise to a three-dimensional flow field. Iso-surface of the instantaneous and time-averaged temperature field in Fig. 4.22 illustrate the three-dimensional nature of the flow-field. It is apparent that even after time-averaging the results in the quasi-steady state for 250 s, the temperature iso-surface is still not perfectly axisymmetric. In other words, simulation results will vary depending on the choice of the plane to extract velocity and temperature fields. To remove this ambiguity, circumferential averaging is performed on the time-averaged data. All the results discussed from here on are time-averaged as well as circumferentially averaged. Figure 4.23 shows the time-averaged and circumferentially averaged velocity and temperature field. The flow field is characterized by two primary convective loops, one in the heated part of the facility

and the other in the cooled section. Hot and cold fluids are continuously exchanged between the two loops. Some weaker convective loops can be seen in the annular space between the heated vessel walls and the inner-cylinder. The sampling lines along which velocity profiles (Y = 0.696 and Y = 0.533) and temperature profiles (R = 0.952 and R = 0.697) are compared with the experimental data are shown in Fig. 4.23.

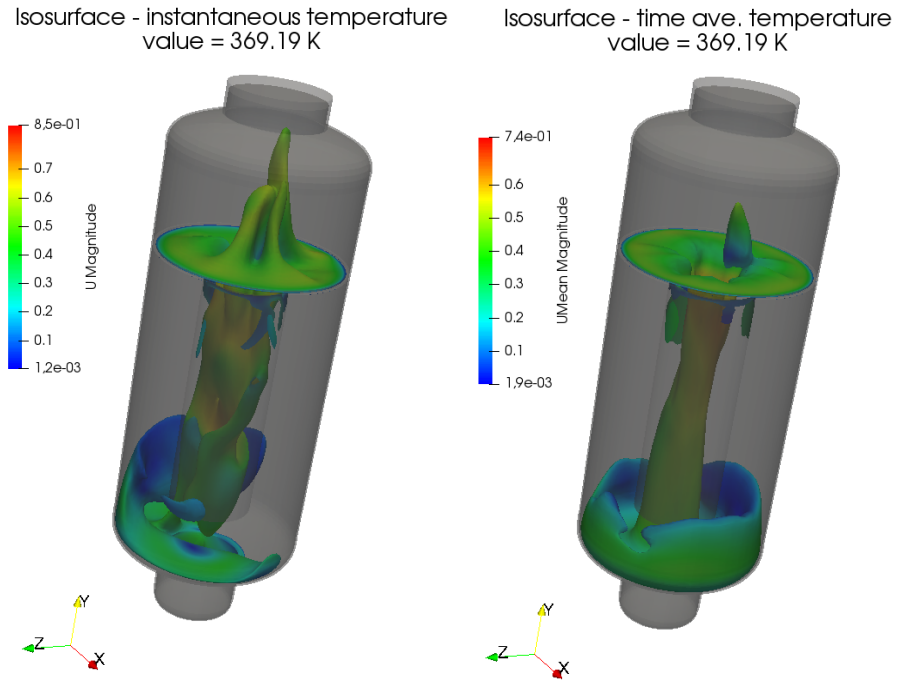

Figure 4.22: THAI-TH21: Iso-surfaces of instantaneous and time-averaged temperature (colored by velocity magnitude), illustrating the 3D nature of flow-field

4.5.3.3 Results: Effect of radiation

To understand the effect of surface-to-surface radiation heat transfer, simulations are performed with and without including the radiation model. The surface emissivity value for the vessel walls is not specified explicitly in the experimental data. All walls in contact with the gas phase except the outer surface of the inner-cylinder are steel surfaces. An emissivity value of 0.5 is assumed on the steel walls. The outer surface of the inner-cylinder is wrapped with an insulation layer and covered by thin aluminum foil. The emissivity of a new aluminum foil is 0.04, a highly reflective surface. But, aluminum is prone to oxidation, and due to this, the emissivity value can go up to 0.3. Due to the uncertainty in surface emissivity values, two simulation cases are considered. In Case 1, the outer surface of the inner-cylinder takes an emissivity of 0.04. In Case

2, this emissivity is set to 0.3. In this way, the sensitivity of the results to the choice of surface emissivity can be understood.

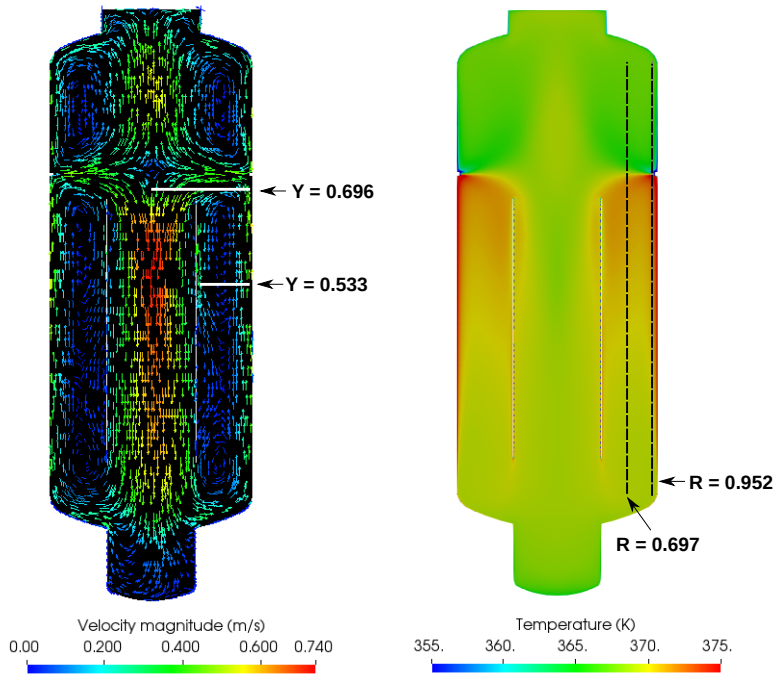

Figure 4.23: THAI-TH21: Time-averaged and circumferentially-averaged streamlines and temperature contour.

Heat transfer rates and steady-state pressure: The effect of the radiation phenomenon on the net heat transfer rates on the external walls of the THAI vessel is shown in Fig. 4.24. Surface-to-surface radiation heat transfer results in increased heat transfer rates on the external walls compared to the results where radiation modeling is ignored. The higher heat transfer rates further result in increased steady-state pressure inside the THAI vessel, as shown in Table 4.4. The heat transfer rates on external walls are higher for Case 2 than for Case 1. The higher surface emissivity value on the outer surface of the inner-cylinder for Case 2 resulted in increased heat exchange with the heated wall section of the THAI vessel and hence larger heat transfer rates and increased steady-state pressure.

Gas temperature profile: The simulations' average steady-state pressure and temperature are higher than in the experiment due to the reasons discussed in section 4.5.3.1. Also, the quasi-steady temperature differs between the simulations

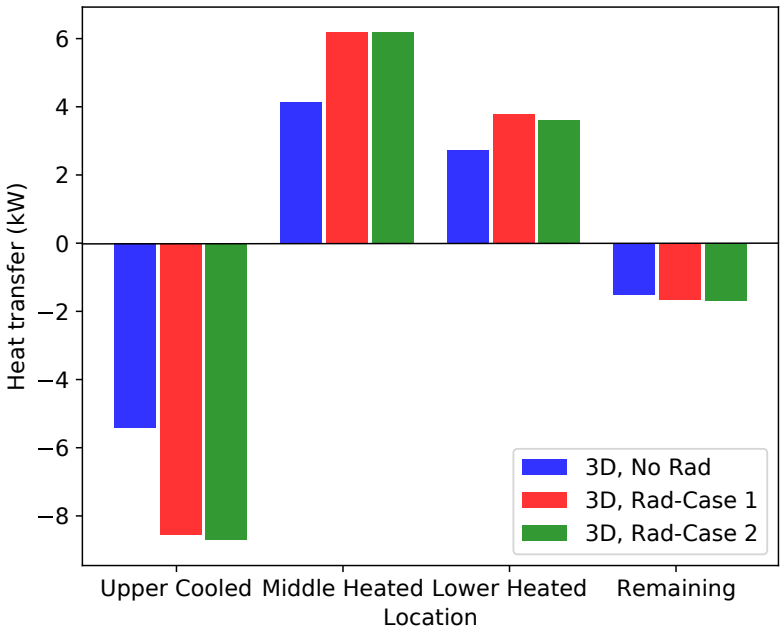

Figure 4.24: THAI-TH21: Heat transfer rates at the external walls for simulations with and without radiation.

with and without radiation (Table 4.4). Hence, directly comparing the temperature profile between the experiment and the simulations with and without radiation is not feasible. Moreover, for buoyancy-driven flows, the density gradients come about due to temperature gradients rather than the actual temperature value. Hence, only the temperature distribution with respect to the average value is of significance rather than the temperature value itself. So, the temperature fields are non-dimensionalized with their corresponding volume average temperature value, thus, making it feasible to compare temperature distribution between experimental data and simulation results.

Model	Pressure (bar)	Temperature (K)
Without radiation	1.21654	367.34
With radiation - Case 1	1.22483	369.868
With radiation - Case 2	1.23021	371.67

Table 4.4: THAI-TH21: Influence of radiation heat transfer on the volume-averaged quasi-steady pressure & temperature.

The temperature distribution along the vertical line R = 0.952 close to the vessel wall is shown in Fig. 4.25. There is a good agreement between experimental data and CFD results for positions near the cooled wall (Y > 0.7). For the positions near the

heated wall (Y = 0.16 to 0.68), the trend of temperature distribution compares well between CFD results and experimental data but not the exact temperature values. The thermocouple readings were not corrected for radiation effects in the experimental data. Radiation effects on the thermocouple probes being predominant near the heated wall section than the cooled wall explain the ambiguity between CFD results and experimental data. It must be kept in mind that the radiation effect under discussion here concerns the measurement technique in the experiment and not the radiation heat exchange between the different walls of the THAI vessel. The temperature profile close to the wall does not vary much between cases with and without radiation, as shown in Fig. 4.25.

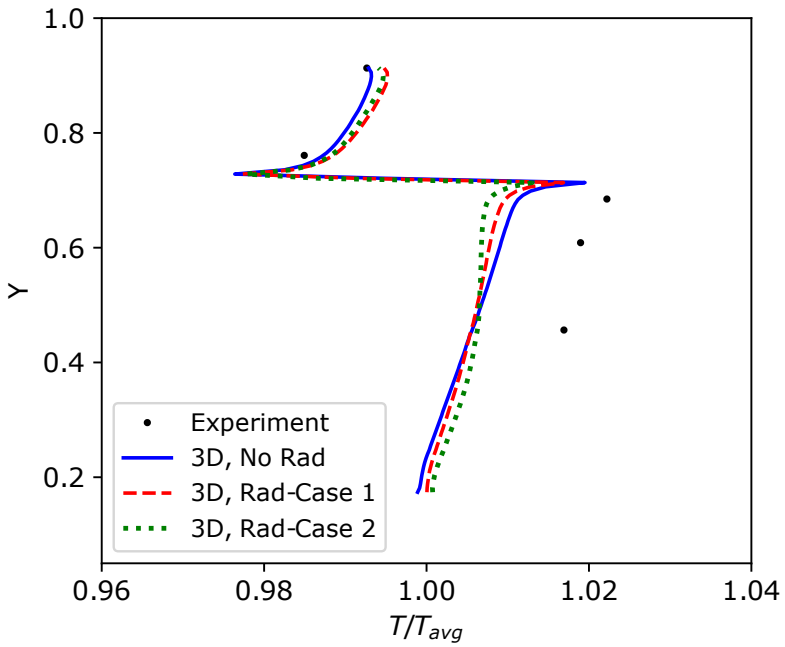

Figure 4.25: THAI-TH21: Temperature variation with height at non-dimensional radius R = 0.952

The temperature variation with height in the annular space between the vessel wall and the inner-cylinder is plotted in Fig. 4.26. There is a temperature differential in the gas atmosphere between the regions adjacent to the heated walls and the cooled wall. For the moment, the discussion is restricted to Case 1 with radiation. The temperature jump in the gas phase along the line R = 0.952 (close to the vessel walls) is around 16 K whereas, along the line R = 0.697 (away from the wall), the temperature jump is only around 6 K. Therefore, the temperature is nearly uniform throughout the THAI

vessel atmosphere except in regions very close to the wall as it can be seen in Fig. 4.23. The temperature jump for Case 1 with radiation along the line R = 0.697 is around 5 K compares well to the experimental value of 6 K, as shown in Fig. 4.26. For Case 2 with radiation, the temperature jump is only around 3.5 K. It can be seen that the higher emissivity value on the outer surface of the inner-cylinder for Case 2, has homogenized the temperature distribution in the gas phase. For the case without radiation, the predicted temperature jump is around 8 K is higher than the experimental value of 6 K. From these results, it can be inferred that the surface to surface radiation heat transfer homogenizes the temperature distribution in the gas phase. The choice of emissivity value of 0.04 for the Aluminum foil in Case 1 gives better results.

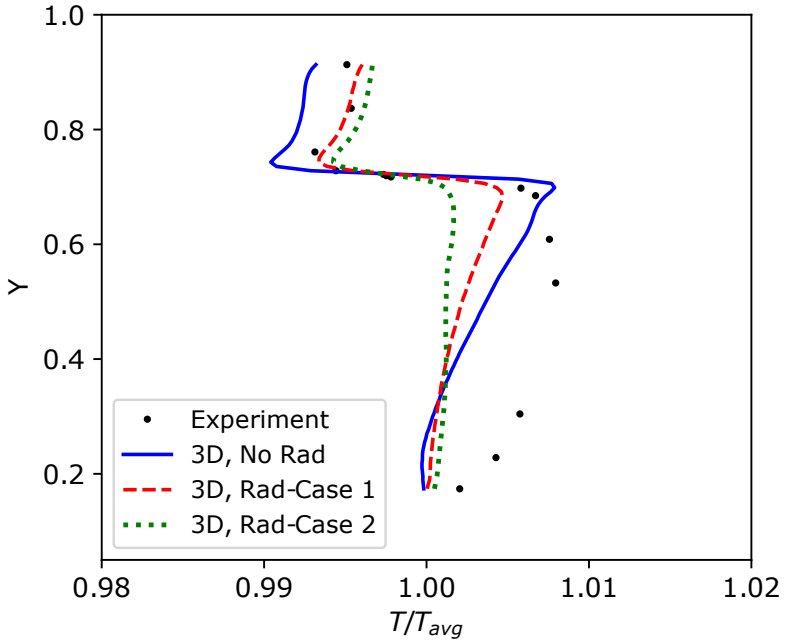

Figure 4.26: THAI-TH21: Temperature variation with height at non-dimensional radius R = 0.697

Temperature on solid walls: The temperature of the internal walls of the THAI vessel in contact with the gas is responsible for the buoyancy-driven flow and temperature distribution in the gas atmosphere. Due to the high thermal conductivity of steel, the temperature of inner vessel wall regions adjacent to the heated/cooled external walls is almost the same as the outer wall temperatures. It is not influenced by the radiation effect existing among the internal walls. The surface-to-surface radiation effect affects the temperature of internal walls adjacent to the insulated part of the THAI

vessel and the outer surface of the inner-cylinder. The sump region is closer to the heated walls of the THAI vessel. Due to radiative heat exchange between the heated walls of the THAI vessel and the sump region, increased temperatures can be found on the sump region for simulations considering radiation effect, as shown in Fig. 4.27. Similarly, the inner-cylinder is heated differentially due to radiative heat exchange from the heated and cooled portions of the THAI vessel, as shown in Fig. 4.28. The upper part of the inner-cylinder is more close to the cooled wall, and hence it is at a lower temperature compared to the lower part of the inner-cylinder.

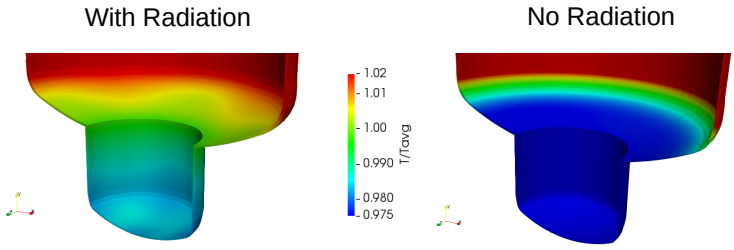

Figure 4.27: THAI-TH21 - temperature contour of the sump region of THAI vessel (sectioned view) for simulations with radiation (Case 1) and without radiation.

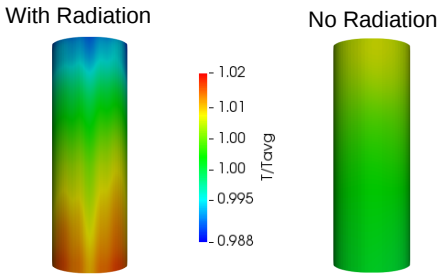

Figure 4.28: THAI-TH21 - temperature contour of the outer surface of the inner-cylinder for simulations with radiation (Case 1) and without radiation.

Velocity profile: The velocity profile is plotted along the line Y = 0.533 in the annular space between the inner-cylinder and heated vessel wall, as shown in Fig. 4.29. Near the vessel wall, there is an ascending flow, and near the inner-cylinder, there is a weak downward flow subjected to turbulent fluctuations. This happens because the inner-cylinder is provided with insulation, and hence it is cooler than the surrounding. For the Case 1 with radiation, with an emissivity of 0.04 on the outer surface of the inner-cylinder, the ascending flow near the heated wall is predicted well. Still, the descending

flow closer to the inner-cylinder is overpredicted. The highly reflective (low emissivity) inner-cylinder wall has resulted in lower temperatures and hence an overprediction of downward velocity. For Case 2, the inner-cylinder wall is at a higher emissivity (0.3), resulting in increased radiative heat exchange and higher surface temperatures than Case 1. The higher surface temperatures resulted in a reduced downward flow near the inner-cylinder wall for Case 2. It is conclusive that the velocity profile in the annular space between the inner-cylinder and the heated vessel wall is highly sensitive to the choice of emissivity value on the outer surface of the inner-cylinder. An overall better prediction of the velocity profile is obtained for the case without considering the radiation effect. This result does not necessarily mean that radiation modeling should be ignored in the simulations, but it further reinforces the importance of sensitivity of the results to the wall emissivity value. The difference in the flow-field is a result of increased temperature levels on the internal walls for the cases with radiation (Fig. 4.27 & 4.28) and hence the generation of excess buoyant forces.

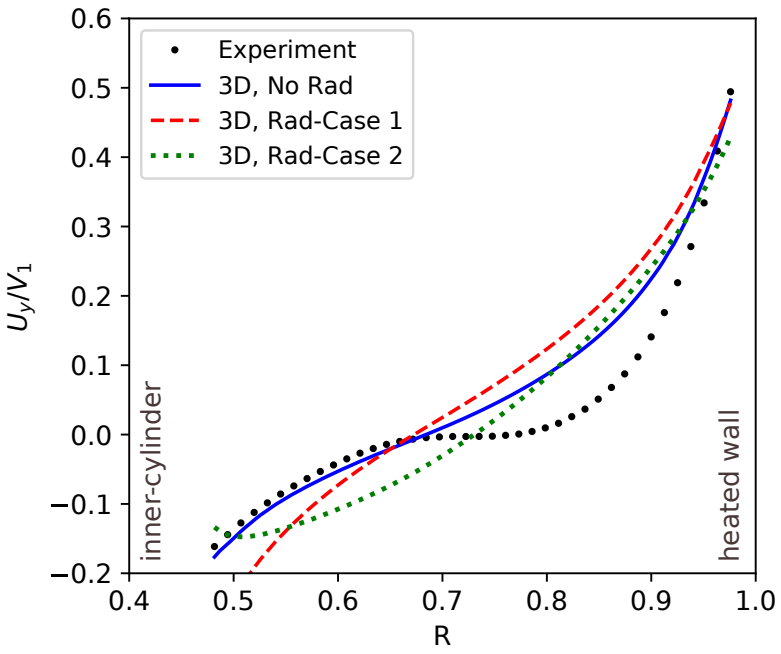

Figure 4.29: THAI-TH21 - velocity profile at Y = 0.533 for simulations with 3D model, with and without radiation.

The velocity profile is also plotted along the line Y = 0.696, as shown in Fig. 4.30. The ascending flow near the heated wall is predicted well. Away from the vessel wall, the radial component of the velocity is predominant (flow going towards the axis and into the inner-cylinder compartment). However, a weak downward velocity

is available directly above the annular space ($R = 0.44$ to 0.8). This downward flow is overpredicted in the simulation without radiation and Case 1 with radiation. There is very little difference in the velocity profile along Y = 0.696 between the simulation without radiation and Case 1. For Case 2, with higher emissivity on the inner-cylinder wall, the velocity profile significantly varies with the results of Case 1 and without radiation simulations.

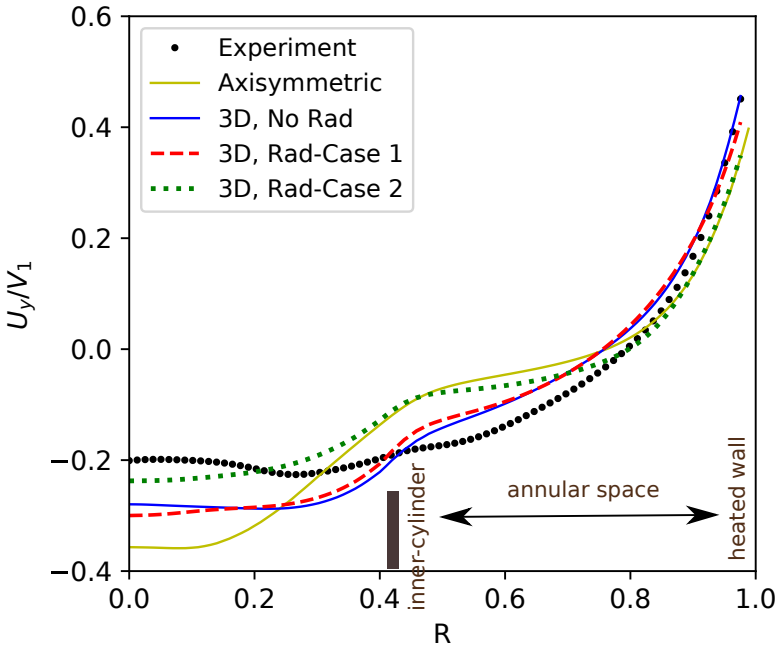

Figure 4.30: THAI-TH21 - velocity profile at Y = 0.696 for simulations with axisymmetric model and 3D model, with and without radiation.

The surface-to-surface radiation heat exchange significantly influences the temperature on the solid walls, the temperature in the gas phase, the heat transfer rates at the external walls of the THAI vessel, the steady-state pressure inside the vessel, and the flow field in the gas phase. The velocity field is susceptible to the choice of the surface emissivity values on the vessel. In the future, it is recommended that the wall emissivity values should be quantified in the THAI experiments to remove modeling uncertainty. Overall, the simulation results are in reasonable agreement with the experimental data. The CFD model was proven capable of predicting a turbulent, natural circulation flow with conjugate heat transfer involving a single gas species.

4.5.4 THAI-TH22 - Natural convection driven helium layer erosion

The primary objective of the THAI-TH22 experiment is to study the erosion of a light gas cloud by the persisting natural convection flow field in the differentially heated THAI vessel. Helium gas with its low molecular weight and high specific heat capacity ($4\ \mathrm{kg\,kmol^{-1}}$ and $5.2\ \mathrm{kJ\,kg^{-1}\,K^{-1}}$) acts as a simulant for the light gas hydrogen in a containment ($2\ \mathrm{kg\,kmol^{-1}}$ and $14.3\ \mathrm{kJ\,kg^{-1}\,K^{-1}}$). Gas molecular diffusion due to the presence of two species is an additional phenomenon compared to the THAI-TH21 experiment.

4.5.4.1 Experimental procedure

The TH22 experiment consists of three phases. The first phase of the TH22 experiment is comparable to that of the TH21 experiment. A natural convection flow of dry air is established by the differential heating of the vessel walls. The heat exchangers ensure almost isothermal temperatures (± 2 °C) on the cylindrical walls: The 'lower heated' and 'middle heated' walls are maintained at a temperature of 120 °C, whereas the 'upper cooled' wall is kept at 40 °C. The electrical heating on the curved sections at the top and bottom (Fig. 4.19) reduces heat loss through these walls and ensures good thermal control. The remaining parts—lid, sump, and the sections between the heated/cooled walls—are insulated with mineral wool. The differential heating on the cylindrical walls increases the pressure from an ambient pressure of 1 bar to the quasi-steady-state pressure of 1.2 bar in about four hours. In the TH21 experiment, similar quasi-steady-state pressure was reached slowly (12 hours), because of the absence of electrical heating on curved sections. In the second phase of the experiment, helium gas is injected into the upper plenum of the vessel for about 226 s (Fig. 4.31). The third and last phase of the experiment is monitoring the helium layer erosion process through natural convection.

4.5.4.2 CFD setup

The 'lower heated,' 'middle heated,' and 'upper cooled' walls are given isothermal boundary conditions—120 °C for the heated walls and 40 °C for the 'upper cooled' wall. Since buoyancy forces drive the flow, the simulation results will be sensitive to temperature boundary conditions. Hence the other external walls—insulated and electrically heated walls—are maintained at temperatures closer to the experimental data with a heat transfer coefficient (HTC) boundary condition. Since helium and dry-air are transparent gases, only the surface-to-surface radiation heat transport prevails.

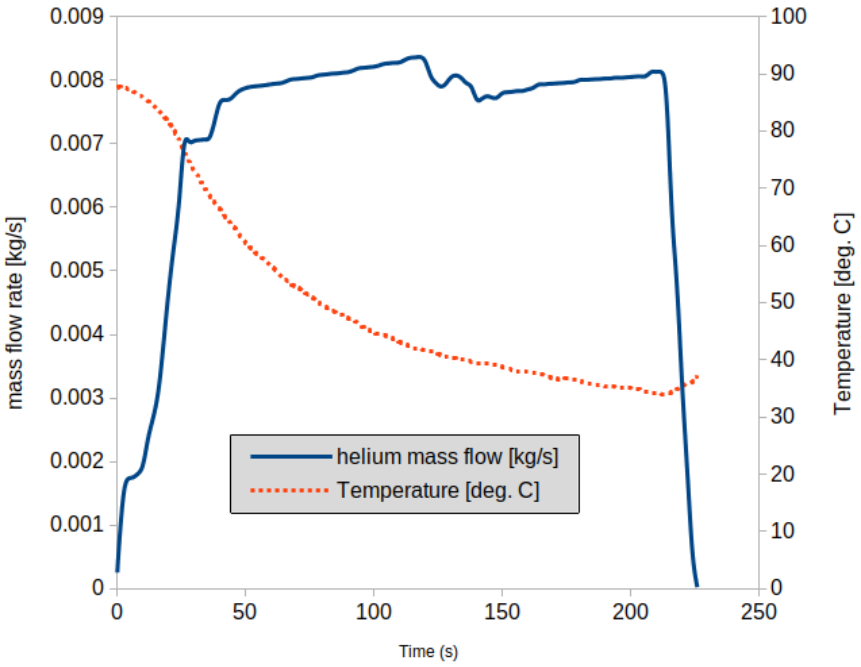

Figure 4.31: THAI-TH22: Helium injection mass flow rate and temperature.

Consequently, the fvDOM radiation model is used to capture the surface-to-surface radiation heat transfer. All the steel walls in contact with the gas mixture are specified with an experimentally determined emissivity of 0.3.

The simulation procedure for the initial phase of the TH22 experiment follows on the same lines as that of the TH21 experiment. Heating the vessel from an ambient pressure of 1 bar to the quasi-steady-state pressure of 1.2 bar over a physical time of 4 hours is computationally expensive. Hence the simulation is started from an initial pressure (1.19 bar) and temperature such that the total mass of dry air in the facility is the same as that of the experiment. A natural circulation flow field in the quasi-steady-state (pressure = 1.207 bar) is reached in the simulation and this point is fixed as the initial time, i.e., time = 0 s, for further discussions. For the helium injection phase, the transient helium mass flow rate and temperature is applied on the injector boundary for 226 s (Fig. 4.31). Following the injection phase, the simulation is continued until the helium gas distribution is homogeneous throughout the facility, indicating the completion of the erosion phase.

4.5.4.3 Discussion of results

First, the simulation results are analyzed qualitatively to get insights into the gas mixing process. Then, a thorough quantitative comparison is made between the simulation

results and the experimental data. The quasi-steady natural circulation flow existing in the vessel before the start of injection is similar to the TH21 flow-field (Fig. 4.23). A large convection loop in the lower part of the vessel with a rising flow closer to the heated vessel walls and a dropping flow into the inner-cylinder. Complementary to this, a convection loop exists in the upper part of the vessel: a downward flow closer to the cooled vessel wall and an upward flow along the axis of the vessel. After the helium injection, the convection loop between the inner-cylinder and annulus is restricted due to the blocking effect of the lower end of the light gas cloud just above the upper end of the inner-cylinder (see t = 226 s in Fig. 4.32).

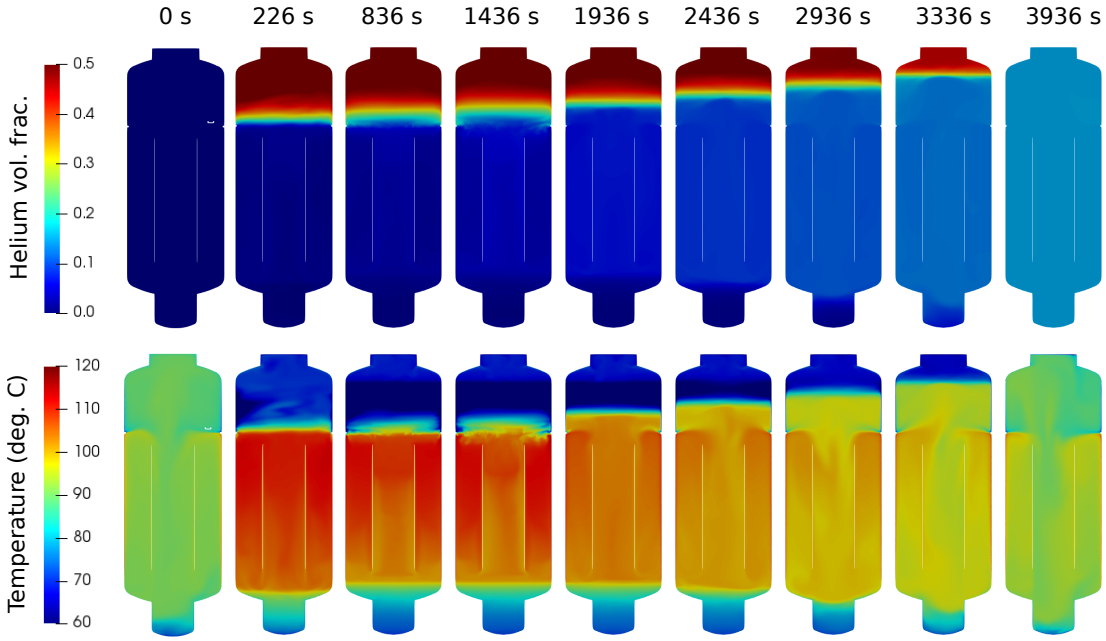

Figure 4.32: THAI-TH22: Simulated transients of the helium concentration and gas temperature (sectional view).

Figure 4.32 shows the progression of helium layer erosion and the corresponding gas temperature transients. At 226 s, a stably-stratified helium layer, formed down to the level of the injector (height = 6.8 m), has completely suppressed the natural convection flow field. The gas temperature in the helium layer is reduced because of the injected helium's lower temperature (Fig. 4.31). Below the injector, the temperature has increased due to gas compression caused by helium injection. The buoyancy forces arising out of the temperature difference between the upper and lower part of the vessel should promote mixing, but they are overwhelmed by the buoyancy effects due to

helium mass concentration gradients. At the lower edge of the helium layer, small instabilities in the flow field due to the heat diffusion from the heated walls are visible by time = 836 s. The fluctuations get stronger by time = 1436 s and promote gas mixing. By time = 1936 s, the lower edge of the helium layer had moved up, and the initial natural circulation flow is getting reestablished. Slowly the natural circulation flow erodes at the bottom edge of the helium layer (time = 2436 s). By nearly t = 4000 s, the gas mixing is complete, and helium is uniformly distributed throughout the THAI vessel.

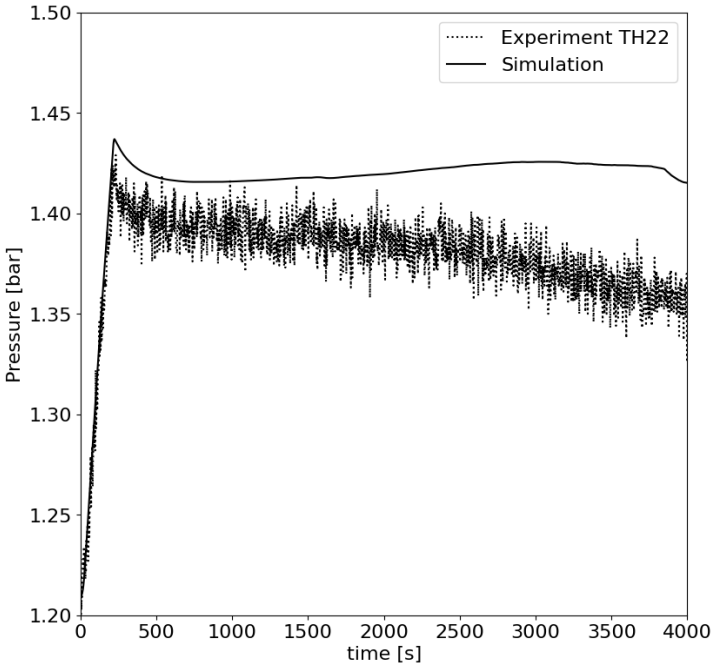

Figure 4.33: THAI-TH22: Comparison of the pressure transients between experiment (dotted line) and simulation (solid line).

The simulation predicts the pressure rise during helium injection accurately (Fig. 4.33). However, during the erosion phase, a pressure drop is visible in the experimental data while the simulation predicts an almost constant pressure (1.42 bar). In the experiment, the pressure loss ($\sim$ 0.05 bar) can be attributed to two causes: 1) Mass removal at multiple locations for helium concentration measurement. 2) Heat loss through the insulation layers in the sump and lid regions. The localized mass loss due to helium sampling in the experiments cannot be modeled with any reasonable accuracy in the simulation. Also, the non-ideal insulation cannot be modeled accurately with a HTC boundary condition. However, the simulation results are acceptable, since the previous CFD simulations of the THAI-TH22 experiment also reported this pressure deviation

due to uncertainity in temperature boundary conditions (Kelm *et al.*, 2016*c*).

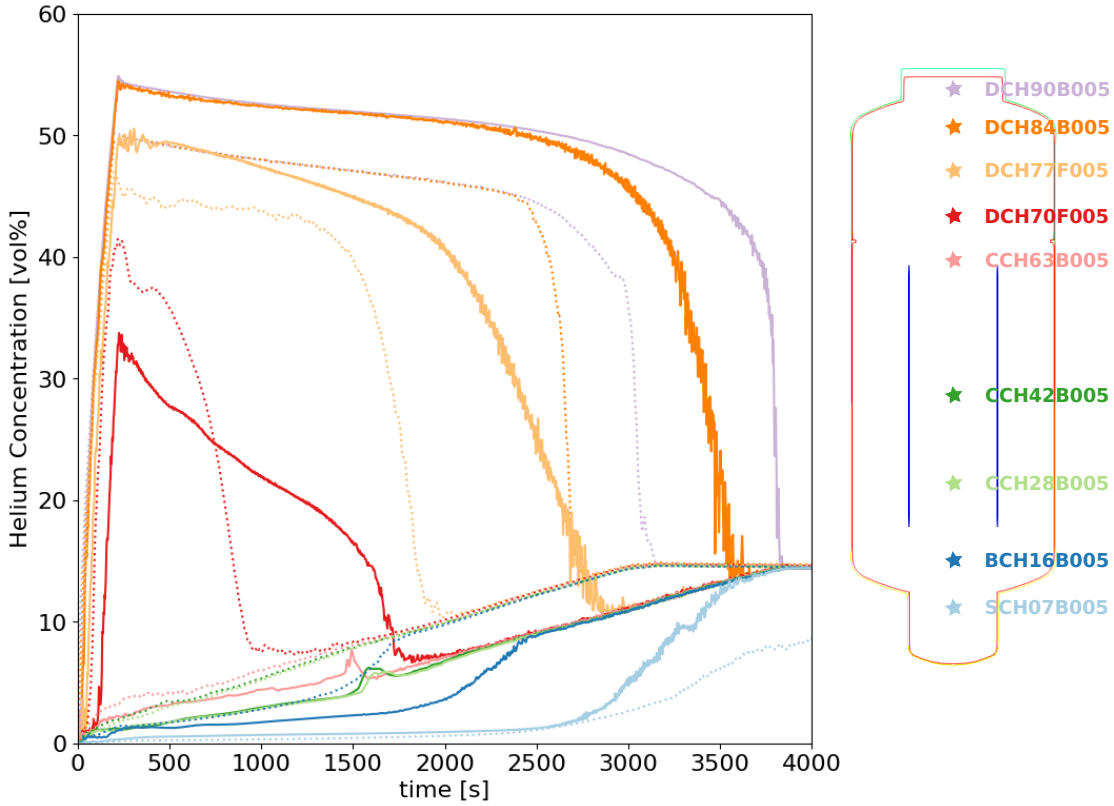

Figure 4.34: THAI-TH22: Comparison of the helium concentration transients between experiment (dotted lines) and simulation (solid lines) at different locations along the centerline.

From the helium concentration transients (Fig. 4.34), it is apparent that the simulation can capture the trend of a long diffusion-dominant slow erosion followed by rapid mixing due to natural convection. But the simulation over-predicts the mixing time compared to the experiment—about 600 s for sensor DCH90B005. At the end of the injection phase (226 s), the simulation over-predicts the helium concentration in the top part of the vessel (DCH77F005, DCH84B005, and DCH90B005) and under-predicts in locations closer to the inner-cylinder (DCH70F005). This can only be explained by a prevailing bulk motion in the experiment, which transports helium to lower levels. From the transients of the sensor DCH70F005, the experimental data shows a faster helium layer erosion indicative of gas transport into the inner-cylinder, whereas the simulation predicts a slower diffusion-dominant decay. The temperature transients (Fig. 4.35) also confirm the above arguments for the difference between the simulation results and the experimental data. Since helium is injected at a lower temperature than the ambient

temperature in the THAI vessel, the sensors (experiment) in the top part of the facility show a drop in temperature during the injection phase. The gas below the injector level is compressed, leading to temperature rise (DTF53M00, CTF42M00, CTF28M00, and BTF16M00). But the simulations over-predict the temperature rise due to compression. This is mainly because of the gap in predicting downward bulk motion into the inner-cylinder. In the experiment, as helium with high specific heat capacity moves into the inner-cylinder due to the existing bulk motion and reduces the temperature rise due to compression. Since no such mass transfer of helium happens in the simulation, it leads to a higher temperature rise.

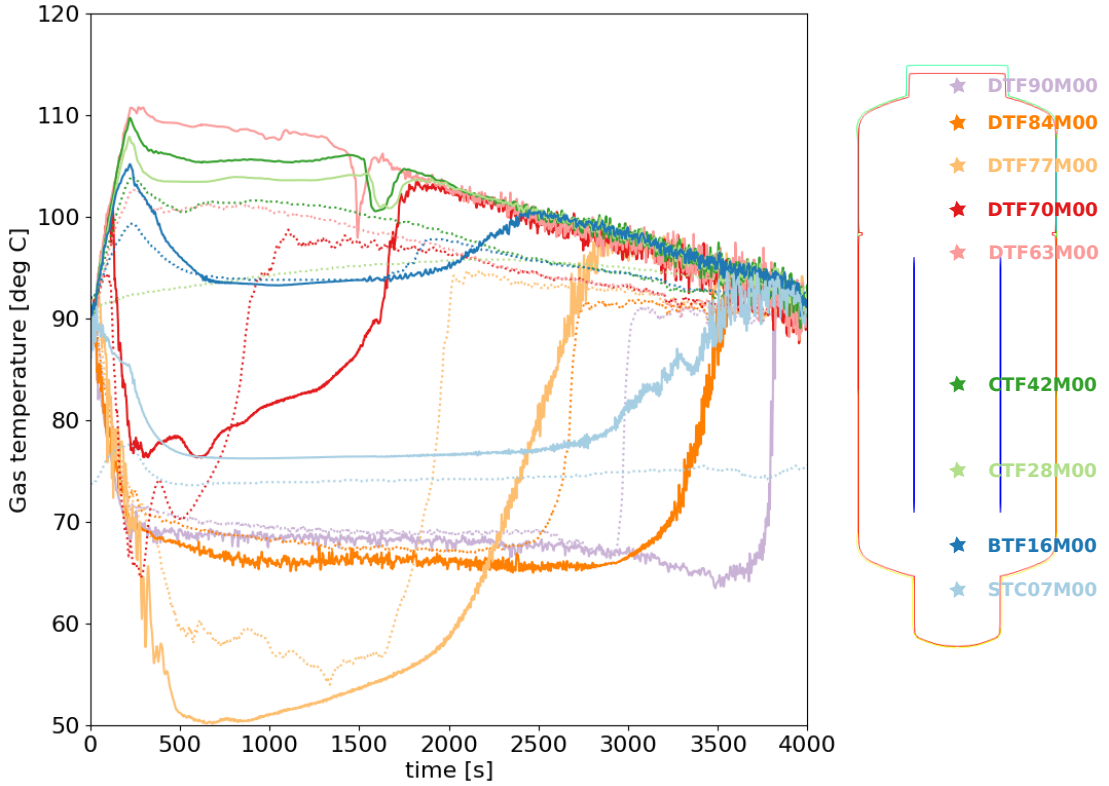

Figure 4.35: THAI-TH22: Comparison of the gas temperature transients between experiment (dotted lines) and simulation (solid lines) at different locations along the centerline.

The simulation predicts a complete blockage of flow at the end of the injection phase, whereas the experimental data indicates gas motion into the inner-cylinder. This may be attributed to two reasons: uncertainty in boundary conditions and geometric simplifications. The sump and lid sections of the vessel wall have non-uniform insulations, and therefore the heat loss through these regions cannot be modeled with

a HTC boundary condition. Also, some welded steel rings on the inner-cylinder in the actual geometry were not considered in the CFD model. From the helium contours at the end of the injection phase (Fig. 4.32), the helium cloud is located just above the inner-cylinder. Hence, the geometric simplification made on the inner-cylinder could have influenced the flow in its vicinity.

Even though the simulation predicts a slower gas mixing than the experimental data, it is clear from the pressure, helium concentration, and gas temperature transients that the CFD model can capture the overall trends of the helium layer erosion process. Moreover, the CFD model employed in the present work gives similar results compared to a previous CFD analysis conducted with commercial software (Kelm *et al.*, 2016*a*). Kelm *et al.* (2016*a*) also reported that the uncertainties in temperature boundary conditions significantly influence the gas mixing processes. Motivated by this work, a new series of experiments (TH32-34), conducted in the THAI facility, aims to reduce the uncertainties in boundary conditions. The result difference between the simulations and experiments may have been caused either due to model deficiencies, uncertainties in boundary conditions, or a combination of both. Therefore, it is recommended that the CFD model used in the present work be validated against the TH32-34 experimental series to remove the influence of uncertainty in boundary conditions, thus identifying the gaps in the model.

4.5.5 THAI-TH24 - Natural convection driven steam layer erosion

The main aim of the THAI-TH24 experiment is to study the erosion of steam-air stratification by natural convection flows. Due to the presence of steam, wall condensation and bulk condensation effects come into the picture, in addition to the effects of buoyancy, turbulence, gas diffusion, structure-gas heat transfer, and radiation heat transfer, as in the preceding experiments (TH21 and TH22). Since steam absorbs radiation, both gas and surface-to-surface radiation heat transfer effects are present in the TH24 experiment. Within the TH24 framework, four separate experiments (TH24.1 to TH24.4) were performed with minor variations in total injected steam mass, injector nozzle position, quasi-steady pressure before the onset of injection, and temperature of the heated/cooled walls. Validating the CFD model against four similar experiments does not add substantial value to the present thesis; hence, the CFD model is validated only against the TH24.3 experiment.

4.5.5.1 Experimental procedure

The TH24.3 experiment consists of the preconditioning phase and the steam injection phase. In the preconditioning phase, dry air with small steam content (about 8% by volume) is heated from ambient pressure and temperature (1 bar and 25 °C) to a quasi-steady state pressure of 1.2 bar and temperature of 94 °C), by differential heating of the cylindrical vessel walls. The oil, at a temperature of 100 °C, flowing through the heating jackets, gives the thermal control of the 'lower heated' and 'middle heated' walls (Fig. 4.19). The temperature control of the 'upper cooled' wall is obtained by oil flowing through the cooling jacket at 55 °C. The other walls of the THAI facility are maintained close to 100 °C, by a combination of adequate insulation and electrical heating so that steam condensation can happen only on the cooled wall. At the end of the preconditioning phase, a natural circulation flow field similar to the TH21 experiment and the initial phase of the TH22 experiment exists in the THAI vessel. In the second steam injection phase, steam is injected into the upper portion of the THAI vessel until the mass accounts for a steam partial pressure of 0.27 bar (Fig. 4.37). The primary steam injection is only for 500 s, after which steam mass flow is only to compensate for the steam condensing on the cold wall. The formation of a stratified steam-air layer and its subsequent dissolution due to the persisting natural circulation flow is studied in this phase. The second phase of steam injection followed by erosion, lasts for about 2500 s and ends when the steam is homogeneously mixed throughout the THAI vessel. Water draining down the cooled wall is collected and measured continuously to quantify steam condensation.

4.5.5.2 CFD setup

In the TH24 experiment, the temperature of the cooled wall varies throughout the steam injection phase due to the strong heat flux caused by steam condensation (Fig. 4.36). The wall temperature is a function of the heat flux due to steam condensation, convection, and radiation on the gas side and heat removal rate by the oil flow in the cooling jacket. Therefore, the cooled wall cannot be simplified with an isothermal boundary condition. Due to heat conduction, the heated sections adjacent to the cooled walls are also influenced by this transient temperature variation. Hence the three cylindrical walls are treated with heat transfer coefficient boundary condition as follows: 1) HTC = 45 $\mathrm{W\,m^{-2}\,K^{-1}}$ and T_{oil} = 100 °C for the 'lower heated' and 'middle heated' walls. 2) HTC = 48.5 $\mathrm{W\,m^{-2}\,K^{-1}}$ and T_{oil} = 57.3 °C for the 'upper cooled' wall. The heat transfer coefficient and oil temperature values are computed from the

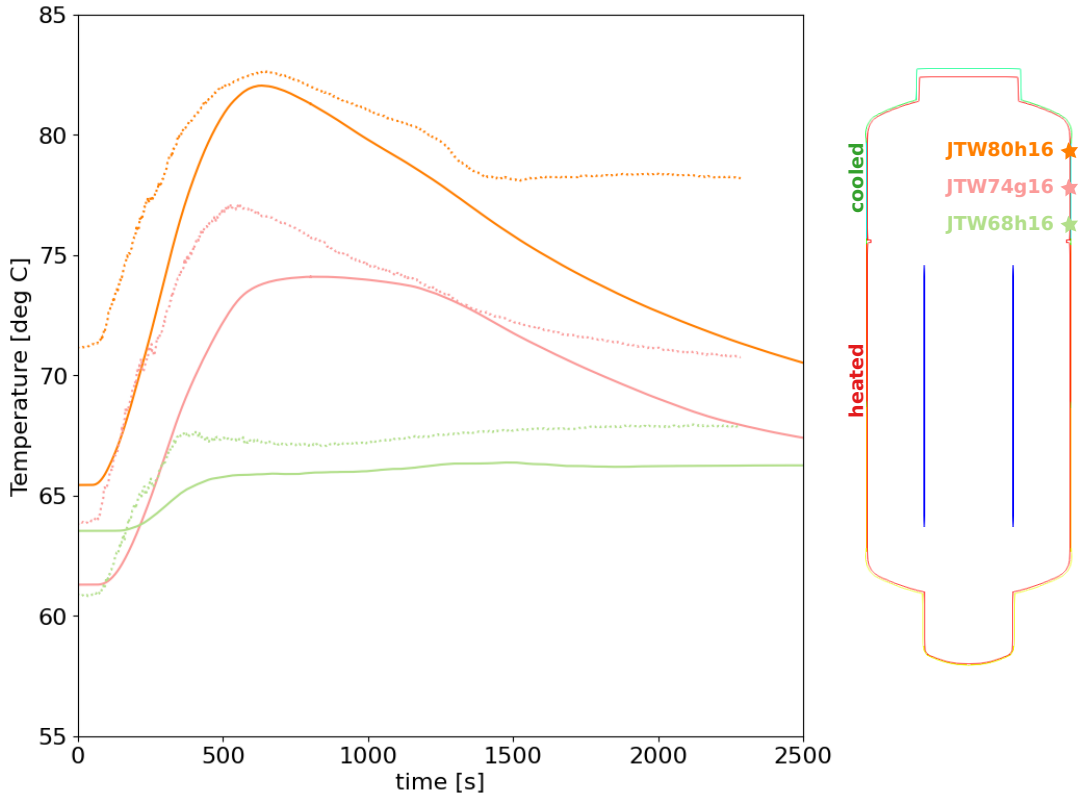

Figure 4.36: THAI-TH24: Comparison of the cooled wall temperature at different heights between experiment (dotted lines) and simulation (solid lines).

experimental data based on the oil flow rate through the heat exchangers and its inlet and outlet temperatures. The insulated walls ('insulated-1' and 'insulated-2') in between the heated and cooled walls are also treated with heat transfer coefficient boundary condition with a low HTC value (HTC = 0.7 $\mathrm{W\,m^{-2}\,K^{-1}}$ and T_{amb} = 33 °C) to account for the high thermal resistance of the mineral wool and aluminum insulation layers. The vessel's lid, the top electrically heated section, and the sump are given an isothermal boundary condition (T = 100 °C) since they are maintained at this temperature in the experiment.

The condensation phenomenon at the walls and in the bulk are captured with the *Face-flux* wall condensation model and the volume condensation model (Kelm *et al.*, 2021) respectively. The fvDOM radiation model is quite accurate for capturing surface-to-surface radiation heat transfer effects but has false scattering effects when a participative gas medium (steam) comes into the picture. Hence, the 'Monte Carlo' based radiation model (Liu *et al.* (2022)) with non-grey gas effects is preferred over the fvDOM model for the TH24 simulation. All the steel walls in contact with the gas mixture are specified with an emissivity of 0.3.

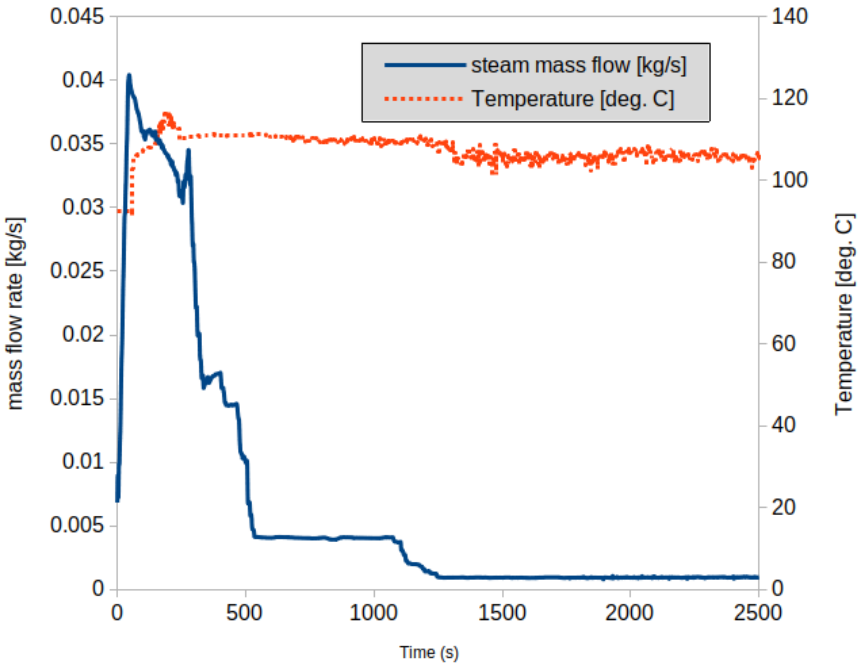

Figure 4.37: THAI-TH24: Steam injection mass flow rate and temperature.

The simulation of the preconditioning phase of the TH24 experiment is done using the same procedure as the TH21 and TH22 experiments to save computational time. In the experiment, the gas atmosphere inside the vessel is heated from ambient conditions (1 bar and 33 °C) until a quasi-steady-state (1.2 bar and 94 °C) is reached. The simulation is started from an intermediate state (1.19 bar and 89.7 °C) such that the mass of gas inside the facility is the same as that of the experiment. Thus, the quasi-steady natural circulation flow field is reached within 600 s of physical time, compared to the experimental time of approximately 19 hours.

4.5.5.3 Discussion of results

Gas mixing behavior: First, the qualitative results of the simulation will be discussed to get insights into the gas mixing mechanism, followed by quantitative comparison with the experimental data. Before the beginning of steam injection, the quasi-steady natural convection flow field resembles that of the TH21 and TH22 simulations. This is visible in the temperature contour in Fig. 4.38; it is clear that the two major convective loops are present as in the TH21 simulation (Fig. 4.23). It must be noted that the temperature field is more uniform in the TH24 simulation compared to the TH21 or TH22 cases. This is because the temperature difference between the cooled and heated

portions of the vessel is lower (∼40 °C) compared to that of the TH21 or TH22 tests (∼80 °C).

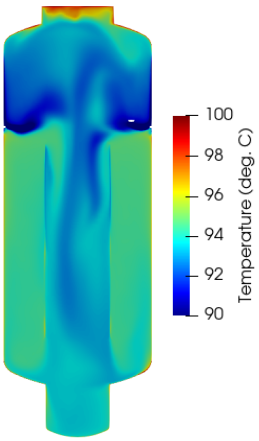

Figure 4.38: THAI-TH24: Simulated initial temperature contour indicating the quasi-steady-state natural circulation flow field

Figure. 4.39 shows the transients of the steam injection to build a stratified steam layer, followed by its subsequent erosion due to the persisting natural convection flow. By about 200 s into the injection phase, steam stratification build-up in the upper part of the facility can be seen. The high temperature of the injected steam (> 100 °C) results in increased temperature levels in the top part of the facility. Also, the temperature below the injector (heights < 6.8 m) rises beyond 100 °C due to gas compression. This means that only minimal buoyancy forces are generated by the 'lower heated' and 'middle heated' walls, which are themselves only at 100 °C. Subsequently, no visible natural circulation flow is present. By time = 500 s, the injection rate has weakened, and the stratification build-up of the steam layer is almost complete. The remaining steam injection is to compensate for the steam condensing on the 'upper cooled' wall. The active cooling due to the 'upper cooled' wall reduces the gas temperature in the upper portion of the facility. The 'lower heated' and 'middle heated' walls, themselves only at 100 °C, reduce the gas temperature in regions below the injector height. By 800 s, the gas temperature levels throughout the vessel have sufficiently reduced, and the initial natural convection flow field is returning. The rising flow adjacent to the heated sections and the downward flow adjacent to the 'upper cooled' wall erode at the steam layer. Consequently, the steam-air interface moves upwards, uncovering more of the 'upper cooled'. This further enhances the downward flow adjacent to the 'upper cooled' wall, resulting in increased mixing (time = 1300s, 1600 s). By 2000 s, the gas

mixing is complete with homogeneous steam concentration throughout the facility and the restoration of initial natural circulation flow.

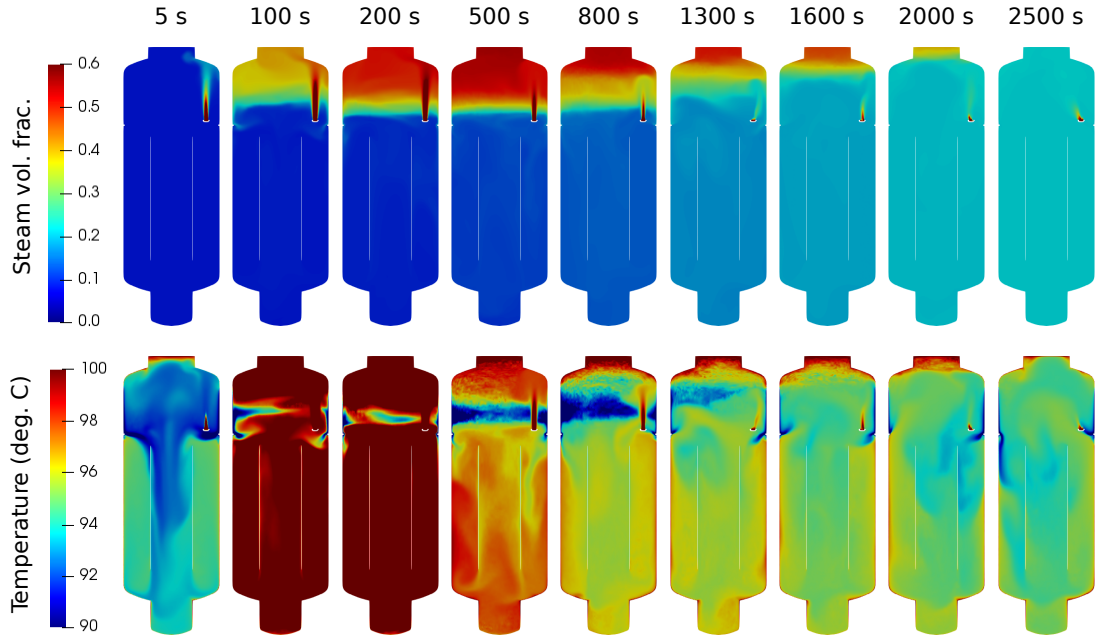

Figure 4.39: THAI-TH24: Simulated transients of the steam concentration and gas temperature (sectional view).

Pressure and Temperature: The simulation captures the trend of pressure rise during the primary injection phase (t < 500 s), followed by the stabilization during the erosion phase (Fig. 4.40). The pressure stabilizes after 500 s because the steam injection is only to compensate for the steam condensing on the walls. However, higher pressure can be seen in the experiment, even from the beginning of the injection phase. In the TH24.3 experimental notes, it is mentioned that some water droplets formed in the injection nozzle got injected along with steam during the beginning of the injection phase. These droplets evaporated downstream of the injector (height > 6.8 m), thereby increasing the pressure. This phenomenon can also be seen in the steam concentration plot (Fig. 4.41). After the gas mixing is complete, the equilibrium steam concentration in the experiment is higher (27%) compared to that predicted by the simulation (21%).

From the steam concentration transients in Figure. 4.41, overall trends of the steam concentration rise during injection followed by the depletion during erosion phase is captured by the simulation. The simulation under-predicts steam concentration at the end of the primary injection phase at a height level of 7.0 m (DCS70M00). This may

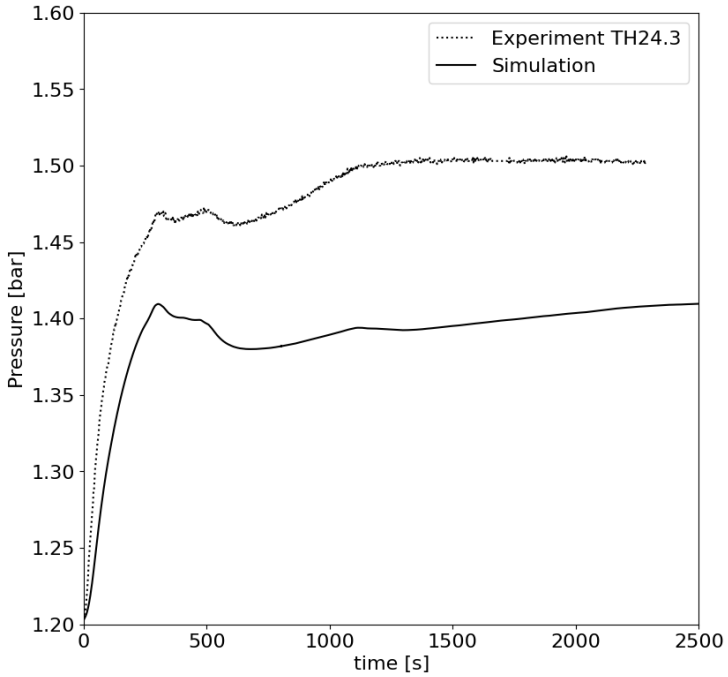

Figure 4.40: THAI-TH24: Comparison of pressure transients between experiment (dotted line) and simulation (solid line).

be attributed to the water droplet evaporation. But the simulation predicts a heightened peak steam concentration at a height level of 8.7 m (DCS87M00). This anomaly can only be explained due to the combined effect of the model's deficiency in predicting the flow field and the unquantified amount of water droplet injection in the experiment. The experiment used five vane wheel sensors to measure the flow velocities. Still, the measurement range of $\pm 0.5\ m/s$ meant that the sensors gave intermittent outputs due to the prevailing low gas velocities. Hence, the CFD model's flow field prediction could not be sufficiently verified with the experimental data.

The gas temperature transients complement the argument that the water droplet injection is one of the crucial factors causing the gap between the simulation and experiments (Fig. 4.42). At height levels 7.0 m, 7.7 m, and 8.4 m—sensors DTF70H07, DTF77H07, and DTF84H07, respectively—the simulation predicts an increase in gas temperature during the primary injection (up to 500 s). Contrary to this, the experiments show lower gas temperatures, which can only be explained due to the heat absorbed by the evaporation of injected water droplets. The simulation also over-predict the gas temperature increase due to the compression effect at height levels below the injector (DTF63M00, DTF42M00, CTF28M00, and BTF16M00). Also, the equilibrium temperature after the completion of gas mixing is lower in the experiment

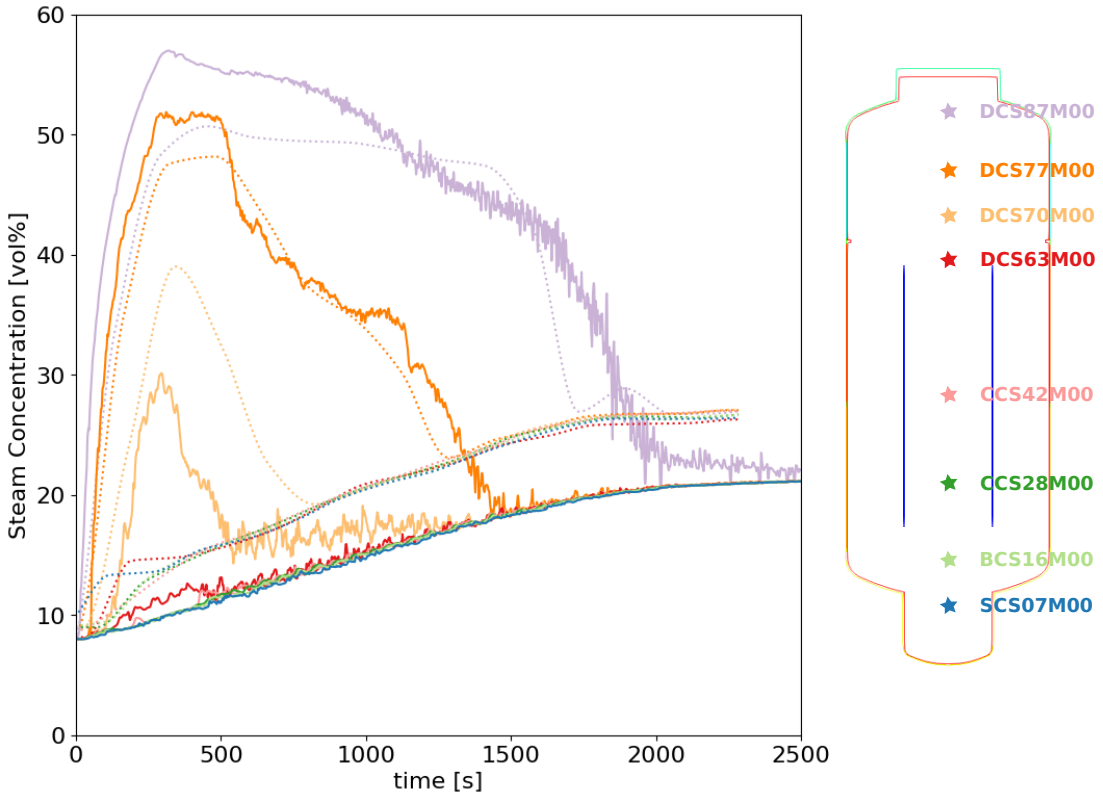

Figure 4.41: THAI-TH24: Comparison of the steam concentration transients between experiment (dotted lines) and simulation (solid lines) at different heights along the centerline.

(92 °C) compared to the simulations (94 °C).

The steam mass condensing on the cooled wall is described in Figure. 4.43. The simulation is able to predict the experiment's trend of higher condensation rates (slope of the curve) during the primary injection phase (up to 500 s), followed by lower condensation rates as the erosion phase progresses. The difference in condensation rates at different times can be explained with the temperatures of the cooled wall (Fig. 4.36. The high condensation rates until 500 s causes the wall temperatures to increase due to latent heat of condensation. Because of the temperature increase, the steam saturation pressure at different locations on the wall also increase, thereby restricting condensation. Though the simulation may appear to over-predict the total mass of condensate formed, this is not a model deficiency. In the experiment, the draining water is measured at regular intervals. Still, there will always be a film on the cooled wall due to surface tension, which cannot be accounted for in the cumulative condensate mass. But the wall condensation model is a single-phase approach, where there is no water film formation on the cold walls. Instead, the entire amount of steam to liquid water

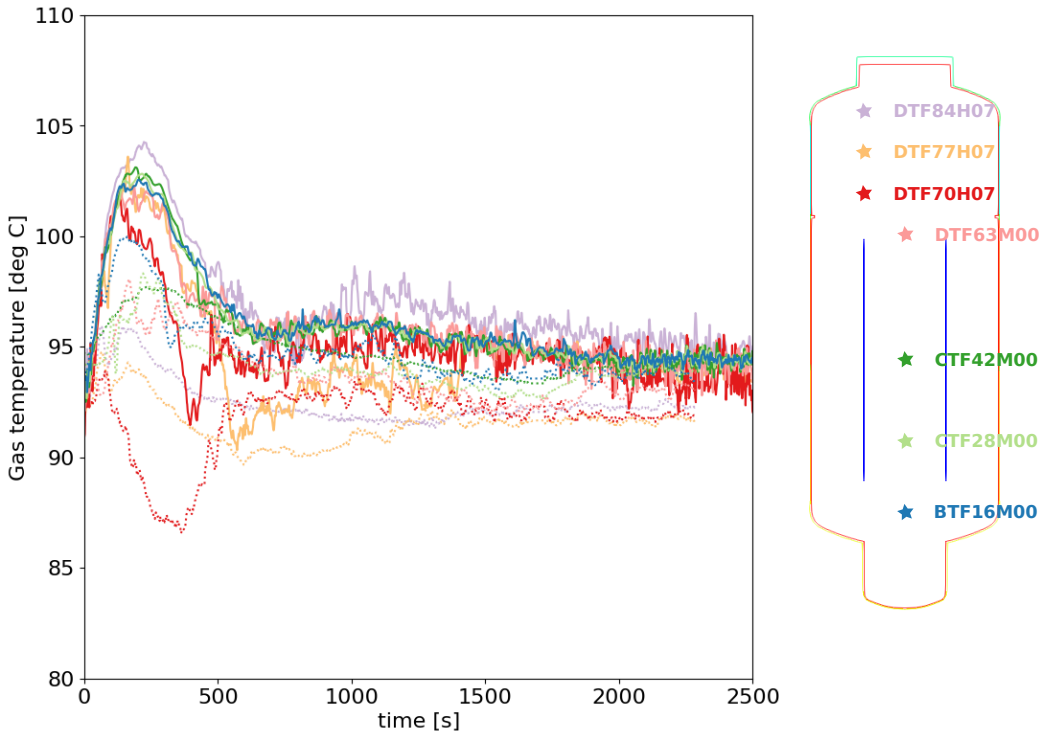

Figure 4.42: THAI-TH24: Comparison of the gas temperature transients between experiment (dotted lines) and simulation (solid lines) at different heights along the centerline.

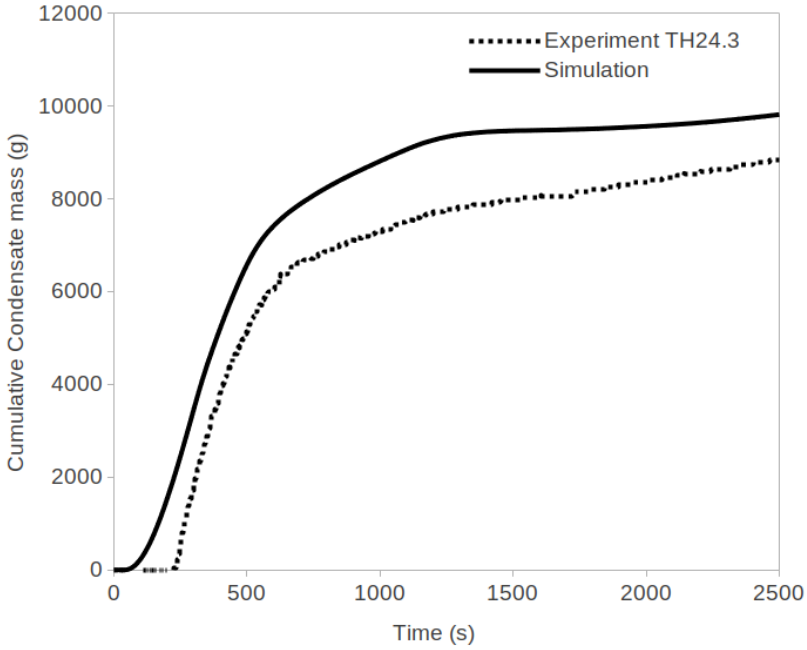

Figure 4.43: THAI-TH24: Comparison of the cumulative steam condensate mass between experiment and simulation.

conversion is considered in the cumulative condensate mass.

Overall, the simulation results reasonably agree with the experimental data for pressure, steam concentration, and gas temperature transients. Though a part of the gap between the simulation results and experimental data may be attributed to the modeling choices, e.g., turbulence with the u-RANS model, the unquantified water droplet injection (along with steam) resulted in changes to the pressure, steam concentration, and temperature levels. Moreover, the *Face-flux* wall condensation model has proven to capture the steam condensation on the 'upper cooled' wall with commendable accuracy—indicated through condensate mass and wall temperatures.

4.6 PARTICLE GROWTH AT DIFFERENT RELATIVE HUMIDITIES

In the event of a severe nuclear accident, the key factor determining the containment aerosol concentration is the evolution of particle size distribution with time. Larger sized aerosols settle at a faster rate under gravity whereas the smaller sized particles remain in the atmosphere for a longer time. Particle size distribution is primarily influenced by coagulation and steam condensation on aerosols (Allelein *et al.*, 2009). The work done in the present thesis is limited to modeling the particle growth due to steam condensation. The following hygroscopic species are released into the containment (Jokiniemi, 1990): CsOH, Cs_2CO_3, Cs_2Te, Cs_2TeO_3, CsI, RbI, SrI_2, BaI_2, $Sr(OH)_2$, $Ba(OH)_2$ (fission products); CdI_2, H_3BO_3, $CsBO_2$, $Cs_2B_4O_7$ (control rod materials); NaOH, Na_2CO_3, KOH, K_2CO_3 (concrete constituents). When exposed to a humid environment, an hygroscopic aerosol particle absorbs water and grows in size until the partial pressure of water vapor on it surface is equal to the partial pressure of water vapor in the gas atmosphere. The ratio of the diameter corresponding to this equilibrium condition to the initial particle diameter is defined as the growth ratio. Mishra *et al.* (2019) experimentally studied the hygroscopic growth of CsOH and CsI aerosols and reported their growth ratios at different relative humidities. The CFD model for hygroscopic aerosol growth described in section 3.2.3.3 is validated against this experimental data.

4.6.1 CFD simulation

The objective of the CFD simulations is to compute the growth ratio of CsI and CsOH aerosol particles at different relative humidities. One simulation corresponds to one particular relative humidity for one aerosol material. The computational domain is a single control-volume of 1 m^3. The initial diameter of the particle is 0.1 $\mu\mathrm{m}$ and the particle number concentration is 10^6 m^{-3}. The pressure (1 atm) and temperature (25 $^{\circ}\mathrm{C}$) are constant for all the simulations. The mass fractions of the gas (air and steam) and dispersed (CsI or CsOH) phases are computed from RH and the particle number concentration. Due to steam condensation on hygroscopic aerosol particles, the mass fraction of steam in the gas phase reduces, thereby changing the relative humidity as the particle grows. The domain size, initial diameter, and the number concentration are selected such that the net steam condensation is minimal and the relative humidity remains almost constant for a simulation. The *Log-normal model* is employed for capturing the evolution of diameter change. The equilibrium diameter of an aerosol material is reached within 1-10 s of physical time. Compared to this, the

transients of an actual containment flow is in the order of hours and days. Therefore, the time evolution of the particle diameter is inconsequential and only the equilibrium diameter at a particular RH influences the gravitational settling of particles. Time-step sensitivity analysis with CsOH aerosol at 90% RH revealed that the equilibrium diameter is insensitive to time-step size for time-steps less than 0.1 s. The results reported in the current work, corresponds to simulations with time-step of 0.01 s.

Material	Molecular weight ($\mathrm{kg\,kmol^{-1}}$)	Density ($\mathrm{kg\,m^{-3}}$)	van't Hoff factor
NaOH	40.0	2130	2.0
CsOH	149.9	3680	2.0
CsI	259.8	4510	1.72
Ag	107.9	10500	-

Table 4.5: Material properties of aerosols

4.6.2 Discussion of Results

4.6.2.1 Hygroscopic growth of CsI aerosols

From the experimental data (Mishra *et al.*, 2019), it is clear that CsI material's growth ratio at a particular RH value depends on the RH history, i.e., whether the RH is increased or decreased (Fig. 4.44). When the RH is increased, the particle starts absorbing water from the atmosphere at a particular RH called as the deliquescence relative humidity (DRH) (Jokiniemi, 1990). When the RH is reduced, the particle recrystallizes from the solution way below the deliquescence point called as the effervescence relative humidity (ERH). From the figure 4.44, it can be inferred that DRH for CsI material is around 90% whereas ERH is 55%. This differential behavior of CsI aerosol in the simulations is captured by either imposing or not imposing the solubility limit (Eq. 3.57). The maximum solubility of CsI in water at 25 $^{\circ}\mathrm{C}$ is 862.5 $\mathrm{g\,L^{-1}}$. In a real application, the relative humidity in a containment varies with time. Therefore, the solubility limit has to imposed if the RH is increasing and turned off if the RH is reducing. Overall, the CFD model accurately captures the hygroscopic growth of CsI aerosols at different RH values. But there is no deterministic way available to predict the effervescence relative humidity, when the RH is reducing. However, the growth ratio (1.2) computed by the model around the ERH is very minimal and does not enhance the gravitational settling of aerosol particles significantly.

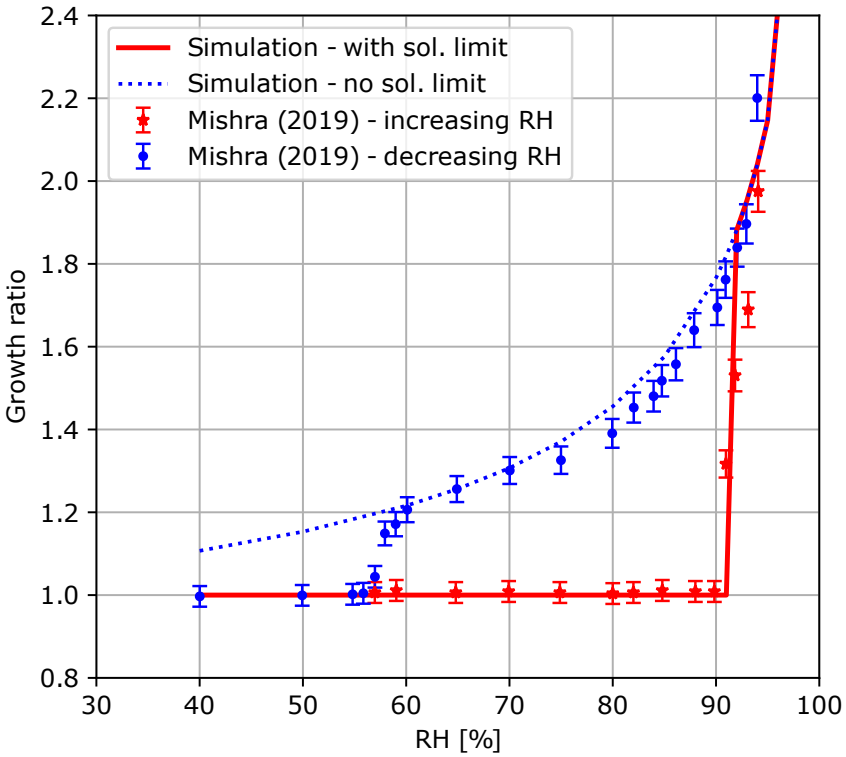

Figure 4.44: Growth ratio of CsI aerosols at different relative humidities.

4.6.2.2 Hygroscopic growth of CsOH aerosols

Unlike CsI aerosol material, CsOH aerosols readily form an aqeous solution and start to absorb water at even low relative humidities (Mishra *et al.*, 2019). Therefore, the solubility limit is not imposed in the simulations for CsOH aerosols. The growth ratios of CsOH aerosols predicted by the CFD simulations are in reasonable agreement with the experimental data (Fig. 4.45). The gap between the simulation results and experimental data at high humidities (RH > 80%) is due to the choice of the simplified hygroscopic model described in Jokiniemi (1990). In the same work, Jokiniemi (1990) has provided formulations for sophisticated hygroscopic models with better accuracy but significantly increased computational cost. Since one of the objectives of the present CFD model is computational efficiency, the deficiencies occurring due to model simplifications is accepted for the moment, as long as the CFD model gives a reasonable estimate.

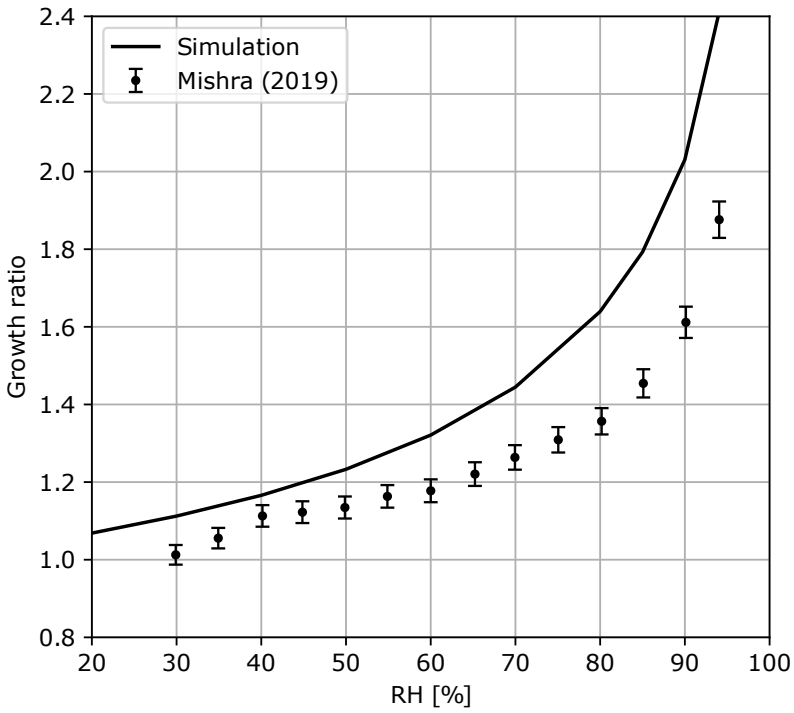

Figure 4.45: Growth ratio of CsOH aerosols at different relative humidities.

4.7 AHMED EXPERIMENTS

Aerosol depletion in humid containment atmospheres have been previously studied at large scale experimental facilities, e.g., LACE (Volume = 852 m^3) and DEMONA/VANAM (Volume = 640 m^3) (Mäkynen *et al.*, 1997). But these experiments had non-homogeneous thermal hydraulic conditions—pressure, temperature, and relative humidity. Such large scale integral experiments cannot be used to validate aerosol models. Therefore, experiments in small scale facilities are necessary to accurately control the thermal hydraulic conditions. PITEAS (Volume = 2.9 m^3) and AHMED (Volume = 1.81 m^3) are small scale experiments on aerosol depletion in humid atmospheres with very good control on thermal hydraulic conditions. But the PITEAS experiments used only the hygroscopic CsI as the aerosol material whereas the AHMED experiments used multiple hygroscopic (NaOH, CsI, and CsOH) and inert (Ag) aerosol materials (Mäkynen *et al.* (1997)). Therefore, the AHMED experiments allows for a more comprehensive validation and hence used in the present work.

4.7.1 Experimental Details

The AHMED facility was constructed by VTT (Technical Research Centre of Finland) to study the gravitational settling rates of hygroscopic and non-hygroscopic aerosols at different thermal-hydraulic conditions. The AHMED vessel is a cylindrical geometry with a vessel radius of 63.5 , height of 142.5 and a total volume of 1.81 m^3. The gas temperatures were measured with Pt100-type resistance type detectors (accuracy of $\pm$ 2°C) at 13 different locations to ensure the homogeneity of the temperature field. Relative humidity was measured with three Vaisala Humicap detectors (accuracy of $\pm$ 2%). Aerosol number and mass concentrations were continuously measured with a condensation nucleus counter (CNC) and tapered element oscillation microbalance (TEOM) systems. The aerosol size distribution, thermal hydraulic conditions, and the initial aerosol mass concentration for different AHMED experiments considered for CFD model validation in the present work are given in Table 4.6.

Material	Size distribution		RH (%)	Temperature (°C)	Initial mass concentration ($\mathrm{mg\,m^{-3}}$)
	AMMD (μm)	GSD			
Ag	2.7	1.7	54	22	79
NaOH	2.4	1.6	22	50	112
			34	20	200
			82	27	208
			91	17	638
			96	23	218
CsOH	2.1	1.7	7	51	89
			33	19	86
			97	28	94
CsI	2.3	1.7	27	23	102
			82	24	98
			96.5	27	94

Table 4.6: Details of AHMED experiments for Ag, NaOH, CsOH, and CsI aerosols

4.7.2 CFD simulations

In the AHMED experiments, because of the uniform thermal-hydraulic conditions (RH, temperature, and pressure) throughout one experiment, the particle size distribution (PSD) changes only at the start of the experiment and the gravitational settling of aerosols happen at this size distribution. The *Log-normal* model is used to compute the particle size distribution after hygroscopic growth at a particular relative humidity. The aerosol depletion rate is maximum at the beginning since the larger sized particles

settle faster, leaving only smaller sized aerosols in the atmosphere. The *Log-normal* computes the drift-velocity at one representative diameter for the entire size distribution and therefore cannot capture this differential settling rates of aerosols of different sizes. The *sectional* model is capable of computing the differential settling rates by solving a number concentration equation for each section. One section corresponds to aerosols of a particular mass (or diameter). Moreover, the objective of comparison with AHMED experiments is to validate the drift-flux model. Consequently, the *sectional* model is used to model the gravitational settling. The following assumptions are made:

- The gas flow is assumed to be frozen with zero velocity. In the AHMED experiments, a weak natural circulation flow was present due to temperature difference between the aerosol sampling systems and the gas ($\sim 0.5\ ^{\circ}\mathrm{C}$). This natural circulation flow cannot be modeled in the simulation and hence the flow field is assumed to be frozen.
- The weak natural circulation flow in the experiments, made the aerosol concentration homogeneous at a given time. But in the CFD simulations, as the aerosols settle under gravity their mass concentration is not homogeneous, i.e., top part will have comparatively less concentration when compared to the bottom part. Therefore, a volume averaged mass concentration is computed for the CFD simulations and compared with the experimental data.
- Particle size distribution changes only due to hygroscopic growth and not due to coalescence or deagglomeration.
- Since gravitational settling of aerosol particles is a one-dimensional phenomenon, a one-dimensional computational domain with an height of 142.5 cm is employed.

The initial PSD is log-normal with an AMMD and a GSD, as given in Table 4.6. After the hygroscopic growth, the particle size distribution is still log-normal with the same GSD but with a different AMMD. This log-normal distribution of the particle size is distributed into finite sections for computing the gravitational settling with the *sectional* model. Sectional sensitivity analyses indicate that 32 mass sections, distributed on the logarithmic scale, are sufficient. Time-step sensitivity studies confirm that a time step of 0.1 s provides necessary accuracy. The sensitivity studies are omitted for the conciseness of the thesis.

4.7.3 Discussion of results

4.7.3.1 Non-hygroscopic aerosols

Silver (Ag) being a non-hygroscopic material, do not absorb steam. The aerosols settle under gravity with their initial size distribution intact. The simulation results are in excellent agreement with the AHMED experimental data (Fig. 4.46).

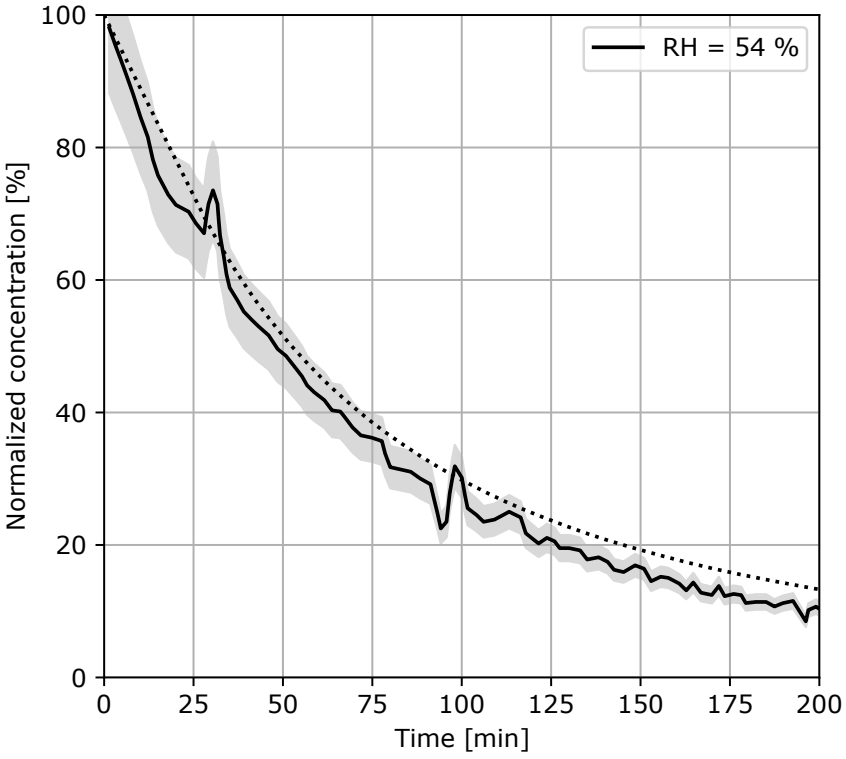

Figure 4.46: Comparison of experimentally measured Ag aerosol mass concentration transients (solid lines) with the simulation results (dotted lines) at RH = 54% (indicated by color). Experimental uncertainity of $\pm 10\%$ is indicated with the grey shading.

4.7.3.2 Hygroscopic-aerosols

The gravitational settling of hygroscopic aerosols is computed in two steps. Firstly, the hygroscopic growth is computed with *Log-normal* model, followed by the gravitational settling using the *sectional* model. The *Log-normal* model takes computes the equilibrium diameter for a given aerosol material, initial size distribution, and thermal-hydraulic conditions as given in Table 4.6. The initial 'count mean diamter' (d_{cm}) is computed from the AMMD and GSD for a particular aerosol provided in the AHMED

experiments. Table 4.7 reports the equilibrium count mean diameter and growth ratio for NaOH, CsOH, and CsI aerosols at different relative humidities. Based on the equilibrium or wet count mean diameter and GSD, the particle number concentration is distributed into 32 mass sections for computing the gravitational settling with the *sectional* model.

Aerosol material	Relative humidity (%)	Equilibrium d_{cm} (µm)	Growth ratio
NaOH (Initial d_{cm} = 0.95 µm)	22	1.03	1.09
	34	1.12	1.18
	82	1.80	1.91
	91	2.21	2.34
	96	2.28	2.40
CsOH (Initial d_{cm} = 0.54 µm)	7	0.55	1.02
	33	0.61	1.13
	97	1.43	2.65
CsI (Initial d_{cm} = 0.54 µm)	27	0.54	1.0
	82	0.54	1.0
	96.5	1.23	2.30

Table 4.7: Growth ratio of different aerosol materials at different relative humidities computed by the CFD model

When RH increases, hygroscopic aerosol particles exhibit enhanced gravitational settling due to their increase in size. For NaOH aerosols, the transients of aerosol concentration obtained from the simulation have good agreement with the experimental data at high RH values (> 80%) (Fig. 4.47). Eventhough the simulation results capture the trend of aerosol depletion at low RH values (22% and 34%), they do not capture the enhanced difference in depletion rates at these two RH values. Part of the reason may be the simplified model for the computation of water activity (section 3.2.3.3). Jokiniemi (1990) describes two models for computation of water activity of hygroscopic material: A simplified model valid at high RH values and a sophisticated model valid at all RH values. The present work utilizes the simplified model, which is deficient when the salts form concentrated solution in water at low RH values. Since the gravitational settling is enhanced only at high RH values (> 90%) and the model errors at low RH values are acceptable. Especially, the sophisticated model for water activity increases the computational burden.

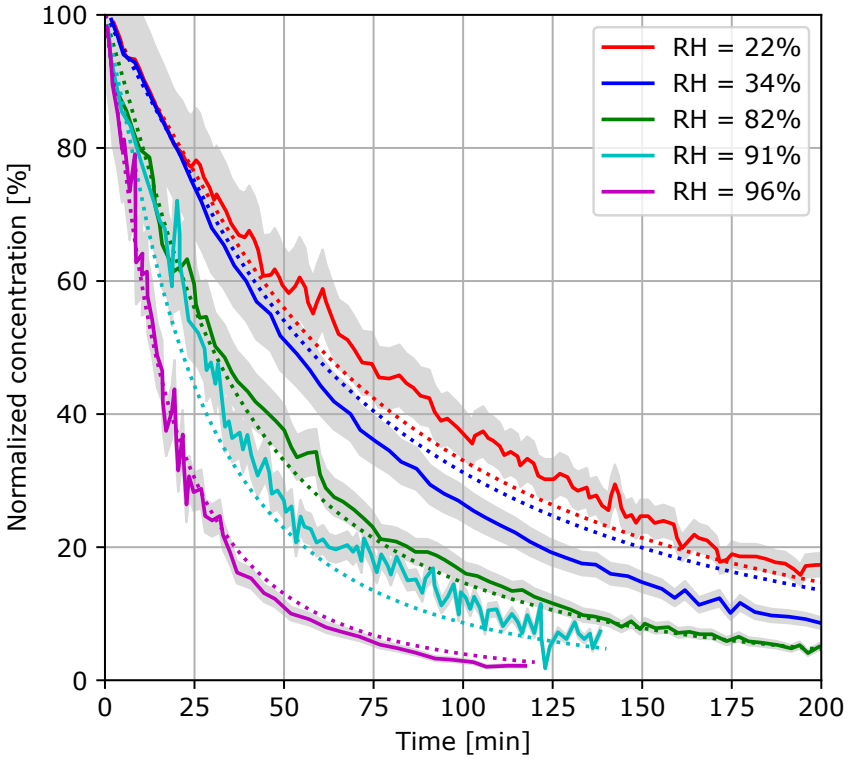

Figure 4.47: Comparison of experimentally measured NaOH aerosol concentration transients (solid lines) with the simulation results (dotted lines) at different relative humidities (indicated by color). Experimental uncertainity of $\pm 10\%$ is indicated with the grey shading.

For CsOH aerosols, the simulations predict slower depletion of aerosol, especially at low RH values (Fig. 4.48). The gap between the simulation results and experimental data at RH = 7% can be only explained due to error in the initial size distribution specified in the AHMED experiment. At RH = 7%, there is no hygroscopic growth of aerosols and the only phenomenon is the downward motion of aerosol particles under gravity, where no modeling errors are possible. Similar to the NaOH aerosols, the experimental data for CsOH aerosols confirm that there is a enhanced gravitational settling at RH = 33% when compared to RH = 7%. This differential behavior is not captured by the CFD model and can be again attributed to the simplified model for computing water activity. At the high relative humidity of 97%, the CFD model predicts a faster depletion of aerosol concentration in the gas atmosphere when compared to low RH values as expected. The gap between the simulation results and experimental data at this high RH may again be due to the incorrect initial size distribution specified by the experiments.

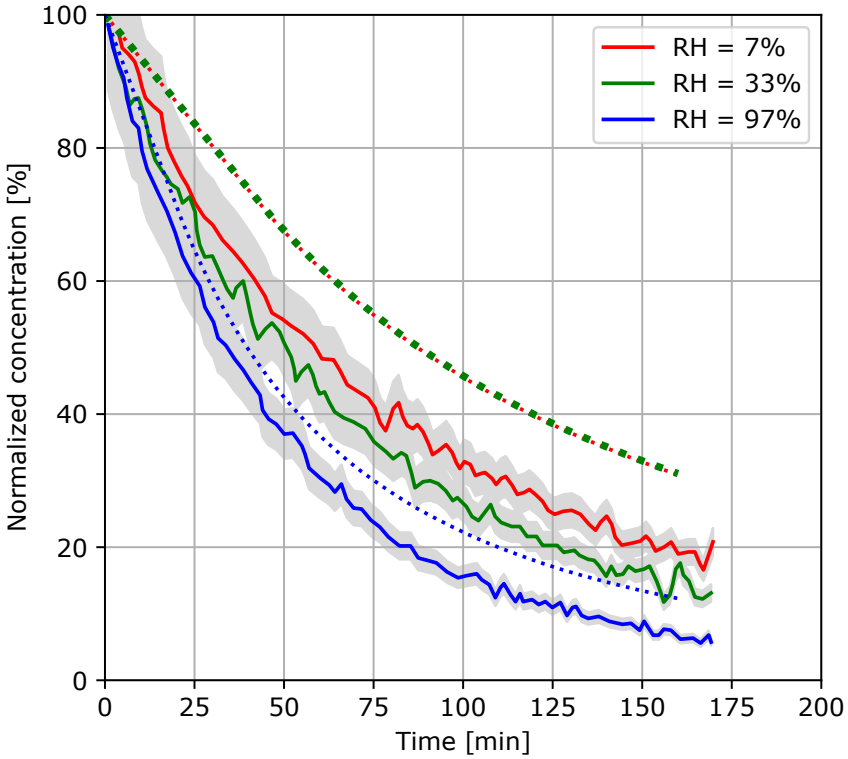

Figure 4.48: Comparison of experimentally measured CsOH aerosol concentration transients (solid lines) with the simulation results (dotted lines) at different relative humidities (indicated by color). Experimental uncertainity of $\pm 10\%$ is indicated with the grey shading.

CsI aerosols have their deliquescence point at RH = 90%, i.e., they start absorbing water only above RH = 90%. The experimental data confirms that the aerosol depletion behavior is nearly the same at 27% and 82% relative humidities (Fig. 4.49). The simulations also exhibit the same behavior on imposing the solubility limit on CsI material. Similar to CsOH aerosols, the simulations predict a slower aerosol depletion at low relative humidities. This gap can only occur if the initial particle size distribution is specified incorrectly in the AHMED experiments. At relative humidity of 96.5%, the CsI aerosols undergo hygroscopic growth and settle faster under gravity. Though the simulations predict the enhanced settling at RH = 96.5%, the gap with the experimental data persists because of the error in the initial size distribution.

In conclusion, the hygroscopic growth model and the drift-flux model to account for particle inertia had a reasonable agreement with the AHMED experimental data. Especially for the hygroscopic NaOH aerosol material, the CFD model predicted aerosol depletion accurately at all relative humidity values. For the non-hygroscopic,

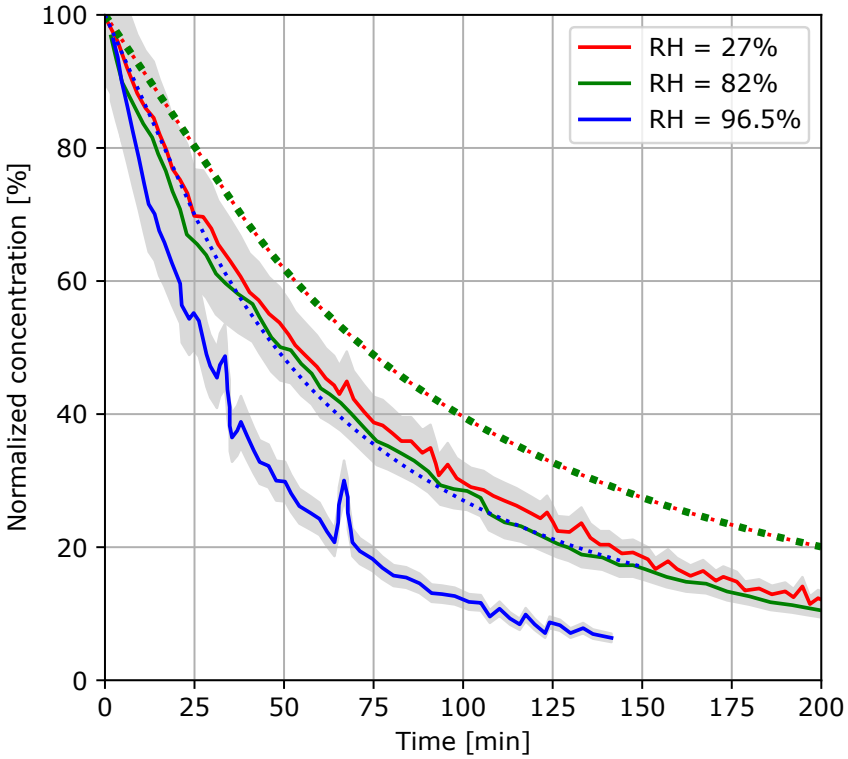

Figure 4.49: Comparison of experimentally measured CsI aerosol concentration transients (solid lines) with the simulation results (dotted lines) at different relative humidities (indicated by color). Experimental uncertainity of $\pm 10\%$ is indicated with the grey shading.

silver aerosol material, the CFD model produced results within the experimental uncertainty. For the CsI aerosol material, the CFD model correctly predicted that the hygroscopic growth only occurs above a relative humidity of 90%. The aerosol depletion rate predicted by the CFD model deviated from the AHMED experimental data for the CsOH aerosol at low relative humidities. In the future, it is recommended to validate the CFD model against multiple experiments for gravitational settling in humid atmospheres to identify the model deficiencies.

4.8 SUMMARY OF THE CFD MODEL VALIDATION

The CFD model was systematically validated against small-scale and technical scale experiments. The DHSC case showed that the CFD model could reasonably predict the turbulent, buoyancy-driven flow field. The validations against the SETCOM experiment revealed that the *Face-flux* wall condensation model could accurately predict steam condensation in the presence of non-condensable gases. Subsequently, simulations of

the THAI experiments (TH21, TH22, and TH24) showed that the CFD model represents the containment typical flow in a technical scale geometry with sufficient accuracy. The validations against the AHMED experiments revealed that the hygroscopic growth and the aerosol gravitational settling are captured correctly by the Mixture model, based on the Euler-Eulerian approach.

CHAPTER 5

Applications

Kampili (2022) studied the impact of aerosol decay heat on buoyancy-driven flows with an Euler-Lagrangian CFD model and concluded that the decay heat influenced the flow field, turbulence levels, and particle deposition. But due to the computational cost of the Lagrangian particle tracking method, only an analysis of the small-scale DIANA facility (L $\sim$ 0.7 m) was feasible. And also, only a single gas species (air) was used in this analysis. Motivated by this work, the current Ph.D. thesis aims to analyze the impact of aerosol decay on buoyancy-driven flows in technical scale geometries. For this purpose, two hypothetical cases are considered based on the experiments in the THAI vessel—TH22 and TH24. In the THAI-TH22-based simulation, the impact of decay heat on the light-gas (helium) erosion process is studied. The steam layer erosion process is studied in the subsequent case based on the THAI-TH24 experiment. Apart from the scale, the physics covered in the above two cases—turbulence, buoyancy-driven flow, multicomponent gas transport, wall condensation, conjugate heat transfer, and radiation heat transfer—are representative of the containment thermal-hydraulics.

The analysis of decay heat effects is followed by applying the CFD model to simulate the VANAM-M3 experiment. The VANAM-M3 experiment conducBatelle Model Containment (BMC) with a free-volume of 626 m^3. VANAM-M3 is a combined effect experiment with containment typical phenomena such as buoyancy-driven flow, multi-compartmented geometry, hygroscopic growth (NaOH), conjugate heat transfer with condensation, convection, and radiation heat transport. The VANAM-M3 simulation is done primarily to demonstrate the CFD solver's ability to run a real large-scale application with multiple interacting phenomena in a computationally efficient manner.

5.1 IMPACT OF DECAY HEAT

5.1.1 CFD Setup

The same simulation settings—initial and boundary conditions, modeling choices—of the THAI-TH22 and THAI-TH24 are applied, except for the additional injection of CsI aerosol particles. The average concentration of aerosol particles in the vessel atmosphere is kept at 1 $\mathrm{g\,m}^{-3}$. Therefore, 60 g of CsI aerosols (corresponding to the THAI vessel volume of 60 m^3) are injected into the upper portion of the THAI

vessel along with helium for the TH22 simulation and steam for the TH24 simulation. The particle size distribution (PSD) of the CsI aerosols is taken from the AHMED experiments: AMMD of 2.3 μm and GSD of 1.7. The density of the CsI material is specified as 4510 $\mathrm{kg\,m^{-3}}$. The decay heat of a nuclear aerosol particle varies with time, but in the current work, a constant decay heat value of 111.57 $\mathrm{kW\,kg^{-1}}$ is used for the CsI aerosol, according to Kampili (2022). In addition to the drag, weight, and buoyancy forces, the thermophoretic force on the aerosol particle accounts for the temperature gradients closer to the walls. Diffusiophoretic force is considered in the TH24 simulation only because of the presence of a condensing wall. Though the TH24 simulation contains a steam-air mixture, the relative humidity is less than 90%, so hygroscopic aerosol growth is considered absent. The objective of the simulation is to assess the impact of decay heat on containment typical flows in a technical scale geometry. Therefore, the discussion of the results is only restricted to the changes in thermal-hydraulic behavior due to aerosol decay heat. Consequently, the deposition of aerosols on containment structures is not analyzed in this work. The aerosols deposited on the structures are considered removed from the computational domain and have no further effects, e.g., heat release to the walls.

5.1.2 THAI-TH22 Results

5.1.2.1 Gas mixing behavior:

Figures 5.1 and 5.2 compare the gas mixing processes in between the THAI-TH22 simulations with and without decay heat effect, through helium concentration and gas temperature contours. In the THAI-TH22 simulation without the aerosol injection, a stably stratified helium layer is established in the upper part of the vessel at the end of the injection phase (time = 226 s). Since the injected helium is colder (T $\sim$ 35-85 $^{\circ}\mathrm{C}$) than the existing gas (T $\sim$ 90 $^{\circ}\mathrm{C}$), it results in a lower temperature in the upper portion of the facility. Therefore, a reduced temperature difference between the gas and the 'upper cooled' wall lowers the gas-wall heat transfer. Consequently, the natural convection flows adjacent to the 'upper cooled' wall are suppressed. Furthermore, the helium injection into the upper part of the THAI vessel compresses the gas below the helium layer, resulting in its temperature rise. Therefore, the temperature differential between the heated walls (T = 120 $^{\circ}\mathrm{C}$) and the gas reduces, leading to reduced heat transfer and buoyancy-driven flows adjacent to the heated walls. The stability of the helium layer stratification depends on the competing buoyancy forces generated from helium mass concentration gradients and the temperature gradients. Eventually, at the

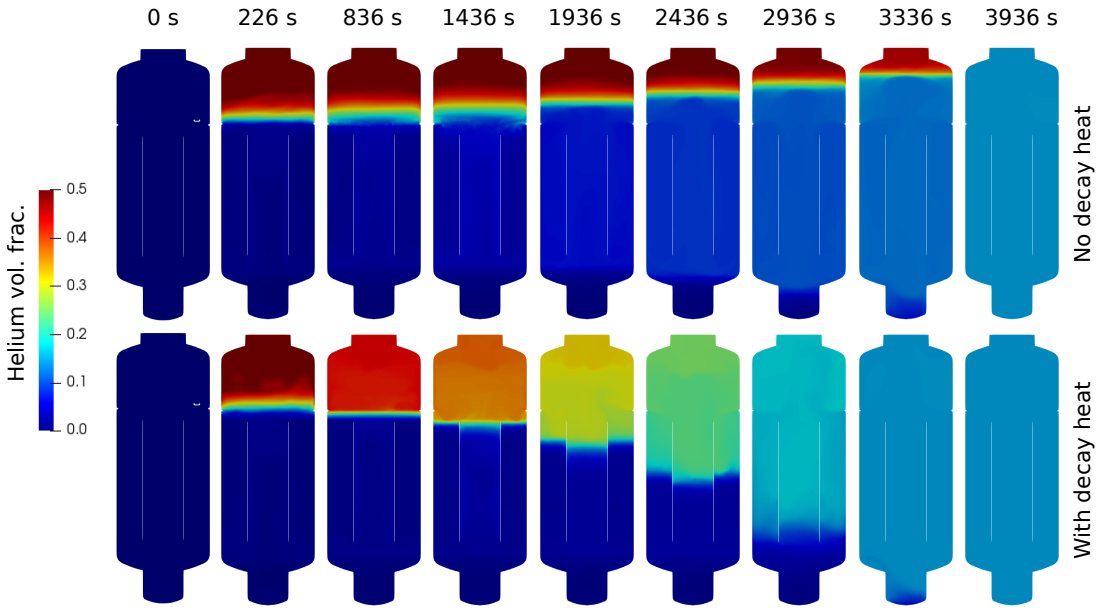

Figure 5.1: Transients of helium concentration contours for the fundamental THAI-TH22 simulation without aerosol injection (top) vs. the THAI-TH22 simulation with CsI aerosol particles carrying decay heat (bottom).

helium-air diffusion layer, the buoyancy effects due to temperature gradients overwhelm the mass concentration gradients leading to the onset of instabilities (time = 836 s). The instabilities get stronger by time = 1436 s. The helium-air interface moves up, uncovering part of the 'upper cooled' wall (time = 1936 s). The uncovered part of the 'upper cooled' wall causes downward flow, which meets the rising flow adjacent to the heated walls, resulting in partial recovery of the initial natural circulation flow. The helium layer is eroded, and the helium-air interface moves up further, resulting in the uncovering of further portions of the 'upper cooled' wall (time = 2436 s, 2936 s, 3336 s). Subsequently, this results in homogenization of the helium layer with the return of initial natural circulation flow around 3936 s.

For the THAI-TH22 simulations with the decay heat effect, the aerosol particles are injected along with the helium gas into the upper plenum of the THAI vessel. The expected behavior is that the decay heat of aerosols results in increased gas temperature, which further reduces the density in the upper part of the THAI vessel and hence a more stable stratification. But the decay heat also results in local buoyancy forces, which enhances the gas mixing in the helium-rich upper region. This phenomenon is visible as early as the end of the injection phase in the gas temperature contour (Fig. 5.2, time = 226 s): A rising flow is visible from the helium-air interface into the upper plenum of the vessel. Also, the increased gas temperatures imply a larger temperature difference

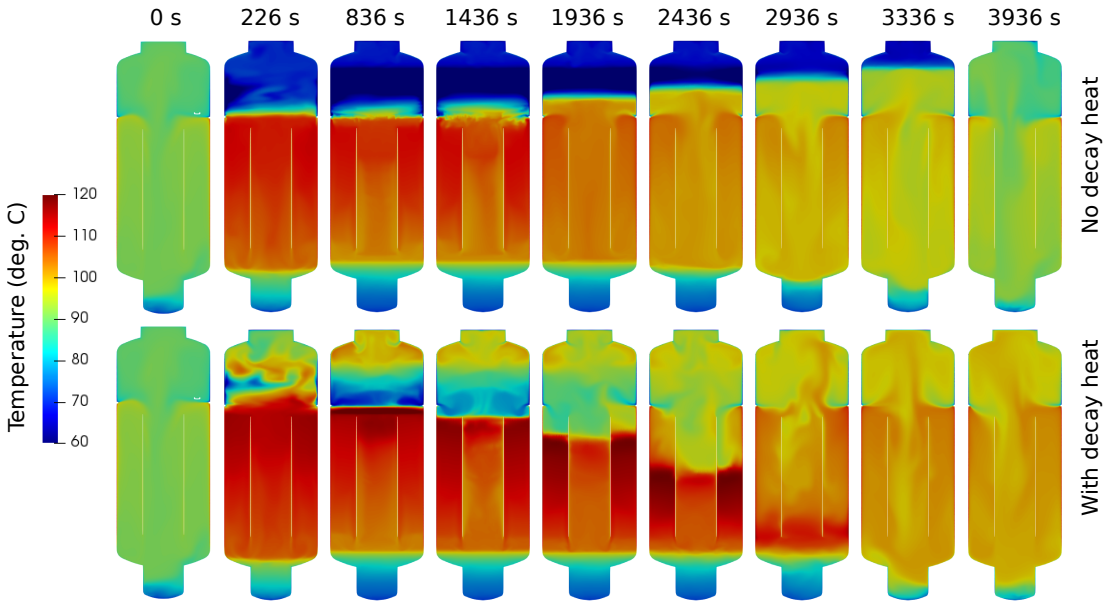

Figure 5.2: Transients of gas temperature contours for the fundamental THAI-TH22 simulation without aerosol injection (top) vs. the THAI-TH22 simulation with CsI aerosol particles carrying decay heat (bottom).

with the 'upper cooled' wall ($\sim$ 40 °C), resulting in increased natural circulation flow closer to the cooled wall. By time = 836 s, the helium concentration in the upper portion of the facility has homogenized, and the wall-gas heat transfer becomes the dominant mechanism. From the temperature contours (Fig. 5.2, time = 836 s), it is clear that the temperature difference between vessel's lid (T $\sim$ 61 °C) and the electrically heated curved section (T $\sim$ 75 °C) results in minor convective loops between these sections. The downward flow, adjacent to the 'upper cooled' wall, encounters the lower edge of the helium layer and results in gas mixing due to inertial forces, further moving the helium-air interface downwards. By time = 1936 s, the helium layer has moved down sufficiently to uncover some part of the actively heated 'middle heated' wall. Also, the gas temperature in these uncovered regions has reduced, enhancing the temperature difference with the 'middle heated' wall (which is at 120 °C). This increased temperature differential results in a rising flow closer to the 'middle heated' wall, which meets the dropping flow nearer to the 'upper cooled' wall leading to enhanced gas mixing. As the bottom edge of the helium layer moves further down, more portions of the actively heated walls are uncovered (time = 2436 and 2936 s). The helium concentration becomes uniform throughout the THAI vessel by time = 3336 s with the complete recovery of the initial natural circulation flow field.

A quantitative comparison of the helium erosion process between the simulations with

and without aerosol decay heat is given in Figure 5.3. In the simulation without the decay heat effect, the helium erosion process is a slow, diffusion-dominant phenomenon for a major part of the transients, followed by the rapid drop of the helium concentration due to convective mixing once the natural circulation flow is reestablished (refer sensor location DCH84B005). For the simulation with aerosol injection, the gas mixing in the top part of the facility is at a faster rate immediately after the end of the injection phase (226 s). From the contour plots (Fig. 5.1), the lower edge of the helium layer moves downwards. This behavior can be inferred from the quantitative plot also: The homogenization at 7.0 m (DCH70F005), 6.3 m (CCH63B005), 4.2 m (CCH42B005), 2.8 m (CCH28B005), 1.6 m (BCH16B005), and 0.7 m (SCH07B005) happens at time = 500 s, time = 1500 s, time = 2500 s, time = 2900 s, time = 3000 s, and time = 3300 s respectively.

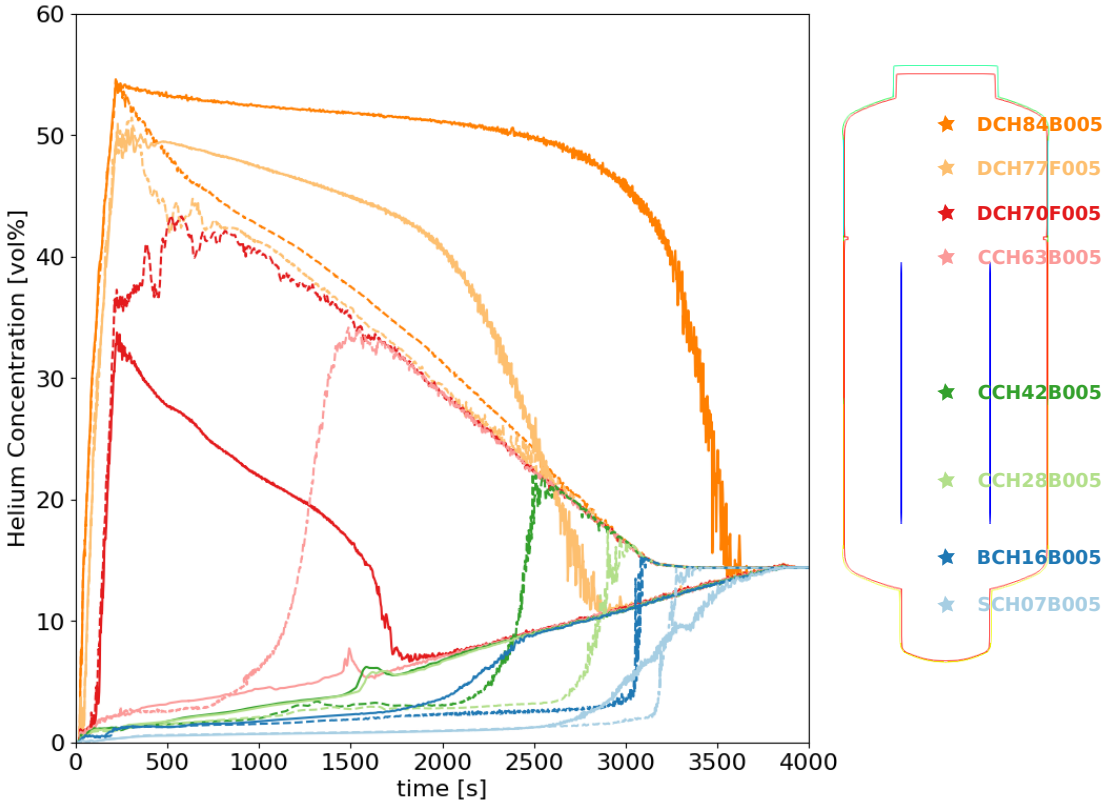

Figure 5.3: Transients of helium concentration profiles for the fundamental THAI-TH22 simulation without aerosol injection (solid lines) vs. the THAI-TH22 simulation with CsI aerosol particles carrying decay heat (dashed lines).

Apart from the difference in mixing times—3900s without aerosol decay heat vs. 3300s with decay heat—the mixing mechanism is being affected due to the consideration of

aerosol decay heat. For the simulation with decay heat, the local gas mixing in the upper part (helium-rich zone) homogenizes the helium concentration in that region. The helium-air interface moves downwards, resulting in the re-establishment of the initial natural circulation flow. But without the decay heat, the initial process is dominated by molecular diffusion, which reduces the gas concentration gradients at the helium-air interface. The helium-air interface moves upwards, resulting in the re-establishment of the initial flow field.

5.1.2.2 Pressure and Temperature

The aerosol decay heat leads to an increase in the average gas temperature of approximately 7 °C and a corresponding increase in pressure of about 0.03 bar (Fig. 5.4). Though there is a continuous release of heat to the gas phase as long as the aerosol particle exists in the atmosphere, a corresponding linear rise in pressure is absent. The actively cooled wall—'upper cooled' maintained at 40 °C—removes the excess heat, thus, limiting the continuous pressurization of the facility.

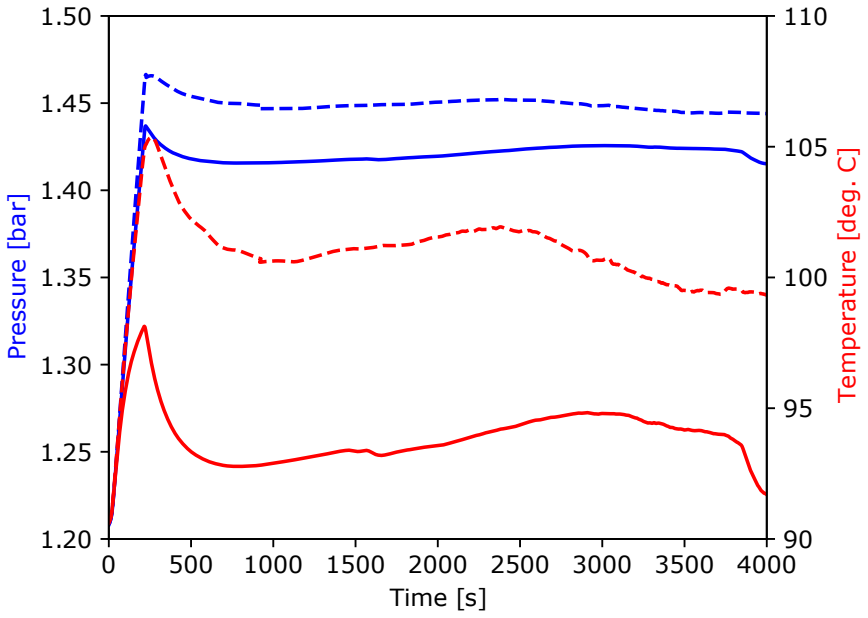

Figure 5.4: Transients of pressure (blue) and volume-averaged gas temperature profiles (red) for the fundamental THAI-TH22 simulation without aerosol injection (solid lines) vs. the THAI-TH22 simulation with CsI aerosol particles carrying decay heat (dashed lines).

5.1.3 THAI-TH24 Results

5.1.3.1 Gas mixing behavior

Figures 5.5 & 5.6 compares the gas mixing mechanism of the THAI-TH24 simulations with and without decay heat. The aerosol contours are not shown for the simulation with decay heat. Still, for all practical purposes, the aerosol concentration coincides with the steam concentration due to its low drift velocity. The progression of steam layer erosion for the THAI-TH24 simulation without the influence of aerosol decay heat is already discussed in section 4.5.5.3. The steam is injected at temperatures exceeding 100 °C, which is more than the prevailing gas temperature. Hence, the temperatures in the upper part of the THAI facility increase. The gas temperatures below the injector level also increase (> 100 °C) due to gas compression (time = 100 s, 200 s), thereby completely suppressing the existing natural circulation flow. This phenomenon is similar to the simulations with and without aerosol injection. It must be remembered that the temperature scales of the contour plot (Fig. 5.6) are different for the simulations with (scale = 90-120 °C) and without aerosol decay heat (scale = 90-100 °C), and hence they are not directly comparable. By 500 s, the steam injection is almost complete, except for the compensating injection to account for the steam condensing on the cooled wall. Around this time, due to the active cooling of the 'upper cooled' wall, the gas temperature in the upper part of the vessel starts to reduce for the simulation without the decay heat. But since the aerosols injected along with steam release decay heat, the gas temperature is higher for the simulation with the decay heat.

In the lower part of the facility, the heated walls (100 °C) are at a lower temperature than the gas, and hence the gas-wall heat transfer reduces the gas temperature (from time = 200 s to 500 s). This phenomenon is common between the simulation with and without decay heat since the aerosols are not transported to the lower portion of the vessel. For the simulation with the decay heat, the 'upper cooled' wall causes a weak downward flow and carries some steam and aerosols below the injector level (Fig. 5.5, time = 500 s). The aerosols release decay heat, thereby heating the gas phase. The 'middle heated' wall at 100 °C cools the gas in the annular space between the inner-cylinder and the vessel wall. But within the inner-cylinder, the heat generated by the aerosol particles is not removed, and the gas temperature increases (time = 800 s, 1300 s). The higher gas temperature inside the inner-cylinder (top part) causes a reverse flow (towards the steam layer) and prevents the steam concentration from moving downwards (time = 1300 s). In the annular region, the 'middle heated' wall is colder than the gas, causing a

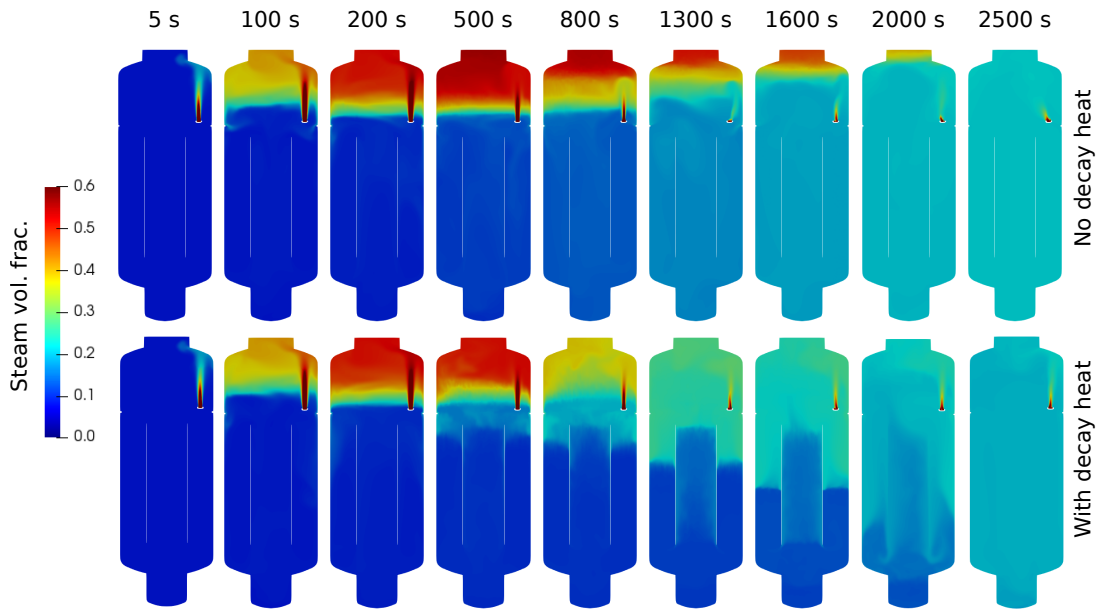

Figure 5.5: Transients of steam concentration contours for the fundamental THAI-TH24 simulation without aerosol injection (top) vs. the THAI-TH24 simulation with CsI aerosol particles carrying decay heat (bottom).

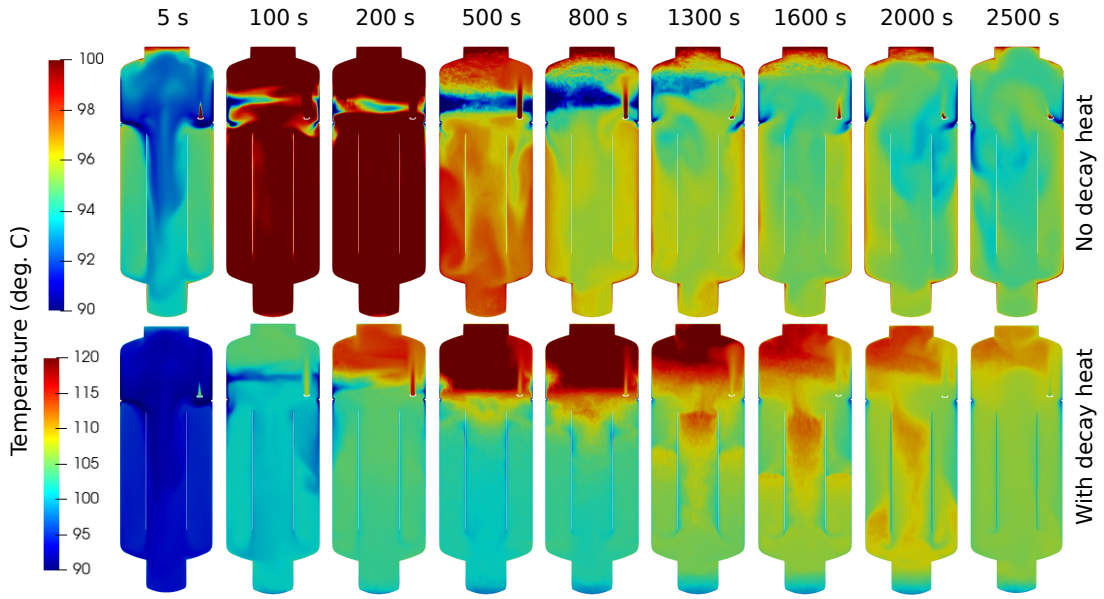

Figure 5.6: Transients of gas temperature contours for the fundamental THAI-TH24 simulation without aerosol injection (top) vs. the THAI-TH24 simulation with CsI aerosol particles carrying decay heat (bottom).

downward flow adjacent to it. This bulk motion brings the steam layer downwards. The differential concentration of steam within the inner-cylinder and in the annular space is visible (time = 1300 s and 1600 s). By time = 2000 s, the gas mixing phenomenon is almost complete for the simulation without decay heat effect, whereas the steam

concentration is still inhomogeneous for the simulation with decay heat. Only by time = 2500 s, the steam is uniformly distributed.

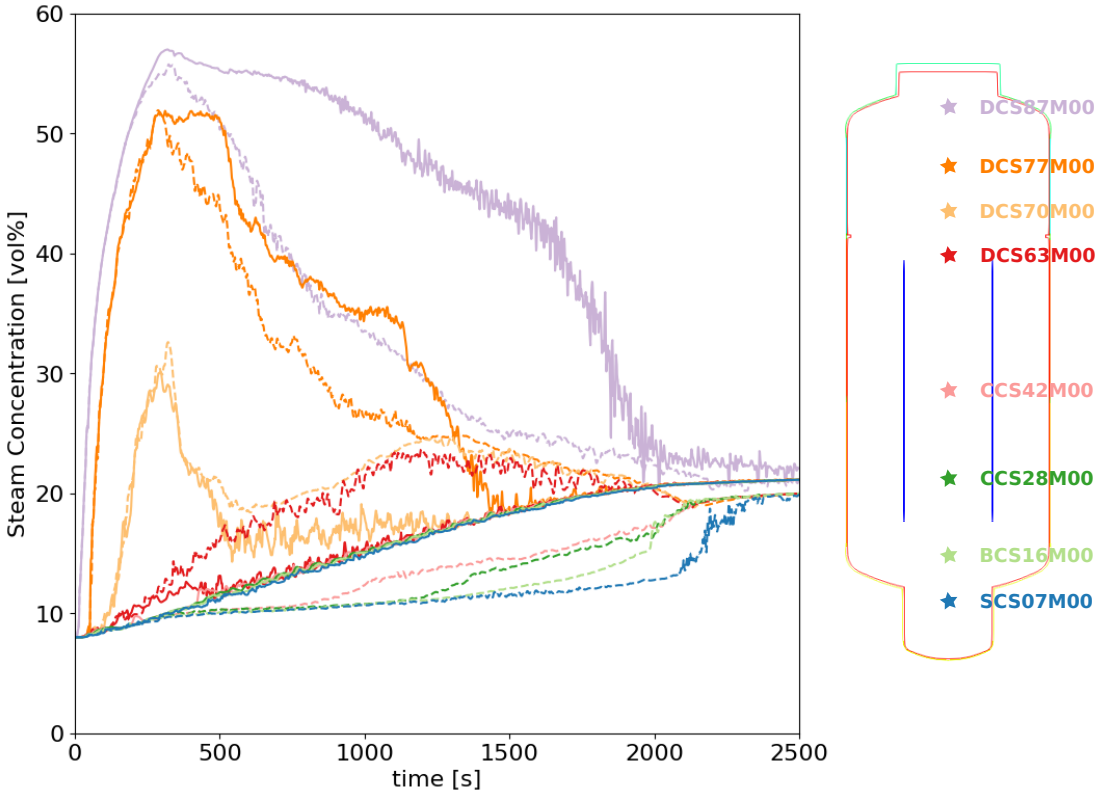

Figure 5.7: Transients of steam concentration profiles for the fundamental THAI-TH24 simulation without aerosol injection (solid lines) vs. the THAI-TH24 simulation with CsI aerosol particles carrying decay heat (dashed lines).

The quantitative comparison of steam concentration profiles for the simulations with and without aerosol decay heat also reveals the difference in the gas mixing mechanism (Fig. 5.7). The steam-air interface moves upwards for the fundamental TH24 simulation without aerosol injection. During the injection phase (up to time = 500 s), the steam levels continue to rise very slowly in the lower part of the facility (probes SCS07M00, BCS16M00, CCS28M00, and CCS42M00). In this period, the locations in the facility's top part show a rapid steam concentration increase, as expected. After 500s, the concentrations in the top part of the facility start to drop, indicating the onset of steam layer erosion. First, the steam concentration at level 6.3 m (DCS63M00) becomes uniform with the rest of the location in the lower part of the vessel at around time = 500 s. Subsequently, the steam concentration at other places in the upper part of the vessel becomes homogeneous with those in the locations below: level 7.0 m

(DCS70M00) at time = 1400 s, level 7.7 m (DCS77M00) at 1500 s, and level 8.7 m (DCS87M00) at 2000 s. But for the simulation with aerosol injection, the bottom part of the vessel (CCS42M00, CCS28M00, CCS28M00, BCS16M00, and SCS07M00) are entirely separated from the top part of the facility until 2000 s. The steam concentration in the top part of the facility becomes almost homogeneous by time = 1500 s, but the gas mixing with the lower part of the facility happens only by time = 2400 s.

5.1.3.2 Pressure and Temperature

Throughout the injection and erosion phases, the decay heat clearly enhances the gas pressure and temperature (Fig. 5.8). After the gas mixing is complete (time = 2500), the gas temperature in the simulation with decay heat is 12 °C higher than the fundamental THAI-TH24 simulation without aerosols . Similar to the THAI-TH22 simulations with the aerosol injection, a linear pressure rise (or gas temperature rise) corresponding to the continuous heat release of the aerosols is absent. This is because most of the vessel walls are maintained at temperatures below 100 °C, hence the gas-wall heat transfer limits the continuous pressurization.

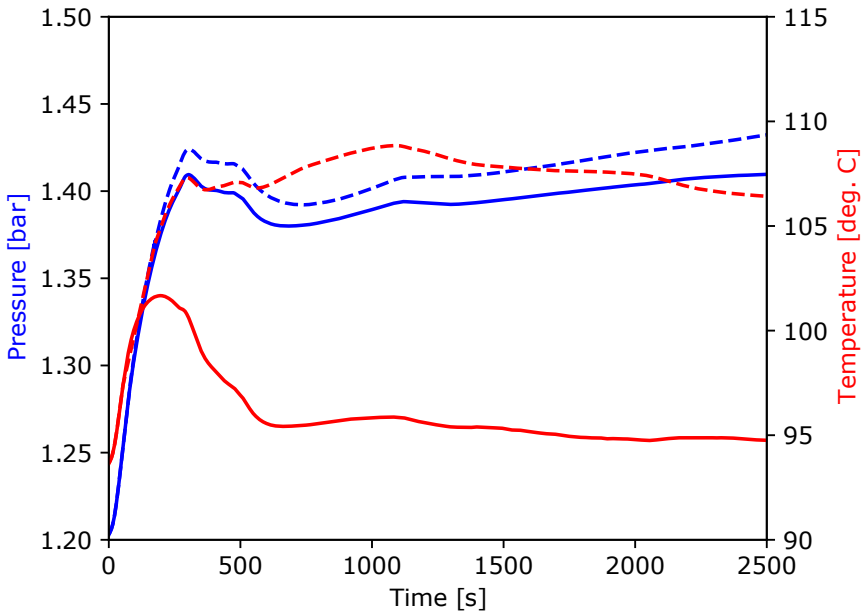

Figure 5.8: Transients of pressure (blue) and volume-averaged gas temperature profiles (red) for the fundamental THAI-TH24 simulation without aerosol injection (solid lines) vs. the THAI-TH24 simulation with CsI aerosol particles carrying decay heat (dashed lines).

5.1.3.3 Wall condensation

Figure 5.9 compares the cumulative mass of steam condensed on the cylindrical sections adjacent to the 'uppper cooled' wall. Until the first 300 s of the steam injection phase, there is no visible difference in the rate of wall condenstion (slopes of the curves). After time = 300 s, the amount of condensate formed is higher for the simulation with aerosol injection, indicating a higher rate of condensation. The enhanced condensation for the simulation with aerosol decay heat can also be inferred from the temperature transients of the 'upper cooled' wall (Fig. 5.10). The slope of the temperature curves indicate a higher rate of condensation (phase change heat transfer). The higher rate of condensation for the simulation with aerosol decay heat can be attributed to the slow gas mixing process, which results in higher steam concentration in the upper part of the facility—region close to the condensing 'upper cooled' wall. After about time = 1000 s, the cumulative condensate mass becomes steady for both the simulations, indicating infinitesimal condensation. This is again indicated by the drop in wall temperatures (Fig. 5.10).

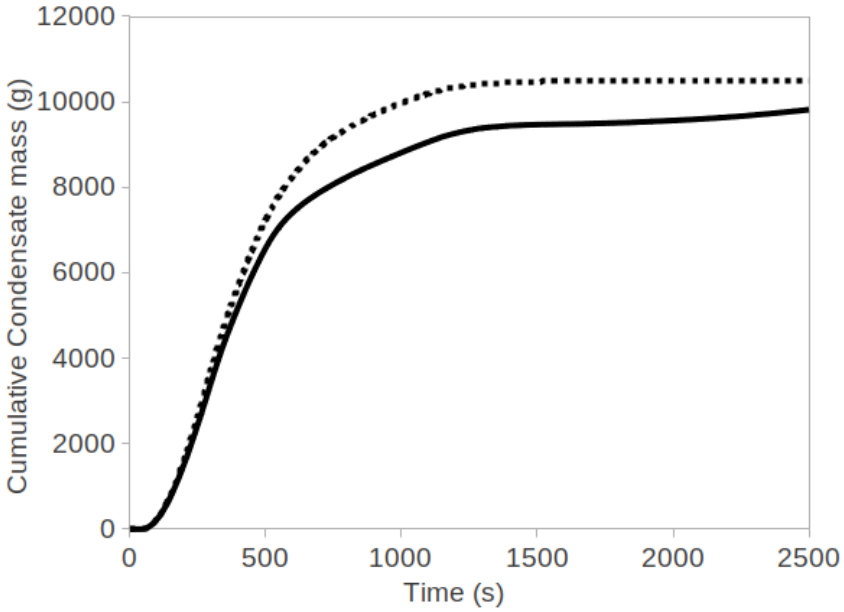

Figure 5.9: Transients of the cumulative condensate mass for the fundamental THAI-TH24 simulation without aerosol injection (solid lines) vs. the THAI-TH24 simulation with CsI aerosol particles carrying decay heat (dotted lines).

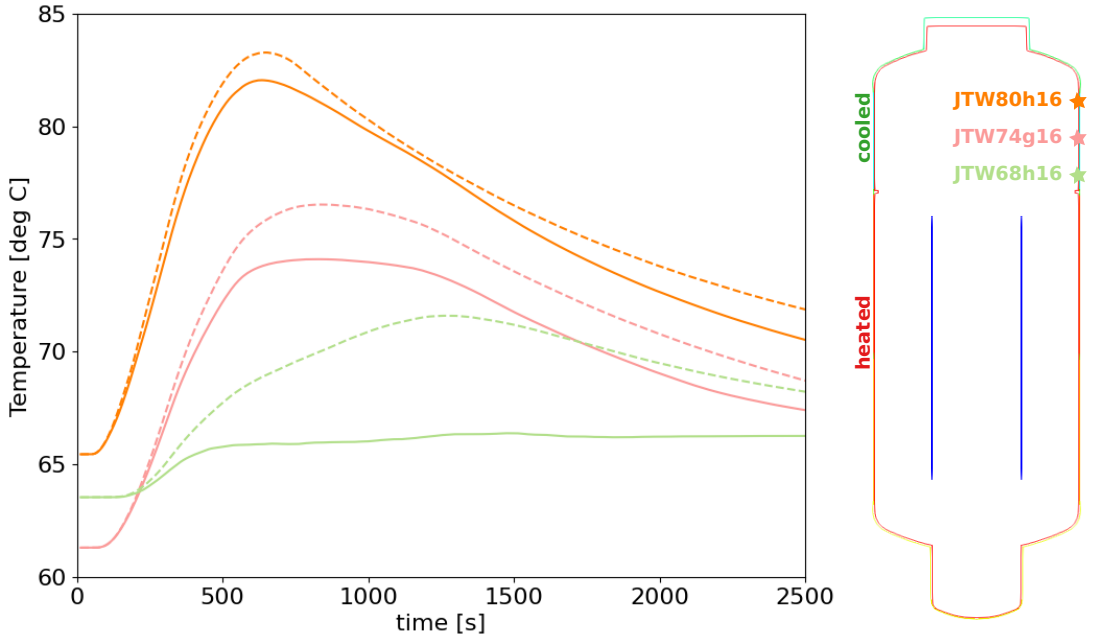

Figure 5.10: Transients of the 'upper cooled' wall temperatures at different heights for the fundamental THAI-TH24 simulation without aerosol injection (solid lines) vs. the THAI-TH24 simulation with CsI aerosol particles carrying decay heat (dashed lines).

5.1.4 Summary of the THAI decay heat simulations

From the THAI-TH22 and THAI-TH24 simulations with aerosol injection, it is conclusive that the aerosol decay heat significantly influences thermal-hydraulic behavior. The increased pressure and gas temperature levels are on the expected lines. But the gas mixing behavior is affected differently for the TH22 simulation with helium injection and the TH24 simulation with steam injection. Since the aerosols are injected into the upper part of the vessel, the expected behavior was a more stable stratification due to the decay heat release. But the decay heat enhanced the local gas mixing in the upper part of the THAI facility and subsequently a faster erosion for the TH22 simulation. For the TH24 simulation, the decay heat slowed the gas mixing, resulting in increased steam condensation on the 'upper cooled' wall. The containment thermal-hydraulic behavior is significantly affected due to the aerosol decay heat. In the future, it is recommended to do more simulations with different aerosol concentration levels and relative humidities to understand the effect in detail.

5.2 VANAM

5.2.1 The VANAM M3 Experiment

5.2.1.1 Experimental Setup in the Batelle Model Containment

The VANAM test series was conducted in the Batelle Model Containment (BMC) in Germany in the 1990s (Kanzleiter, 1995). Four tests were conducted with different aerosol materials to study the depletion behavior of aerosol concentration in a large-scale multi-compartment building under dry and humid conditions. Among the four tests, the VANAM M3 experiment was selected as International Standard Problem No. 37 (ISP37) to assess the status of system code modeling concerning hygroscopic aerosol transport and gas distribution in a multi-compartmented geometry. Battelle Eschborn performed the experiment and was financially sponsored by the German Ministry for Education, Science, Research, and Technology (Grant No. 1500803). VANAM M3 is a combined effect experiment with containment typical phenomena such as local gas stratifications, gas transport and mixing by natural circulation, and gas-wall conjugate heat transfer—condensation, convection, radiation (Firnhaber *et al.*, 1996). Hygroscopic sodium hydroxide (NaOH) was used as a model material in place of the containment aerosol cesium hydroxide (CsOH).

The BMC has 626 m^3 and consists of nine compartments (rooms) with various gas mixture compositions, gas velocities, and thermodynamic conditions during an experimental transient. Figure 5.11 illustrates the facility design and the compartment definitions. R5, R6, R7, and R8 represent the upper and lower steam generator compartments, while the containment dome and annular compartments are grouped in R9. The remaining compartments are the reactor cavity (R3), the reactor room (R1), and the central compartment (R2). R4 is a dead-end compartment with walls surrounding it, except for the visible opening. The primary flow path of the gas mixture injected into the upper steam generator room R5 is depicted by steam concentration contours in the right-hand side image of Figure 5.11. The preferred flow path is through the overflow opening of R5 to the dome, while a doorway partially blocks the passage to R7. As long as there is no injection into the reactor cavity (R3), the weak flow in the lower compartments is primarily driven by gas-wall heat transfer and local density differences.

In contrast to most other containment test facilities, the BMC is a concrete building

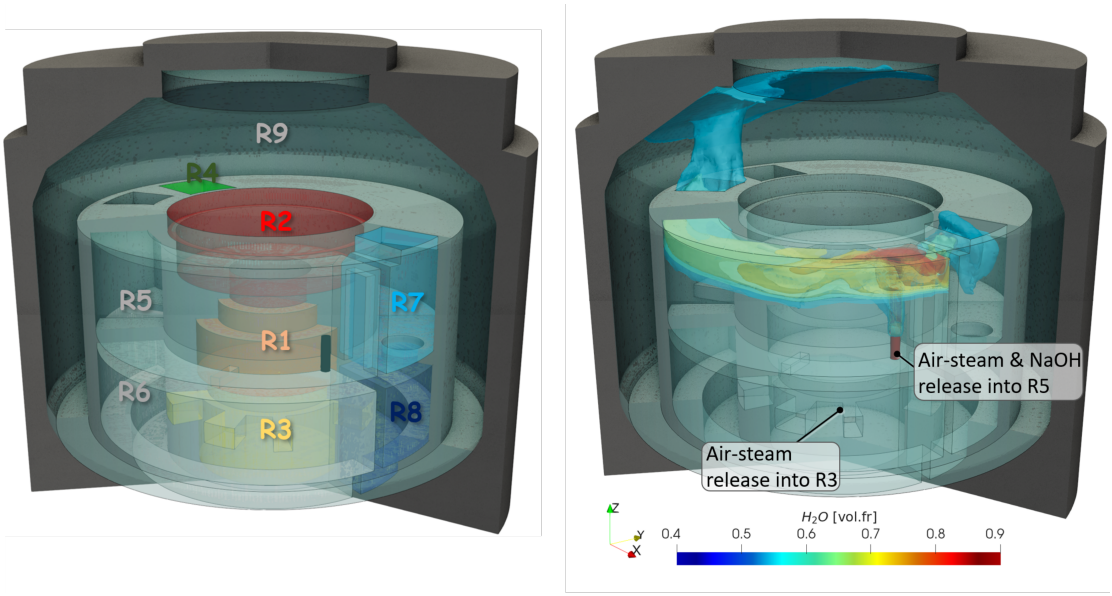

Figure 5.11: VANAM: Geometry of the Batelle Model Containment (BMC) with the different compartments/rooms (left) and the locations of gas/aerosol injection, and the gas flow path showing interconnections between rooms (right).

with no steel liner. Thus, when operated under pressure, there is an inevitable gas leakage to the environment. It could not be localized, but at least there was an attempt to quantify the mass loss rate through a tracer gas concentration measurement. Modeling this leakage in the CFD simulation is a significant challenge.

5.2.1.2 Experimental procedure

The VANAM M3 experiment was conducted with a comparable test sequence to the previous test M2*, except that the water-soluble NaOH aerosol material was used in place of the insoluble SnO2 used in M2* (Kanzleiter, 1993). Hygroscopic NaOH aerosol particles absorb the steam from the atmosphere and grow in size even in sub-saturated conditions (RH < 100 %), resulting in enhanced gravitational settling. The experiment comprises of two aerosol injection and depletion phases to quantify this effect. The first aerosol injection and depletion phases (phases 2 & 3) consider a sub-saturated atmosphere with limited hygroscopic growth. Phases 4-6 address supersaturated conditions (RH > 100%) to have more pronounced aerosol particle growth and thus an enhanced aerosol depletion. The experimental sequence is summarized in Table 5.1.

During the pre-conditioning phase, steam is injected into R5 to heat up the facility.

Phase	Time (s)	Description
Phase 1 (pre-conditioning)	-57850 – 0	Steam injection into R5; Air extraction from R9 annular compartment (1 – 3 h) and backfeeding (13 – 14 h) with reduced steam injection to R3.
Phase 2 (1st aerosol injection)	0 – 3700	NaOH injection into R5 along with steam-air mixture.
Phase 3 (dry aerosol depletion)	3700 – 19800	No injections.
Phase 4 (2nd aerosol injection)	19800 – 21380	NaOH injection into R5 along with steam-air mixture.
Phase 5 (wet aerosol depletion)	21380 – 29000	Gas mixing and aerosol depletion in a humid atmosphere caused by steam injection into R3.
Phase 6 (continued wet depletion)	29000 – 46080	Continued wet aerosol depletion with steam injection into R5.

Table 5.1: VANAM: Experimental sequence

The steam injection will lead to the pressure rise in the facility and consequently gas leak because of the containment design (due to concrete wall without steel liners). Therefore, the facility pressurization was limited by removing about 200 kg of air from the annular portion of the R9 compartment and feeding it back to R3 at the end of the pre-conditioning phase. Figure 5.12 compares the pressure evolution during the different phases with the estimated non-condensable gas (air) mass and the estimated integral leak rate. The continuous leakage is visible by reducing air mass in the stagnant depletion phases 3, 5, and 6. The leak rate was estimated from tracer gas measurements and did not seem to be pressure-dependent only. The consistent description of the non-condensable gas mass balance and leak rate directly affects the predicted pressure of the facility during the injection/depletion phases, thus, posing a considerable uncertainty to the CFD model's setup and assessment of its results.

5.2.1.3 Instrumentation and Experimental Data

The instrumentation of the VANAM M3 test was designed for system code validation and is relatively sparse for a CFD code's validation. Nonetheless, the experiment provides several unique features, particularly its concrete multi-compartment design, which makes it an interesting application-oriented assessment of the CFD model. In total, the measurement concept comprises two pressure transducers (1-6 bar, ±0.02 bar), 54 thermocouples (TC) in the gas phase (0-240 °C, ±1.4 K), and 27 TC inside

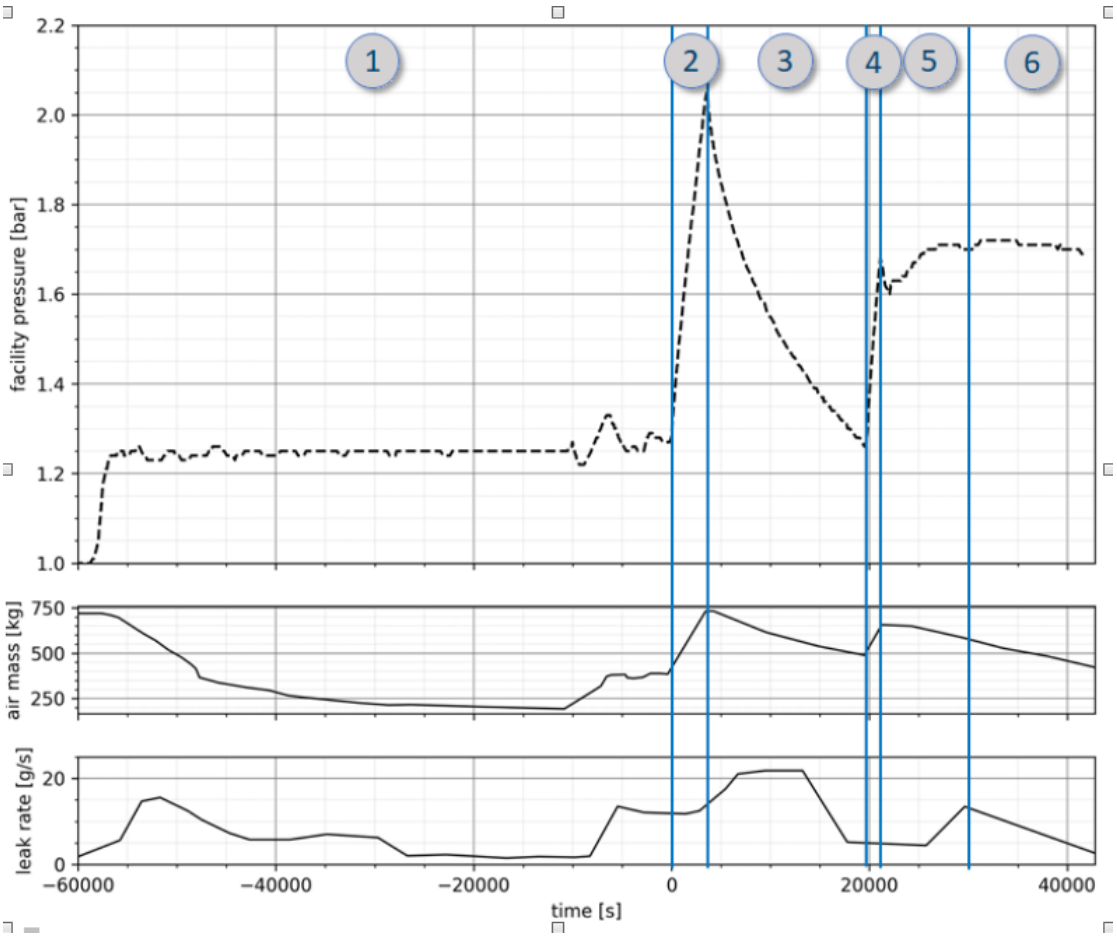

Figure 5.12: VANAM: Pressure evolution and mass balance of the gas during the different phases of the experiment.

the structures (0-240 °C, ±1.4 K) and seven TC in the sump regions near the bottom of the compartments (0-240 °C, ±1.4 K). Additionally, seven capacitive humidity sensors (0-100%, ±10%) are installed. Fourteen vane wheels (0.15-10 m/s, ±0.15 m/s) were installed in the apertures to characterize the flow between the compartments. At six filter stations, the airborne NaOH concentrations are measured discontinuously (for every 5000s).

The major limitation on the use of the experimental data results from the fact that it had to be digitized from available reports (Firnhaber *et al.*, 1996; Kanzleiter, 1995, 1993). The number of sensor histories that could be used for the CFD code's assessment is limited by the amount of data reported in the literature. Also, not all the reported data could be extracted due to the poor clarity of the black and white plots. Furthermore, due to the wide range of the time axis scale (up to 18 h – 64800 s), a considerable uncertainty of at least ±100 s is introduced during digitization, which may become

significant, especially for defining the injection boundary conditions.

5.2.2 CFD simulation

5.2.2.1 Assessment Strategy

Though the experiment is not a well-posed validation case, it offers a unique possibility to assess the CFD model on heat and mass transport processes under conditions close to a severe accident scenario. Consequently, an accurate representation of the measurement is not expected, but a qualitative agreement, i.e., a representation of the observed trends, is sought. Within the frame of this thesis, only the first aerosol injection and depletion phases (2 and 3) are considered with a total duration of $\sim$ 18000 s (5 h).

The primary quantities for the assessment of the thermo-fluid dynamic processes and the water/steam balance are the measured pressure and temperature (gas and structures). Due to the thermal inertia of the concrete material, even continuous wall condensation does not lead to visible changes in the structure temperatures during phases 2 and 3. Due to the formation and evaporation of fog, the steam concentration in the bulk flow remains mostly at saturation conditions, i.e., besides a confirmation, no further conclusions can be drawn from humidity measurements. The transport processes are primarily characterized based on the evolutions of gas temperatures and NaOH concentrations. At the same time, the flow velocities are too low ($< 0.25\ \mathrm{m\,s^{-1}}$) to be detected by the vane wheel sensors.

5.2.2.2 Geometry and Mesh

The 3D geometry was built based on the 2D layouts found in the experimental reports (Firnhaber *et al.*, 1996; Kanzleiter, 1995, 1993). While the large structures were relatively well dimensioned, the information was lacking for the openings and channels which connect the central compartments (R2 and R3) to the steam generator compartments (R5-R8). As a consequence, their position and cross-section could only be guessed. Furthermore, the documentation mentioned that some openings were closed by plates, but quantitative details were missing. Due to the ambiguity in geometrical information, these connections were removed entirely from the 3D geometry and may influence the simulation results.

In contrast to previous validation work, a manually constructed block-structured mesh was hardly feasible for the complex multi-compartmented geometry. Instead, a mesh

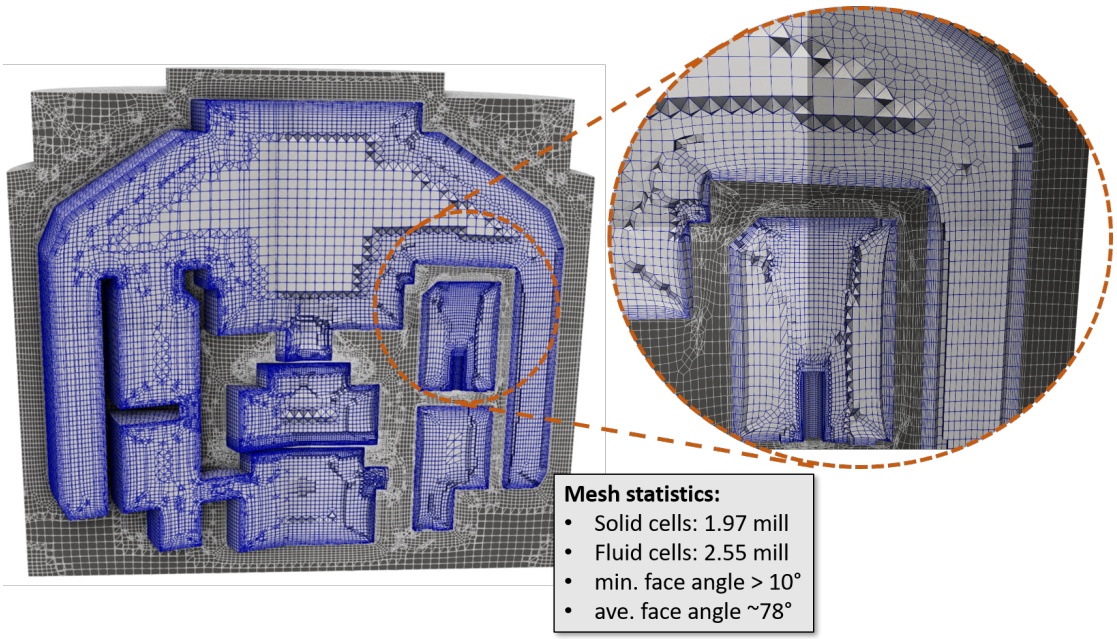

Figure 5.13: VANAM: Sectional view of the hex-dominant mesh with mesh quality statistics.

is automatically generated using the commercial mesh generating toolbox 'cfMesh+.' Figure 5.13 depicts a cut section of the mesh. It employs a cartesian base mesh in the bulk regions with an edge length of 0.2 m, which is refined in two steps (0.1 and 0.05 m) towards the boundaries. Furthermore, the zoom detail illustrates the boundary layer mesh (10 layers) on both sides of the fluid-solid interface.

Generally, a good mesh quality is achieved, satisfying the criteria defined in the established "Best Practice Guidelines" (BPG) (Mahaffey, 2015). However, a few severely non-orthogonal cells with sharp face angles of >10° remained. A formal mesh sensitivity analysis was not conducted in the scope of this paper and is considered infeasible due to the significant computational effort required for the complex 3D flows with long transients. Nevertheless, in the future, the grid sensitivity must be evaluated to identify under-resolved regions and further improve the mesh.

5.2.2.3 Physical models

Aerosol transport is modeled using an Eulerian mixture model (Manninen *et al.*, 1996) along with a drift-flux approach (Frederix *et al.*, 2017). The drift-flux accounts for the forces on the particle due to drag, gravity, thermophoresis, and diffusiophoresis. A significant challenge is modeling the concrete containment's leak rate. As the leak position(s) at the outer wall could not be localized, a volumetric mass sink is considered

for the annular (lower R9) and dome (upper R9) compartment volume. This approach corresponds to a previous system code analysis (Firnhaber *et al.*, 1996). The transient mass loss rate is described according to the experimental estimate (Figure 5.12 bottom), while its composition is according to the local mixture. The major uncertainty in this approach is whether the facility's non-condensable (air) mass remains consistent with the experiment, which, as shown later, affects the pressure transients.

5.2.2.4 Initial and Boundary Conditions

The optimal approach to determine the BMC structure temperature distribution before the aerosol injection and depletion phases 2 to 6 is to simulate the entire facility preconditioning phase (phase 1 $\sim$ 16 hours). However, this was not done due to the substantial computational effort for simulating the long transients. Instead, the initial condition for aerosol injection (phase 2) was approximated by assuming that the concrete surface and gas temperature are close to thermal equilibrium. I.e., the structure temperatures were initialized by mapping the experimentally measured temperatures onto a 7.5 cm thick layer of the corresponding structure. At the same time, the remaining part is defined to be at 295.15 K. Then, the transient heat conduction equation is solved (only for the concrete structures) for 10000 s to get a smooth temperature distribution. The BMC atmosphere is initialized in a two-step approach: First, the measured gas temperatures are mapped for each compartment. As there were insufficient measurements of the steam distribution, the average relative humidity was adjusted to RH = 81% to match the experimentally estimated air mass of approximately 393 kg at t = 60000 s (2000 s before the start of the '1st aerosol injection'). To achieve the expected thermal equilibrium (between the concrete structures and the gas) and to obtain a 3D flow, concentration, and temperature field, the remaining 2000 s of 'phase 1'—steam injection into compartment R5—were simulated. The resulting fields were used as initial conditions for 'phase 2' (Fig. 5.14).

The mass flow rate, gas mixture composition, and temperature of the injection to the upper steam generator R5 were prescribed according to the experimental data extracted from the technical reports (Firnhaber *et al.*, 1996; Kanzleiter, 1995, 1993), which resulted in unavoidable uncertainties in both the injection timing and the injection parameters. Furthermore, estimates had to be made for the aerosol injection. In particular, the aerosol mass flow rate is assumed to be directly proportional to the measured electric current fed to the aerosol generator. The NaOH aerosol's particle size distribution (PSD) was not measured at the inlet but only at the sampling positions

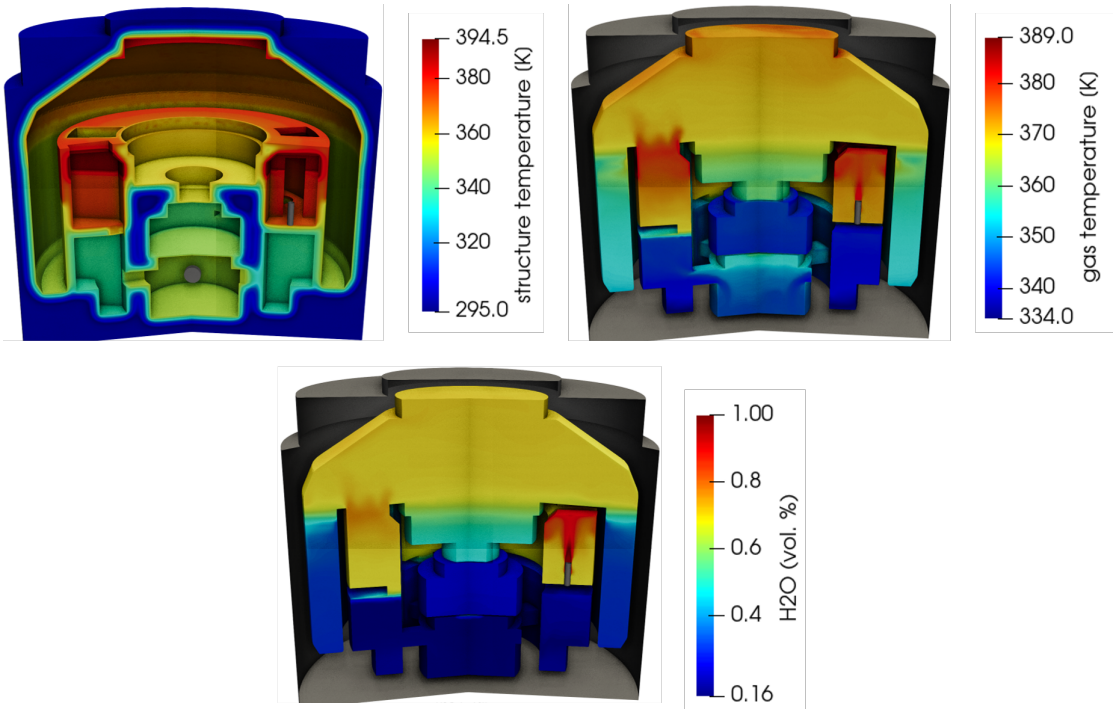

Figure 5.14: VANAM: Temperature and steam distribution estimated as initialization for 'phase 2' (1st aerosol injection).

in R5 at the end of 'phase 2.' The measurement revealed a log-normal distribution for the dry NaOH aerosol with a Mass Median Diameter (MMD) of 0.86 µm and a Geometric Standard Deviation (GSD) of 1.8. In the present work, the humidity in the VANAM facility is at saturation conditions or slightly below saturation. It is assumed that the aerosol particle would have achieved an equilibrium diameter due to hygroscopic growth in these almost constant humidity conditions. Hence, hygroscopic growth of NaOH aerosol is not computed during the simulation transients but is modeled with an equilibrium particle size distribution—MMD of 2.167 µm and GSD of 1.8 corresponding to a relative humidity of 96%. In the equilibrium state, the modeled aerosol consists of 12.47 wt.% NaOH and 87.53 wt.% water have a density of 1067 kg/m³.

5.2.3 Results

The integral facility pressure evolution is the primary reference for assessing the thermo-fluid dynamic processes and the steam-air mass balance. It is compared to the experimental measurement in Figure 5.15 (top). During the injection phase, though the initial pressurization is predicted consistently with the experiment, the peak pressure differs between the simulation and experimental data. After 10000 s, depressurization

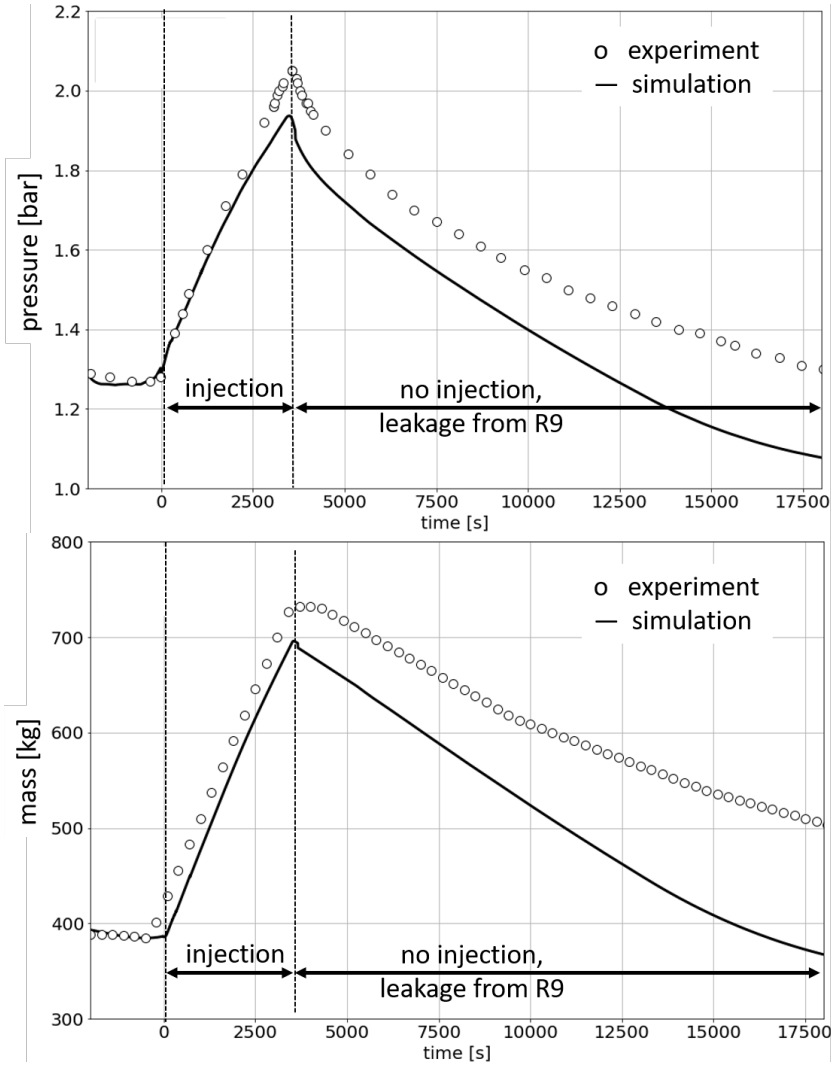

Figure 5.15: VANAM: Transient evolution of pressure and non-condensable gas (air) mass.

occurs slightly faster in the simulation compared to the experiment. The explanation for these observations can be found in the non-condensable gas (air) mass balance (Figure 5.15 bottom). There is an increasing discrepancy after time $\sim$ 2500 s between the air mass estimated by the experimentalists and that predicted by the simulation. This is qualitatively consistent with the one found for pressure evolution. This lower mass of non-condensable gas explains the lower pressure, while there are no indications that throw doubts on the condensation model or the gas-wall heat transfer.

The lower air mass at the end of 'phase 2' results from the prescribed injection air rate's uncertainty. However, the increasing deviation in the depletion phase results from the gas leakage modeling: In the simulation, a uniform gas removal throughout compartment R9 is done to capture the gas leakage through gaps in the concrete

structure. The amount of non-condensable air mass lost in the experiments depends on the local gas composition at the leak locations, which is difficult to model with a uniform volumetric sink term. Characterizing the flow and transport processes inside the multi-compartment geometry is of high interest for code assessment. Even though there were vane wheels installed in the facility, their measurements could not be used due to the low flow velocities (< 0.25 $\mathrm{m\,s^{-1}}$ in the injection phase, < 0.1 $\mathrm{m\,s^{-1}}$ in depletion phase), which were below or near their response threshold of 0.2 $\mathrm{m\,s^{-1}}$. Consequently, the transport processes are implicitly assessed using the gas temperatures and NaOH concentration in the different compartments. Figure 5.16 illustrates the predicted evolution of the gas temperature distribution in both phases. During the

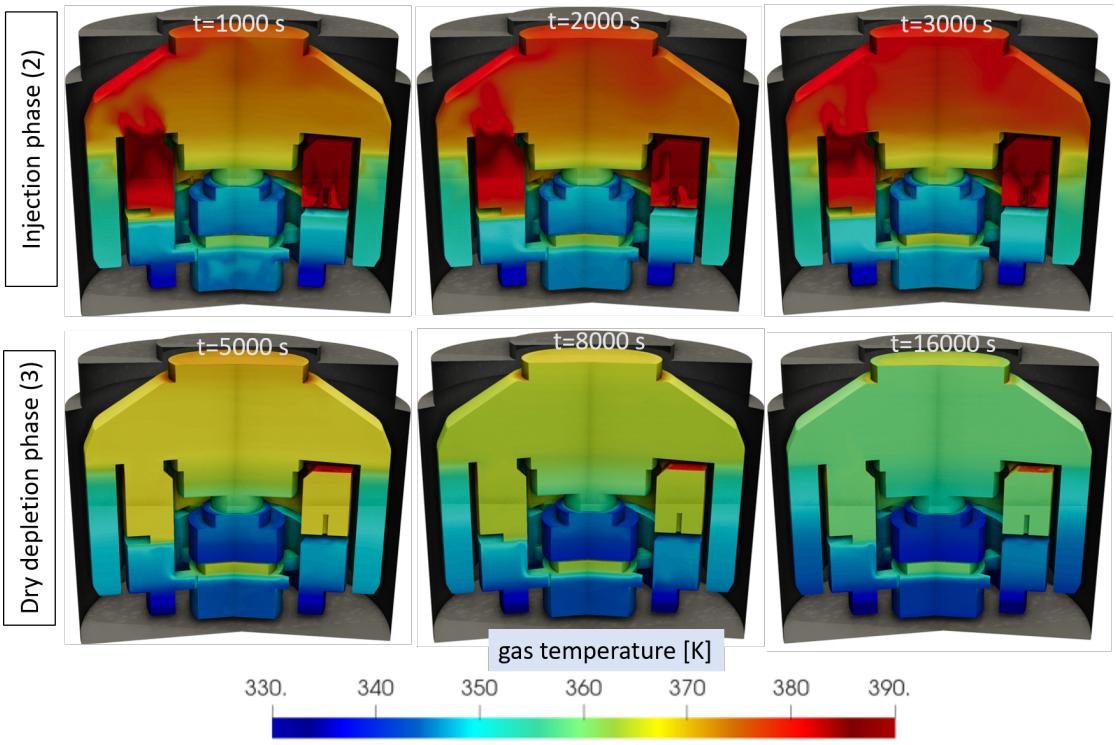

Figure 5.16: VANAM: Transient evolution of the simulated gas temperature during the 1st injection and dry depletion phase.

injection phase, the superheated steam-air-NaOH mixture is injected into the upper steam generator compartment R5 and mainly flows through the overflow opening into the dome. A secondary flow path is observed via the passage connecting R5 and R7 and through another opening into the dome zone (R9). The gas temperature continuously decreases along the flow path. Steam condensation occurs primarily on the upper dome structure and only on the lower wall sections of R5 and R7 since the upper structures are

already strongly heated up during the pre-conditioning phase. A stratified steam layer is formed in the upper dome region down to the elevation of the overflow openings. At the same time, there is only a limited amount of steam transported to the lower steam generator compartments (R6 and R8), reactor room and cavity (R1 and R3), or annular compartments (R9). In the depletion phase, the atmospheric temperature distribution homogenizes, with a visible difference between the regions above the injection and the colder lower compartments.

The gas temperature evolution is quantitatively compared against the measurements in Figure 5.17. Those measurements above the injection location (R5) are well predicted during the injection phase, while more significant quantitative deviations are observed in the lower compartments (R4, R6, R8, and R3). Here the predicted gas temperature drops before the start of 'phase 2' (time = 0 s) before it rises again, corresponding to the pressure rise during the injection. Furthermore, the higher gas temperatures in the lower compartments (R6 -blue lines and R3 -black lines) indicate a more substantial transport of hot steam into these regions in the experiment. In depletion phase, the simulation predicts a qualitatively consistent but quantitatively stronger homogenization of the gas temperature among the upper region (R5, R7, R9) and the lower compartments R6, R8, and R9 (2.2m). Generally, the observed stratification is confirmed by the measurements, while the lower overall temperature level predicted in this phase corresponds to the lower pressure level prediction.

The evolution of the predicted NaOH aerosol distribution (dry aerosol mass concentration) is illustrated in Figure 5.18 and is compared to the measurements in Figure 5.19. The NaOH aerosol is first transported with the steam-air mixture through the SG compartments (R5/7) to the dome compartment R9. From there, it settles and is transported to the lower compartments (R9 and R3). Generally, a decreasing airborne concentration with time is observed primarily due to gravitational settling but, to a lesser extent, also due to thermophoretic and diffusiophoretic deposition.

The quantitative assessment of the predicted aerosol concentrations is difficult due to the sparse measurement points in space and time (filter stations) and considerable measurement uncertainty. Nonetheless, a few qualitative observations can be made on Figure 5.19. The lesser predicted decay rate (slope) in the first half of the depletion phase indicates that the settling rate is underpredicted in the simulation. This may be partially attributed to uncertainties on the specified aerosol size distribution at the

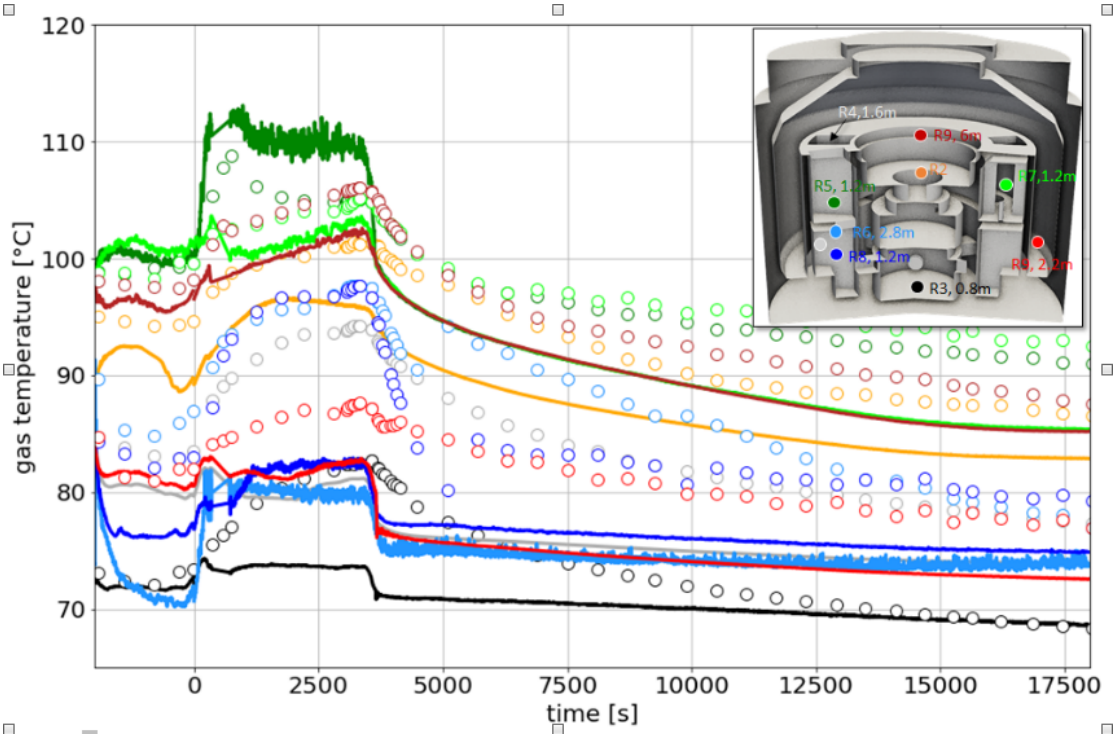

Figure 5.17: VANAM: Comparison of gas temperature transients between the experiment (circle) and simulation (solid lines). Color coding indicates the measurement locations.

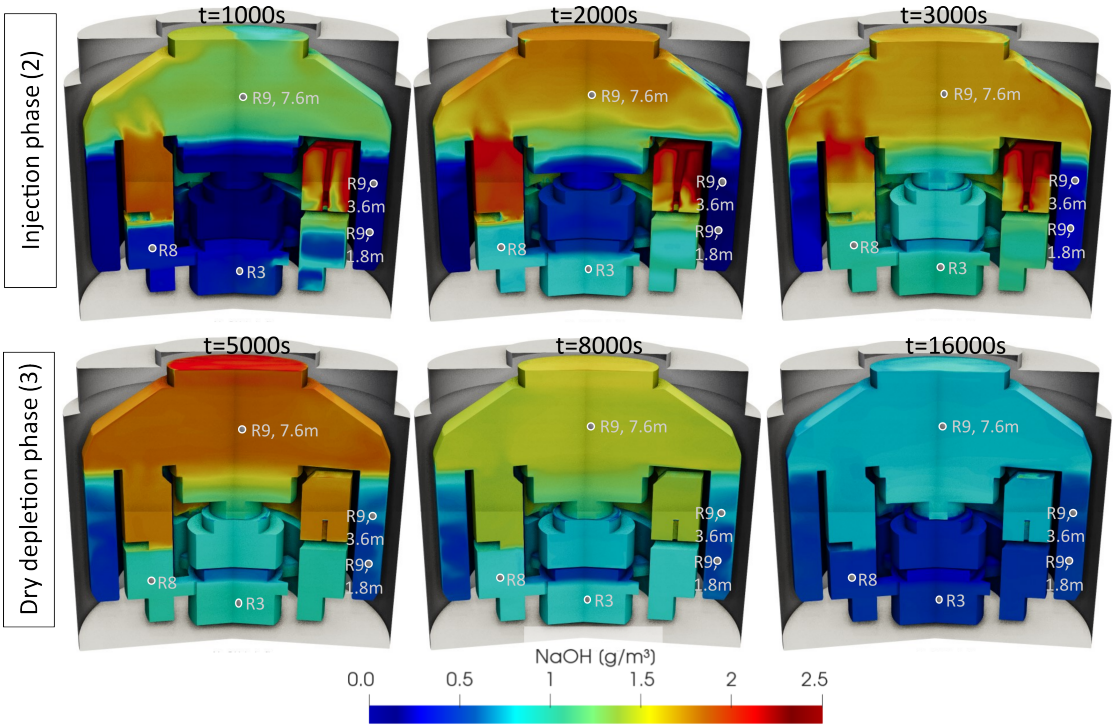

Figure 5.18: VANAM: Transient evolution of the simulated NaOH aerosol concentration during the 1st injection and dry depletion phase.

injection location. The relative comparison of the dry NaOH concentration among the sensors indicates differences between simulation and experiment. For example, around time $\sim$ 12000s, in the experiment, the maximum NaOH concentration is in the stagnant gas volume of the annular compartment (R9, 3.6m). In contrast, the simulation predicts a maximum NaOH concentration in the upper dome. On the other hand, the transport into the lower steam generator compartment (R8) and reactor cavity (R3) are visibly stronger in the simulation than characterized experimentally. These observations cannot be further explained based on the available data and require a deeper comparison against other codes' predictions and refined analysis with improved thermo-fluid dynamic conditions.

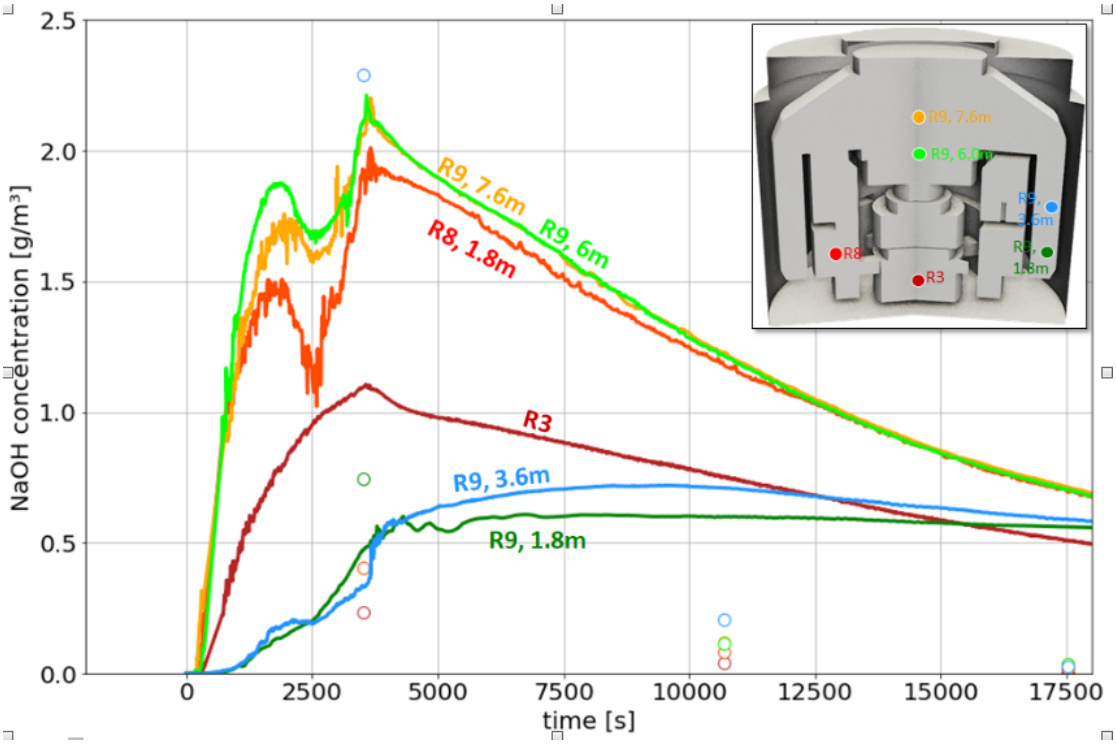

Figure 5.19: VANAM: Comparison of NaOH aerosol concentration transients between the experiment (circle) and simulation (solid lines). Color coding indicates the measurement locations.

5.2.4 Summary of the VANAM-M3 simulation

As a step towards a future full-scale containment analysis with the *containmentFOAM* package, an integral application-oriented assessment of its CFD models was conducted based on the ISP-37 VANAM M3 experiment conducted in the technical scale Batelle Model Containment in 1993. Besides the transport and condensation of steam

and corresponding pressurization, the experiment also addresses the transport and deposition of the hygroscopic aerosol material NaOH (a simulant for nuclear aerosol material CsOH). The primary objective of the work was to demonstrate the applicability and interaction of the multi-physics models on a technical scale with respect to numerical performance and to qualitatively assess the prediction results based on the limited available experimental data.

The simulation results regarding pressurization and gas transport were in reasonable agreement with the measurement results, and observed deviations can be related to the significant uncertainty in the definition of the boundary conditions and the leak rate. Considering aerosol transport, experimental data is too limited for both the description of injection boundary conditions and the assessment of transient evolution. Therefore, future work will also focus on code-to-code comparison with the existing analysis of ISP-37.

The CFD approach proved to be numerically efficient and stable. It achieved run times (physical time/day computing time) of about 400 s for the injection phase and up to 1100s for the depletion phase on a 4.5 Million cells mesh and a medium-sized cluster of 128 Xeon® Gold CPU.

CHAPTER 6

Summary and future perspectives

6.1 SUMMARY AND CONCLUSIONS

During a severe accident, hydrogen combustion events may challenge the integrity of the containment building and eventually result in the release of radioactive material into the environment. Accurate prediction of hydrogen-steam-air composition with simulation tools paves the way for effective accident management. The gas mixing in a containment is governed by multiple phenomena such as buoyancy, turbulence, multicomponent gas system, wall and bulk condensation of steam, radiation heat transport, and conjugate heat transfer. Radioactive aerosols and noble gases, carrying decay heat, are also released into the containment during a core melt accident. The impact of aerosol decay heat on the thermal-hydraulics in a containment is of great research interest. The previous research project at RWTH Aachen University and Forschungzentrum Juelich (Kampili, 2022) studied the influence of aerosol decay heat on buoyancy-driven flows in a small scale DIANA facility (L $\sim$ 0.7 m). The particle phase was treated with a sophisticated Lagrangian approach. But the Lagrangian treatment of aerosol particles is computationally expensive considering the containment scale (L $\sim$ 50 m). Consequently, in the present work, a computationally efficient CFD model based on the simplified Euler-Eulerian framework is developed to run an integral containment analysis. The impact of aerosol decay heat on the buoyancy-driven gas mixing in a large-scale THAI facility (H $\sim$ 9.2 m) is analyzed. Attention is also given to modeling the enhanced gravitational settling of nuclear aerosols in humid atmospheres.

The major objective of the present work is to build an computationally efficient and well balanced model set. The flow prevailing in a containment is incompressible from the perspective of flow velocities (Ma < 0.3), but the density varies due to the multicomponent gas mixture's temperature and mass concentration gradients. Thus, the Boussinesq approximation of buoyancy becomes untenable, and the ideal gas equation of state models the varying density. Due to the large size of a nuclear reactor containment, scale resolving approaches such as LES or hybrid RANS-LES becomes computationally expensive; therefore, an unsteady RANS (U-RANS) approach based on the standard k-ω-SST model is used. In stably stratified regions or stagnant zones of a containment, the gas molecular diffusion becomes the dominant mechanism. Therefore, using a constant molecular diffusivity for all gas species is error-prone. At the same

time, using the accurate Stefan Maxwell diffusion model increases the numerical cost. As a trade-off, the *Effective binary diffusivity* method is employed. From the literature survey, steam condensation on the cold walls is modeled with two approaches—*Face-flux* and *Volumetric source terms*. In the present work, it was successfully demonstrated that the *Face-flux* method is numerically robust and less grid sensitive compared to the *Volumetric source terms* model.

To facilitate application to technical scales, the aerosol transport is modeled with an efficient Eulerian approach—*Mixture model*. In addition to the standard forces of drag, inertia, and buoyancy, the thermophoretic and diffusiophoretic forces are considered in the CFD model. Especially, thermophoresis and diffusiophoresis become critical phenomena due to the substantial temperature and concentration gradients prevailing near the condensing walls. In containment atmospheres with low gas flow velocities, the gravitational settling of aerosol particles determines the local aerosol concentration. Gravitational settling is mainly influenced by particle size distribution. Based on the literature review, particle growth due to steam condensation and coalescence are the critical mechanisms determining the particles' size distribution evolution. Within the scope of this thesis, only the former phenomenon is addressed. The relative humidity in a containment atmosphere can vary significantly between locations. The nuclear aerosols, such as CsI and CsOH, are hygroscopic, i.e., they can absorb water even at sub-saturation conditions (RH < 100%). Therefore, the hygroscopicity model is formulated and implemented in the current CFD model. In the present work, two approaches are used to capture the evolution of particle size distribution—*Fixed sectional* method and *Log-normal* method. The *Fixed sectional* method splits the overall range of particle sizes into N-sections and solves a number concentration equation for each section. The *Log-normal* method assumes a log-normal particle size distribution and solves for only one transport equation for a median number concentration. The *Fixed sectional* method gives detailed insights into the evolution of particle size distribution. In contrast, the *Log-normal* method is computationally cheap and can be used for large-scale analysis.

The CFD model is systematically validated: First, the gas transport modeling is validated against small-scale experiments and then against the technical scale THAI experiments. Subsequently, the hygroscopic particle growth and the resultant gravitational settling modeling is validated against the AHMED experiments.

The buoyancy and turbulence modeling is initially validated against the 2D

differentially heated square cavity (DHSC) case (L $\sim$ 0.75 m, Ra $\sim$ 10^9). The CFD model predicted reasonable accuracy of the gas flow field, temperature, and local convective wall heat fluxes. From this simple 2D test, it was revealed that the standard wall functions derived for forced convection flows could not be used to model the buoyancy-dominant flows in a containment. Consequently, the boundary layer should be resolved with a fine mesh ($y^+ < 2$) to capture the wall fluxes—shear stress, heat flux—accurately. Modeling the surface to surface radiation heat transfer is indispensable in simulating natural convection flows. The radiation effect increased the overall heat transfer from the walls and affected the gas temperature distribution.

The SETCOM experiments were primarily used to validate the *Face-flux* wall condensation model. Three cases with differing condensation rates were chosen in the forced convection regime to test the model's ability to predict mild to severe condensation scenarios. The results *Face-flux* method were in agreement with the experiment data for all three cases on both the fine (y^+ 1) and coarse (y^+ 75) meshes. Since the wall functions used in the current work are derived for fully-developed forced convection flows, the coarse-mesh solution compared reasonably with the fine-mesh solution in the developed part of the flow. Still, it deviated in the developing flow at the channel's entrance. Also, for higher condensation rates, grid-dependency was observed because of the "suction effect," which tends to change the profile in the log-law part of the boundary layer. Though containment flows are predominantly in the mixed convection/natural convection regime, the current validation proves that the *Face-flux* method, when used with wall functions appropriate for a specific flow regime, can model the steam condensation on walls accurately on even the meshes with under-resolved boundary layer thereby significantly reducing the computational cost.

Three experiments conducted in the THAI experimental facility on buoyancy-driven flows were taken to validate the CFD model. The experiments were in increasing order of complexity and included multiple interacting phenomena—buoyancy, turbulence, multicomponent gas transport, wall condensation, and radiation heat transfer. The TH21 experiment analyzed the turbulent natural circulation flow of a single species (dry air). For the 3D model of the THAI vessel, grid-insensitive results were obtained for a mesh with approximately 2 million cells. The same mesh was utilized to run all the THAI simulations discussed in the present thesis. The gas species in the TH21 experiment—dry air—is transparent to radiation; hence the fvDOM radiation model is employed. The velocity and temperature profiles obtained from the THAI-TH21 simulation reasonably

agreed with the experimental data. But the results were sensitive to the choice of wall emissivity, whose measurements were not available from the experimental inputs. The surface-to-surface radiation heat transfer between the internal walls (in contact with the gas) increased the net heat transfer rate on the external walls and resulted in an amplified quasi-stead-state pressure. The temperature gradients along the internal walls are affected by the choice of wall emissivity, thereby causing differences in the flow field. However, the natural circulation flow was well predicted and the model settings can be considered to be applicable to simulated the THAI-TH22 (helium-air mixing) and THAI-TH24 (steam-air mixing) experiments.

In the THAI-TH22 experiment, the erosion of a stably stratified helium-air layer by the persisting natural convection flow-field is studied. Since both helium and dry-air are transparent to radiation, the fvDOM model captures the radiation heat transfer between the internal walls. The transients of the helium concentration and temperature obtained from the CFD model reasonably agreed with the experimental data, but the mixing time was over-predicted by 18%. The simulations predict a complete flow blockage once helium injection is complete and the dominant mixing mechanism is only gas diffusion. But in the experiment, a weak bulk motion into the inner-cylinder is observed, which hastens the breakage of the stably stratified gas layer, thereby promoting the early onset of natural circulation flow. This may be due to the geometric simplifications employed in the CFD model or uncertainty in model parameters, e.g., wall emissivity. Nonetheless, a qualitatively consistent mixing transient is obtained, proving the model's validity.

Natural convection-driven erosion of stably stratified steam-air layer is analyzed in the THAI-TH24 experiment. Since steam is a participative gas medium in radiation heat transport, the sophisticated fvMCM radiation model is used. Overall, a good agreement was found in the transients of steam concentration between the simulation and the experiment. Also, the condensate quantity measured in the experiment and the temperature of the cooled wall makes for a good comparison with the simulation results, implying that *Face-flux* wall condensation model along with the conjugate heat transfer boundary conditions used are valid. In the experiment, an unknown quantity of liquid water was injected as droplets (along with steam), which evaporated in the gas atmosphere, leading to lower gas temperature and increased steam concentration levels and pressure. This unquanitified amount of water droplet inject can hardly be given as a boundary condition in the simulation. Besides this, the CFD model consistently

reproduced the transients of steam layer erosion due to natural convection.

In the AHMED facility, experiments were conducted to study the gravitational settling of hygroscopic (NaOH, CsI, and CsOH) and non-hygroscopic aerosol (Ag) particles under dry and humid atmospheres. Low aerosol particle number concentration used in the experiments ensures that the particle size distribution is not affected by coalescence and only particle growth through water absorption is dominant. Since the gravitational settling of aerosol particles is a one-dimensional phenomenon, the three-dimensional computational domain of the AHMED facility is simplified with a one-dimensional domain. Sensitivity analysis revealed that 32 size sections are needed to resolve the aerosol depletion behavior correctly with the *Fixed sectional* model. The CFD model accurately predicted the depletion behavior of the non-hygroscopic silver aerosol particles at RH = 54%. There is no particle growth due to condensation at this humidity, and the aerosol particles settling under gravity is the only phenomenon. For the water-absorbing NaOH aerosol particles, the CFD simulations correctly predicted the settling behavior at different humidity conditions (RH = 22% to 96%). The simulation results matched the trends of gravitational settling for CsI and CsOH aerosol particles. Still, they predicted a slower depletion rate than the experimental data at low and high relative humidity conditions. There is no particle growth due to condensation at low relative humidity (RH = 27%) for CsI, and the gravitational settling is determined only by the initial particle size distribution. Only an error in the initial particle size distribution specification could explain the difference between simulation results and the experiments. Concluding, the aerosol model successfully predicted the phenomenology and proved to be application ready.

As a first application, the CFD model is applied to estimate the effect of aerosol particles' decay heat on containment typical flows. Two hypothetical test cases were set up on the THAI-TH22 and THAI-TH24 experiments. In the TH22 based simulation, decay heat carrying CsI aerosol particles, having a log-normal distribution (AMMD = 2.3 $\mu\mathrm{m}$ and GSD = 1.7), amounting to a mean concentration of 1 $\mathrm{g\,m^{-3}}$, are injected along with the helium gas into the upper part of the THAI vessel. The decay heat of the aerosols was expected to heat the helium layer and make it more stably stratified. But, unexpectedly, the decay heat caused local buoyant flows in the upper part of the THAI vessel and homogenized the helium concentration. The mixing phenomenon was entirely different from the actual TH22 simulation and eventually resulted in a shorter mixing time. In the TH24 based simulation, the same amount of aerosol particle

mass was injected along with the steam gas into the upper part of the vessel. The decay heat of aerosols increased the temperature of the steam layer thereby making it more stably stratified and hence slowed down the mixing process as expected. It is demonstrated that the decay heat of aerosols can significantly impact the flow and transport processes in containment and thus cannot be neglected for H_2 risk analysis. This conclusion should be further substantiated by investigating the decay heat effects of different aerosol materials, concentrations, and scenarios.

A second application addresses the simulation of the ISP-37 (VANAM-M3) experiment in the technical scale Battelle Model Containment (BMC). Besides pressurization and steam distribution in the 615 m^3 multi-compartmented building, the experiment addresses the transport and deposition of the hygroscopic NaOH aerosols (simulant for CsOH). The objective of this simulation is to demonstrate the model's applicability and computational efficiency on a technical scale rather than model validation. The latter will be difficult due to sparse instrumentation and limited inputs for this old experiment conducted in the year 1993. However, the CFD model predicts the pressurization, steam, and aerosol particles transport with reasonable accuracy. The observed deviation between the simulation and the experiment can be attributed to uncertainty in boundary conditions obtained from the digitization of plots. The model proved to be numerically robust, completing the fast injection phase at the speed of 400 seconds of physical time per day and the relatively slow flows during the depletion phase at 1100 seconds per day.

Concluding, the CFD model's validity and computational efficiency were successfully demonstrated. This enables future applicability of *containmentFOAM* CFD code to simulate an actual severe accident scenario in a nuclear reactor containment, which is unprecedented so far. Furthermore, the scoping analysis of decay heat effects of aerosol particles on containment flows motivates a closer look in this direction.

6.2 FUTURE PERSPECTIVES

In the current work, a computationally efficient and well-balanced Euler-Euler based CFD model is proposed to simulate the multicomponent gas flow and aerosol transport in a nuclear reactor containment in a severe accident scenario. The model is systematically validated, first against a small scale experiments and then against technical scale experiments on natural convection flows in the THAI facility.

From the simulation results of the SETCOM forced convection experiments, it is clear that the wall functions along with the *Face-flux* wall condensation model give grid insensitive results. But for buoyancy-driven flows in a containment, the near-wall region had to be resolved with $y^+ < 2$ mesh to capture the wall fluxes—wall shear stress, heat flux, and condensation rate—accurately. Efforts are already underway at Forschungzentrum Juelich in collaboration with RWTH Aachen University through the SETCOM project to develop wall functions applicable to all flow regimes—forced convection, mixed convection, and natural convection (Kelm *et al.*, 2019*b*). Integrating the generic wall functions with *containmentFoam* will allow for a coarser near-wall grid resolution and significantly reduce the computational time for large scale applications, e.g., VANAM experiment.

Apart from the drag and inertial forces, the particle deposition on condensing walls of a containment depends on thermophoresis, diffusiophoresis, and turbophoresis. In the current CFD model, state-of-the-art implementations of thermophoresis and diffusiophoresis are already available. But from the fundamental 2D, differentially heated square cavity case, it is clear that the k-ω-SST turbulence model underpredicts the turbulence kinetic energy (TKE) closer to the walls, especially for cases with a low level of turbulence (Ra $\sim 10^9$). Incorrect TKE prediction results in inaccurate modeling of turbophoresis. To this end, low Reynolds number corrections should be employed to get an improved TKE prediction and hence accurate modeling of particle deposition on the walls (Wilcox, 2006).

Simulations of the AHMED experiment have revealed that the prediction of aerosol depletion rate due to gravitational settling is sensitive to the initial size distribution. Ongoing experiments at Forschungzentrum Juelich focuses on the gravitational settling of nuclear aerosols in both dry and wet conditions at the in-house INEX facility. Therefore, more details on the initial size distribution are available. The validation of the CFD model against the INEX data will separate model deficiency from the errors due to incorrect boundary conditions.

The gravitational settling behavior of aerosol depends on the evolution of the particle size distribution. Particle growth due to condensation and coalescence/agglomeration are the major mechanisms determining the size distribution. The aerosol particle concentration in a containment atmosphere is typically around 1 $\mathrm{g\,m^{-3}}$, but local concentrations can go up to 100 $\mathrm{g\,m^{-3}}$. The particle number concentrations can

exceed 10^{13} per m^3, and therefore, the agglomeration of particles becomes an important phenomenon. In the present work, particle growth due to condensation is modeled with the *Log-normal* method. In the future, the agglomeration of particles due to the relative motion under gravity, Brownian diffusion, turbulent diffusion, turbulent inertia, and electrostatic forces have to be implemented within the existing framework.

The present work considers only the influence of aerosol decay heat on buoyancy-driven gas mixing and containment pressurization. In reality, the aerosol particles deposited on the walls release heat onto the walls and affect the local steam condensation. A proportion of the aerosol particles are washed into the sump through prevailing condensate flows and results in evaporation of sump water (Allelein *et al.*, 2007). The CFD models should include these phenomena to simulate an actual containment accident sequence. But two-phase (gas-liquid) modeling is necessary to simulate the liquid films on the walls and subsequent aerosol deposition on the liquid films. Extending *containmentFOAM* to include a two-phase approach is recommended. Also, the decay heat of CsI aerosol particles was assigned a constant value of $111.57\ \mathrm{kW\,kg^{-1}}$ similar to the preceding work of Kampili (2022). Though this approach is reasonable for the short transients considered in the THAI vessel ($\sim$ 4000s), in reality, the decay heat source of a nuclear aerosol particle varies with time. Therefore, in the future, it is recommended to model the decay heat source as physically as possible and analyze its impact on more prolonged transients.

The uncertainty in the boundary conditions of the VANAM-M3 experiment made it difficult to separate the modeling deficiencies from the error caused due to uncertainty in boundary conditions. Therefore, the CFD model should be validated against results obtained with system codes like COCOSYS or integral analysis codes like MELCOR for the same boundary conditions to substantiate the progress of the approach presented in this thesis.

For the VANAM-M3 experiment, only the first injection phase and the "dry" depletion phase have been completed ($\sim$ 20,000 s) in the simulation. Only in the second injection phase followed by the "wet" depletion of aerosols under super-saturated conditions. While this analysis exceeded the frame of this thesis, it is the next logical step to assess the model's applicability for technical scale analysis. Similar to VANAM, parametric studies on large scale tests involving long transients must be done to make the model eventually applicable for a containment scale.

REFERENCES

1. **Allelein, H.-J.**, **S. Arndt**, **W. Klein-Hessling**, **S. Schwarz**, **C. Spengler**, and **G. Weber** (2008). Cocosys: Status of development and validation of the german containment code system. *Nuclear Engineering and Design*, **238**(4), 872 – 889. ISSN 0029-5493.

2. **Allelein, H.-J.**, **A. Auvinen**, **J. Ball**, **S. Güntay**, **L. E. Herranz**, **A. Hidaka**, **A. V. Jones**, **M. Kissane**, **D. Powers**, and **G. Weber** (2009). State-of-the-Art Report (SOAR) on Nuclear Aerosols. Technical Report 611688, OECD-NEA.

3. **Allelein, H.-J.**, **K. Fischer**, **J. Vendel**, **J. Malet**, **E. Studer**, **S. Schwarz**, **M. Houkema**, **M. PaillËre**, and **A. Bentaib** (2007). International Standard Problem: ISP-47 on Containment Thermal Hydraulics. Final Report NEA/CSNI/R(2007)10, OECD-NEA.

4. **Amano, Y.** (2015). The Fukushima Daiichi Accident. Report by the Director General GC(59)/14, International Atomic Energy Agency.

5. **Ampofo, F.** and **T. Karayiannis** (2003). Experimental benchmark data for turbulent natural convection in an air filled square cavity. *International Journal of Heat and Mass Transfer*, **46**(19), 3551 – 3572. ISSN 0017-9310.

6. **Antoine, C.** (1888). Tensions des vapeurs; nouvelle relation entre les tensions et les températures. *Comptes Rendus des Séances de l'Académie des Sciences (in French)*, **107**, 681–684.

7. **Asgari, M.**, **F. Lucci**, and **A. K. Kuczaj** (2021). Multispecies aerosol evolution and deposition in a human respiratory tract cast model. *Journal of Aerosol Science*, **153**(August 2020), 105720. ISSN 18791964.

8. **ASME** (2008). Procedure for estimation and reporting of uncertainty due to discretization in CFD applications. *Journal of Fluids Engineering*, **130**(7), 078001–078001–4.

9. **Auban, O.**, **R. Zboray**, and **D. Paladino** (2007). Investigation of large-scale gas mixing and stratification phenomena related to lwr containment studies in the panda facility. *Nuclear Engineering and Design*, **237**(4), 409–419. ISSN 0029-5493.

10. **Balaji, C.** and **S. Venkateshan** (1993). Interaction of surface radiation with free convection in a square cavity. *International Journal of Heat and Fluid Flow*, **14**(3), 260 – 267. ISSN 0142-727X.

11. **Bentaïb, A.**, **H. Bonneville**, and **G. Cénérino**, *Nuclear power reactor core melt accidents. State of knowledge*. EDP Sciences, 2015. ISBN 9782759818358.

12. **Bucci, M.**, **W. Ambrosini**, and **N. Forgione** (2013). Experimental and Computational Analysis of Steam Condensation in the Presence of Air and Helium. *Nuclear Technology*, **181**(1), 115–132. ISSN 0029-5450.

13. **Camuffo, D.**, *Microclimate for Cultural Heritage*. Elsevier, 2014. ISBN 9780444641069.

14. **Chung W. and Devaud C. B.** (2008). Buoyancy-corrected k– models and large eddy simulation applied to a large axisymmetric helium plume. *International Journal for Numerical Methods in Fluids*, **58**(1), 57–89.

15. **Dehbi, A.** (2008). A CFD model for particle dispersion in turbulent boundary layer flows. *Nuclear Engineering and Design*, **238**(3), 707–715. ISSN 00295493.

16. **Dehbi, A.**, **F. Janasz**, and **B. Bell** (2013). Prediction of steam condensation in the presence of noncondensable gases using a CFD-based approach. *Nuclear Engineering and Design*, **258**, 199–210. ISSN 00295493.

17. **Dehbi, A.**, **S. Kelm**, **J. Kalilainen**, and **H. Mueller** (2019). The influence of thermal radiation on the free convection inside enclosures. *Nuclear Engineering and Design*, **341**, 176 – 185. ISSN 0029-5493.

18. **ERCOFTAC**, *Best Practice Guidelines - Industrial Computational Fluid Dynamics of Single-Phase Flows, Version 1*. European Research Community on Flow Turbulence and Combustion (ERCOFTAC), 2001.

19. **Favre, A.**, **R. Dumas**, **E. Verollet**, and **M. Coantic** (1966). Couche limite turbulente sur paroi poreuse avec aspiration. *Journal de Mecanique*, **5**(1), 3–28.

20. **Firnhaber, M.**, **T. Kanzleiter**, **S. Schwarz**, and **G. Weber** (1996). International standard problem ISP37: VANAM M3 - A Multi compartment aerosol depletion test with hygroscopic aerosol material. Comparison Report NEA/CSNI/R(1996)26, OECD-NEA.

21. **Fischer, K.**, **S. Gupta**, and **A. Kühnel** (2009). THAI-Konvektionsversuch TH21. Technical Report 1501325, Becker Technologies GmbH, Eschborn.

22. **Frederix, E.**, **A. Kuczaj**, **M. Nordlund**, **A. Veldman**, and **B. Geurts** (2017). Eulerian modeling of inertial and diffusional aerosol deposition in bent pipes. *Computers & Fluids*, **159**, 217–231. ISSN 00457930.

23. **Frederix, E. M. A.**, *Eulerian modeling of aerosol dynamics*. University of Twente, 2016. ISBN 9036542286.

24. **Fuller, E. N.**, **P. D. Schettler**, and **J. C. Giddings** (1966). New method for prediction of binary gas-phase diffusion coefficients. *Industrial Engineering Chemistry*, **58**(5), 18–27.

25. **Gupta, S.**, **K. Fischer**, **G. Langer**, **B. Balewski**, and **A. Kühnel** (2010). Comparison report of simulations of THAI Test TH22, dissolution of a light gas stratification by natural convection. Technical Report 1501361, Becker Technologies GmbH, Eschborn.

26. **Gupta, S.**, **E. Schmidt**, **B. von Laufenberg**, **M. Freitag**, **G. Poss**, **F. Funke**, and **G. Weber** (2015). THAI test facility for experimental research on hydrogen and fission product behaviour in light water reactor containments. *Nuclear Engineering and Design*, **294**, 183–201. ISSN 00295493.

27. **Gupta, S.**, **E. Schmidt-Naujok**, **B. Balewski**, and **G. Langer** (2012). Dissolution of a Steam-Air Stratification by Natural Convection-Test ID: TH-24 (CV5). Technical Report 1501361–TH24–FB/TR, Becker Technologies GmbH, Eschborn.

28. **Jokiniemi, J.** (1990). Effect of selected binary and mixed solutions on steam condensation and aerosol behavior in containment. *Aerosol Science and Technology*, **12**(4), 891–902. ISSN 15217388.

29. **Kader, B. A.** (1981). Temperature and concentration profiles in fully turbulent boundary layers. *International Journal of Heat and Mass Transfer*, **24**(9), 1541–1544. ISSN 00179310.

30. **Kampili, M.** (2022). *Euler-Lagrangian Modeling of Aerosol Transport , Deposition and Impact of Nuclear Decay Heat*. Ph.D. thesis, RWTH Aachen University.

31. **Kanzleiter, T.** (1993). VANAM Multi-Compartment Aerosol Depletion Test M3 with Soluble Aerosol Material. Technical Report BIeV-R67.098-304, Batelle-Institut e.V., Frankfurt.

32. **Kanzleiter, T.** (1995). Experiments on the Aerosol Behavior Within a Multi-Compartment Containment - VANAM Tests. Final Report BIeV-R67.098-01, Batelle-Institut e.V., Frankfurt.

33. **Karwat, H.**, **J. Bardelay**, **T. Hashimoto**, **G. W. Koroll**, **M. Krause**, **J.-P. L'Heriteau**, **P. Lundstroem**, **A. Notafrancesco**, **P. Royl**, **B. Schwinges**, **H. Tezuka**, **J. Tills**, and **J. Royen** (1999). SOAR on Containment Thermalhydraulics and Hydrogen Distribution. Technical Report NEA-CSNI-R–1999-16, OECD-NEA.

34. **Kelm, S.**, **M. Kampili**, **V. K. Gopala Krishna Moorthy**, **K. Sakamoto**, **X. Liu**, **C. Druska**, **A. Kuhr**, **K. Prakash**, and **H.-J. Allelein**, Development and first validation of the tailored cfd solver 'containmentfoam' for analysis of containment atmosphere mixing. *In 18th International Topical Meeting on Nuclear Reactor Thermal Hydraulics (NURETH-18)*. Portland, Oregon, USA, 2019*a*.

35. **Kelm, S.**, **M. Kampili**, **X. Liu**, **A. George**, **D. Schumacher**, **C. Druska**, **S. Struth**, **A. Kuhr**, **L. Ramacher**, **H.-J. Allelein**, **K. A. Prakash**, **G. V. Kumar**, **L. M. Cammiade**, and **R. Ji** (2021). The Tailored CFD Package 'containmentFOAM' for Analysis of Containment Atmosphere Mixing, H2/CO Mitigation and Aerosol Transport. *Fluids*, **6**(3), 100. ISSN 2311-5521.

36. **Kelm, S.**, **M. Klauck**, **S. Beck**, **H.-J. Allelein**, **G. Preusser**, **M. Sangiorgi**, **W. Klein-Hessling**, **I. Bakalov**, **A. Bleyer**, **A. Bentaib**, **I. Kljenak**, **M. Stempniewicz**, **P. Kostka**, **S. Morandi**, **B. Ada del Corno**, **C. Bratfisch**, **T. Risken**, **L. Denk**, **Z. Parduba**, **S. Paci**, **A. Manfredini**, **A. Silde**, **P. Juris**, **J. Jancovic**, **H. Lele**, and **S. Ganju** (2014). Generic Containment: Detailed comparison of containment simulations performed on plant scale. *Annals of Nuclear Energy*, **74**, 165–172. ISSN 03064549.

37. **Kelm, S.**, **J. Lehmkuhl**, **W. Jahn**, and **H.-J. Allelein** (2016*a*). A comparative assessment of different experiments on buoyancy driven mixing processes by means of cfd. *Annals of Nuclear Energy*, **93**, 50 – 57. ISSN 0306-4549.

38. **Kelm, S.**, **H. Mueller**, and **H.-J. Allelein**, Importance of thermal radiation heat transfer modeling in containment typical flows. *In Proc. OECD/NEA & IAEA Workshop on Experiments and CFD Codes Application to Nuclear Reactor Safety (CFD4NRS)*. Cambridge MA, USA, 2016*b*.

39. **Kelm, S.**, **H. Müller**, **A. Hundhausen**, **C. Druska**, **A. Kuhr**, and **H. J. Allelein** (2019*b*). Development of a multi-dimensional wall-function approach for wall condensation. *Nuclear Engineering and Design*, **353**(August), 110239.

40. **Kelm, S.**, **M. Ritterath**, **H.-M. Prasser**, and **H.-J. Allelein** (2016*c*). Application of the minipanda test case 'erosion of a stratified layer by a vertical jet' for cfd validation. *Nuclear Engineering and Design*, **299**, 124 – 135. ISSN 0029-5493.

41. **Kumar, G. V.**, **M. Kampili**, **S. Kelm**, **K. A. Prakash**, and **H.-J. Allelein** (2020). CFD modelling of buoyancy driven flows in enclosures with relevance to nuclear reactor safety. *Nuclear Engineering and Design*, **365**, 110682. ISSN 0029-5493.

42. **Lehmkuhl, J.**, **S. Kelm**, **M. Bucci**, and **H. J. Allelein** (2016). Improvement of wall condensation modeling with suction wall functions for containment application. *Nuclear Engineering and Design*, **299**, 105–111. ISSN 00295493.

43. **Liu, X.**, **S. Kelm**, **M. Kampili**, **G. V. Kumar**, and **H.-J. Allelein** (2022). Monte Carlo method with SNBCK nongray gas model for thermal radiation in containment flows. *Nuclear Engineering and Design*, **390**(January), 111689. ISSN 00295493.

44. **Lucci, F.**, **E. Frederix**, and **A. K. Kuczaj** (2022). AeroSolved: Computational fluid dynamics modeling of multispecies aerosol flows with sectional and moment methods. *Journal of Aerosol Science*, **159**(August 2020), 105854. ISSN 18791964.

45. **Mahaffey, J.** (2015). Best Practice Guidelines for the Use of CFD in Nuclear Reactor Safety Application - Revision. Technical Report NEA/CSNI/R(2014)11, OECD/NEA.

46. **Mäkynen, J. M.**, **J. Jokiniemi**, **P. P. Ahonen**, **E. I. Kauppinen**, and **R. Zilliacus** (1997). AHMED experiments on hygroscopic and inert aerosol behaviour in LWR containment conditions: Experimental results. *Nuclear Engineering and Design*, **178**(1), 45–59. ISSN 00295493.

47. **Manninen, M.**, **V. Taivassalo**, and **S. Kallio** (1996). On the mixture model for multiphase flow. Technical Report VTT-PUB-288, Technical Research Centre of Finland, Espoo (Finland).

48. **Menter, F.** and **T. Esch**, Elements of industrial heat transfer prediction. *In Elements of Industrial Heat Transfer Prediction*. 2001.

49. **Minkowycz, W. J.** and **E. M. Sparrow** (1966). Condensation heat transfer in the presence of noncondensables, interfacial resistance, superheating, variable properties, and diffusion. *International Journal of Heat and Mass Transfer*, **9**(10), 1125–1144. ISSN 00179310.

50. **Mishra, G.**, **A. K. Mandariya**, **S. N. Tripathi**, **Mariam**, **M. Joshi**, **A. Khan**, and **B. K. Sapra** (2019). Hygroscopic growth of CsI and CsOH particles in context of nuclear reactor accident research. *Journal of Aerosol Science*, **132**(May 2018), 60–69. ISSN 18791964.

51. **Newbold, F. R.** and **N. R. Amundson** (1973). A model for evaporation of a multicomponent droplet. *AIChE Journal*, **19**(1), 22–30. ISSN 15475905.

52. **OECD-NEA** (2015). Status Report on Hydrogen Management and Related Computer Codes. Technical Report NEA/CSNI/R(2014)8, OECD-NEA.

53. **Riella, M.**, **R. Kahraman**, and **G. Tabor** (2018). Reynolds-Averaged Two-Fluid Model prediction of moderately dilute fluid-particle flow over a backward-facing step. *International Journal of Multiphase Flow*, **106**, 95–108. ISSN 03019322.

54. **Smith, B.**, **M. Andreani**, **U. Bieder**, **F. Ducros**, **D. Bestion**, **E. Graffard**, **M. Heitsch**, **M. Scheuerer**, **M. Henriksson**, **T. Hoehne**, **M. Houkema**, **E. Komen**, **J. Mahaffy**, **F. Menter**, **F. Moretti**, **T. Morii**, **P. Muehlbauer**, **U. Rohde**, **E. Krepper**, **C. Song**, **T. Watanabe**, **G. Zigh**, **C. Boyd**, **F. Archambeau**, **S. Bellet**, **J. Munoz-Cobo**, and **J. Simoneau** (2015). Assessment of CFD Codes for Nuclear Reactor Safety Problems - Revision 2. Technical Report NEA-CSNI-R–2014-12, OECD-NEA.

55. **Spalding, D. B.** (1961). A Single Formula for the "Law of the Wall". *Journal of Applied Mechanics*, **28**(3), 455–458. ISSN 0021-8936.

56. **Studer, E.**, **J. Brinster**, **I. Tkatschenko**, **G. Mignot**, **D. Paladino**, and **M. Andreani** (2012). Interaction of a light gas stratified layer with an air jet coming from below: Large scale experiments and scaling issues. *Nuclear Engineering and Design*, **253**, 406–412. ISSN 00295493.

57. **Sucec, J.** (1999). Prediction of heat transfer in turbulent, transpired boundary layers. *Journal of Heat Transfer*, **121**(1), 186–190. ISSN 0022-1481.

58. **Talbot, L.**, **R. K. Cheng**, **R. W. Schefer**, and **D. R. Willis** (1980). Thermophoresis of particles in a heated boundary layer. *Journal of Fluid Mechanics*, **101**(4), 737–758. ISSN 0022-1120.

59. **Vijaya Kumar, G.**, **L. M. Cammiade**, **S. Kelm**, **K. Arul Prakash**, **E. M. Groß**, **H. J. Allelein**, **R. Kneer**, and **W. Rohlfs** (2021). Implementation of a CFD model for wall condensation in the presence of non-condensable gas mixtures. *Applied Thermal Engineering*, **187**(August 2020), 116546. ISSN 13594311.

60. **Wilcox, D. C.**, *Turbulence Modeling for CFD - Third Edition*. DCW Industries, Incorporated, California, 2006.

61. **Wilke, C. R.** (1950). A Viscosity Equation for Gas Mixtures. *The Journal of Chemical Physics*, **18**(4), 517–519. ISSN 0021-9606.

62. **Zschaeck, G.**, **T. Frank**, and **A. Burns** (2014). CFD modelling and validation of wall condensation in the presence of non-condensable gases. *Nuclear Engineering and Design*, **279**, 137–146. ISSN 00295493.